EXPERIMENTAL STRATEGIES FOR INVESTIGATING PASSIVE AND ULTRASOUND-ENHANCED TRANSDERMAL DRUG DELIVERY

by

JENNIFER ELIZABETH SETO

B.S. Chemical Engineering, Rutgers University, 2005
M.S. Chemical Engineering Practice, Massachusetts Institute of Technology, 2007

Submitted to the Department of Chemical Engineering
in Partial Fulfillment of the Requirements for the Degree of

Doctor of Philosophy in Chemical Engineering

at the

MASSACHUSETTS INSTITUTE OF TECHNOLOGY

June 2011

Author_____
Department of Chemical Engineering
May 19, 2011

Certified by_____
Daniel Blankschtein
Professor of Chemical Engineering
Thesis Advisor

_____
Robert Langer
Institute Professor
Thesis Advisor

Accepted by _____
William Deen
Professor of Chemical Engineering
Chairman, Committee for Graduate Students

This Doctoral Thesis has been examined by the following Thesis Committee:

Daniel Blankschtein, Ph.D.
Thesis Advisor
Professor of Chemical Engineering
Massachusetts Institute of Technology

Robert Langer, Sc.D.
Thesis Advisor
Institute Professor
Massachusetts Institute of Technology

William Deen, Ph.D.
Professor of Chemical Engineering
Massachusetts Institute of Technology

Moungi Bawendi, Ph.D.
Professor of Chemistry
Massachusetts Institute of Technology

Betty Yu, Sc.D.
Vice President, Skincare & New Material Discovery
Living Proof, Inc.

EXPERIMENTAL STRATEGIES FOR INVESTIGATING PASSIVE AND ULTRASOUND-ENHANCED TRANSDERMAL DRUG DELIVERY

by

JENNIFER ELIZABETH SETO

Submitted to the Department of Chemical Engineering on May 19, 2011
in Partial Fulfillment of the Requirements for the Degree of
Doctor of Philosophy in Chemical Engineering

ABSTRACT

Transdermal drug delivery offers many advantages over traditional drug delivery methods. However, the natural resistance of the skin to drug permeation represents a major challenge that transdermal drug delivery needs to overcome in a safe and reversible manner. One method for enhancing transdermal drug delivery involves the application of ultrasound (US) to skin to physically overcome the skin's barrier properties. To advance this method, the focus of this thesis has been to develop novel experimental strategies and data analyses that can be utilized in *in vitro* investigations of passive and US-enhanced transdermal drug delivery.

US treatment is often combined with a chemical enhancer such as the surfactant sodium lauryl sulfate (SLS). The simultaneous application of US and SLS (referred to as US/SLS) to skin exhibits synergism in enhancing transdermal drug delivery and has been utilized in clinical settings. In order to study the delivery of therapeutic macromolecules into US/SLS-treated skin, e.g. vaccine delivery to the Langerhans cells or drug delivery to the blood capillaries near the epidermis-dermis junction, it would be desirable to conduct *in vitro* US/SLS-enhanced transdermal diffusion experiments using split-thickness skin (STS) models, in which much of the dermis is removed in order to simulate the *in vivo* transdermal diffusion to the desired skin component. Therefore, STS was evaluated as an alternative to the well-established US/SLS-treated full-thickness skin (FTS) model for the delivery of hydrophilic permeants. The skin permeabilities and the aqueous pore radii of US/SLS-treated pig FTS, 700-μm-thick pig STS, human FTS, 700-μm-thick human STS, and 250-μm-thick human STS were compared over a range of skin electrical resistivity values. The US/SLS-treated pig skin models were found to exhibit similar permeabilities and pore radii, but the human skin models did not. Furthermore, the US/SLS-enhanced delivery of gold nanoparticles and quantum dots (two model hydrophilic macromolecules) was found to be greater through pig STS than through pig FTS, due to the presence of less dermis that acts as an artificial barrier to macromolecules. In spite of greater variability in correlations between STS permeability and resistivity, the results strongly suggest the use of 700-μm-thick pig STS to investigate the *in vitro* US/SLS-enhanced delivery of hydrophilic macromolecules.

After the validation of the pig STS for US/SLS studies, this skin model was used to study the transdermal delivery of nanoparticles. While nanoparticles have potential as transdermal drug carriers, many studies have shown that nanoparticle skin penetration is limited. Therefore, the US/SLS treatment was evaluated as a skin pre-treatment method for enhancing the passive transdermal delivery of nanoparticles. Quantitative and qualitative methods (elemental analysis

and confocal microscopy, respectively) were utilized to compare the delivery of 10-nm and 20-nm cationic, neutral, and anionic quantum dots into US/SLS-treated and untreated pig STS. The findings include: (a) ~0.01% of the quantum dots penetrated the dermis of untreated skin (which was quantified for the first time), (b) the quantum dots fully permeated US/SLS-treated skin, (c) the two cationic quantum dots studied exhibited different extents of skin penetration and dermal clearance, and (d) the quantum dot skin penetration is heterogeneous (which was determined using a novel application of confocal microscopy). Routes of nanoparticle skin penetration are discussed, as well as the application of the methods described herein to address conflicting literature reports on nanoparticle skin penetration in the context of nanoparticle skin toxicity. US/SLS treatment is concluded to significantly enhance quantum dot transdermal penetration by 500 – 1300%. The findings suggest that an optimum surface charge exists for nanoparticle skin penetration, and motivate the application of nanoparticle carriers to US/SLS-treated skin for enhanced transdermal drug delivery.

The final investigation of this thesis focused on chemical penetration enhancers, which are used to enhance drug delivery through several biological membranes, particularly the stratum corneum of the skin. However, the fundamental mechanisms that govern the interactions between penetration enhancers and membranes are not fully understood. Therefore, the goal of this work was to identify naturally fluorescent penetration enhancers (FPEs) in order to utilize well-established fluorescence techniques to directly study the behavior of FPEs within the skin. In this study, 12 FPE candidates were selected and ranked according to their potency as skin penetration enhancers. The best FPEs found compared well to SLS, a well-known potent skin penetration enhancer. Based on the ranking of the FPEs, FPE design principles are presented. In addition, to illustrate the novel, direct, and non-invasive visualization of the behavior of FPEs within skin, three case studies involving the use of two-photon fluorescence microscopy are presented, including visualizing glycerol-mitigated and US-enhanced FPE skin penetration. Previous two-photon fluorescence microscopy studies have *indirectly* visualized the effect of penetration enhancers on skin by using a fluorescent permeant to probe the transdermal pathways of the penetration enhancer. These effects can now be *directly* visualized and investigated using FPEs. The combination of FPEs with fluorescence techniques represents a useful new approach for elucidating the mechanisms involved in penetration enhancement and membrane irritation, and for improving structure-activity relationships for penetration enhancers. The new physical insights obtained using FPEs will aid in designing effective penetration enhancers for drug delivery applications, including penetration enhancers to be combined with US for synergistically enhancing transdermal drug delivery.

The experimental strategies presented in this thesis pave the way for investigations in several transdermal fields, including evaluating nanoparticle skin toxicity, designing nanoparticle drug delivery carriers, evaluating ultrasound-assisted transdermal vaccination, elucidating mechanisms of chemical penetration enhancer-induced skin irritation, designing topical formulations with penetration enhancers, and elucidating mechanisms of ultrasound and penetration enhancer synergism in enhancing skin permeability.

Thesis Advisor: Daniel Blankschtein
Title: Professor of Chemical Engineering

Thesis Advisor: Robert Langer
Title: Institute Professor

THIS THESIS IS DEDICATED TO MY PARENTS

ANDY AND ELIZABETH SETO

ACKNOWLEDGEMENTS

The completion of this PhD is a significant milestone for the extended Seto family. This is the first PhD within a family that has come a long way from being a poor family in the rural hills of Hong Kong. My father's parents, Ting and Yuk Sim Seto, worked hard to make a living there, struggling to provide for their five sons and one daughter; they endured with significant aid from the Maryknollers. Luckily, an opportunity came along for a chance at a better life. My grandmother's sister, a US citizen by marriage, petitioned to allow my grandparents and their children to immigrate to the US in 1969; my grandfather's uncle sponsored the family with jobs in NYC. My grandparents were brave enough to move the family to the US because they believed that with hard work, their descendents could achieve the American Dream (success on "Golden Mountain"). They would be proud to know that their children and grandchildren did not disappoint them. We all lead very good lives now, thanks to my grandparents and everyone who supported them before, during, and after their immigration to the US. Now, my grandparents' legacy is preserved in the libraries of MIT; may they rest in peace.

My mother's grandfather was also brave in immigrating to the US by himself to work hard and support his family back in Hong Kong. After several years, during which he founded several businesses, he was able to sponsor his family's immigration to the US. He is also remembered fondly for being a proponent of hard work and a good education.

The story about all the events that led to the opportunity for me to earn a PhD from MIT has been inspirational to me. I drew upon this story for motivation during the many times throughout my PhD when I wasn't sure that I could finish. During those times, I had to remind myself that my parents and grandparents all worked very hard for me to have this opportunity, so I could not let it go to waste. Another aspect of this story that I drew upon was that any great achievement requires much help from others. My PhD was no exception, so I have many people to thank ...

First and foremost, I thank my parents. My father is an engineer at heart, and I got my "problem-solving genes" from him. I thank my mother for choosing to stay home during most of my childhood in order to raise good kids. My parents have done a tremendous job in providing me and my siblings happy memories and instilling in us the importance of doing well in school. (In particular, even though neither had a scientific background, both stressed the importance of math. As a result, they produced two engineers and one biomath/statistician!) In addition, I thank my parents, my sister, my brother, and my extended family for believing in me every step of the way.

Thanks to Carolyn for being such a great friend (and my life coach) ever since the ninth grade. I've always been able to count on her for great advice all the way through grad school. I wish her the very best as she completes her own PhD.

Thanks to all my teachers from the Scotch Plains-Fanwood K-12 school district who saw something special in me and reached out to point me in the right direction. Thanks to the NJ Governor's School in the Sciences program which inspired me to (accidentally) major in chemical engineering when I got to college, even though in hindsight my project was in the field of applied organic chemistry. Thanks to the faculty at Rutgers University who also reached out to me, engaged me in numerous conversations about preparing for my future career, and encouraged me to apply to graduate school and the NSF fellowship.

At MIT, I first thank my advisors, Professor Daniel Blankschtein and Professor Robert Langer. I thank Professor Blankschtein for the weekly discussions on my research progress and

for the extraordinary time and effort he invested in providing critical, constructive feedback on my work to help me present my work in the best light possible. I thank Professor Langer for the opportunity to work in his lab with seemingly endless resources. Both advisors cared greatly about my personal well-being. I thank them for guiding my growth as a scientific researcher, growing pains and all. I also thank my thesis committee members, Professor Moungi Bawendi, Professor William Deen, and Dr. Betty Yu, for asking insightful questions and for guiding my thinking in new ways.

Thanks to all of my collaborators, particularly Baris Polat and Professor Renata Lopez. Baris and I joined the transdermal project together. I thank him for his companionship during our shared trials and tribulations. Renata spent a 1.5-year sabbatical in our lab during my 4th and 5th years at MIT. Her optimistic and cheerful demeanor, fresh perspective in the lab, and belief in my abilities brought about the turning point in my PhD. Thanks to everyone else who has given me help, support, or advice over the years: members of the Blankschtein group, members of the Langer group, members of the Bawendi group, Brett VanVeller, Professor Pak Yuet, Professor Edward Boyle, Rick Kayser, Professor Francesco Stellacci, Randy Carney, Professor Darrell Irvine, and Anna Bershteyn. Thanks for administrative support from the Student Office and the Langer Office.

Thanks to the wonderful members of the MIT Women's Volleyball Club and Coach Tony Lee for providing a reason to get out of lab, a physical outlet for stress, and friendships and fun at practice and at tournaments. I was never an athletic person growing up. But after three stressful years at MIT, I looked for a recreational activity to have some fun and relieve stress. The first thing that I tried was volleyball, even though I was terribly bad at it in high school gym class. I started as a beginner, but in such a supportive environment, I quickly transitioned into a regular tournament player. The steady improvements of my volleyball skills and the occasional tournament wins gave me something to feel good about when research wasn't going well.

Thanks to Dan, Erin, Amanda, Jeff, and Wayne for sharing stories and laughter during lunchtime and for enjoying board games and card games almost as much as I do. Thanks to the Mak family for checking in on me from time to time and for the excursions outside of Cambridge.

Thanks to the Practice School program. Going to Practice School at Novartis in Switzerland and France and General Mills in Minnesota was a welcome break after finishing my thesis proposal in my second year. It was a great experience, both professionally and personally. In addition, it provided the opportunity to get to know Michael Harper, and we have been inseparable ever since. Thanks to him for being a wonderful, caring, and loving person, for being a shoulder to lean on, and for keeping me sane throughout this whole process.

Lastly, I am grateful for funding from the following sources: National Science Foundation Graduate Research Fellowship, National Institutes of Health, U.S. Army Research Office through the Institute for Soldier Nanotechnologies at MIT, and the Chemical Engineering Department (in various forms, including the Haas Family Fellowship Fund and the Robert T Haslam Fellowship).

TABLE OF CONTENTS

LIST OF FIGURES

LIST OF TABLES

CHAPTER 1

INTRODUCTION

1.1 OVERVIEW OF TRANSDERMAL DRUG DELIVERY

Transdermal drug delivery offers many advantages over traditional drug delivery methods, including oral delivery and injections. Delivery through the skin circumvents problems associated with the acidic environment of the stomach, liver metabolism, and absorption in the gastrointestinal tract [1,2]. Furthermore, transdermal drug delivery provides a non-invasive, minimal-pain alternative to injections, resulting in higher levels of patient compliance. Unfortunately, transdermal drug delivery has its own disadvantages. A major challenge that transdermal drug delivery needs to overcome in a safe and reversible manner is the natural resistance of the skin to drug permeation. At the start of this thesis work in December 2006, only 15 hydrophobic drug molecules (all with molecular weights of less than 400 Daltons) had FDA approval for therapeutic applications using transdermal delivery methods [3-6]. Currently, there are 19 drugs available in the form of a transdermal patch.

1.2 IMPACT OF SKIN STRUCTURE ON TRANSDERMAL DRUG DELIVERY

The reason why the skin is such a good protective barrier can be understood by examining the unique structure of the skin. The three main layers of the skin are the stratum corneum, the viable epidermis, and the dermis (see FIGURE 1-1). The stratum corneum, the

outermost layer, is the thinnest layer of the skin with a thickness of 10 – 20 μm in humans, while the viable epidermis and the dermis have thicknesses of 100 – 200 μm and 1 – 4 mm, respectively [7]. The stratum corneum typically consists of 15 offset layers of flat, interlocking, polyhedral corneocytes (dead skin cells filled with cross-linked keratin fibers) surrounded by a matrix of lipid bilayers. The stratum corneum structure has been compared to that of a brick wall, where the anucleated cells are the "bricks" and the intercellular lipids are the "mortar" (see FIGURE 1-2). This tightly packed brick-and-mortar structure is the primary barrier to transdermal diffusion.

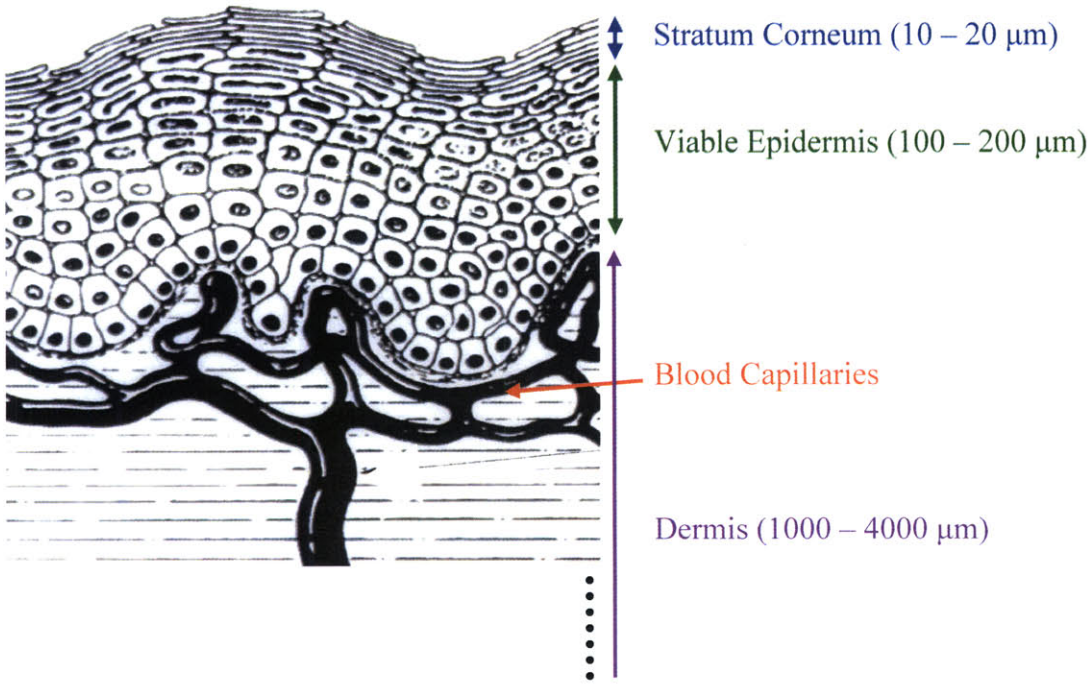

FIGURE 1-1: Sketch of the cross-section of the skin. The three main layers of the skin are the stratum corneum, the viable epidermis, and the dermis (figure adapted from [8]).

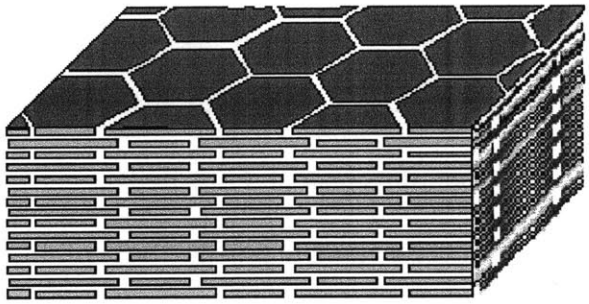

FIGURE 1-2: Schematic representation of the brick-and-mortar model of the stratum corneum. Corneocytes (depicted in gray) are shown with their characteristic hexagonal shape and are contained within the lipid bilayers (depicted in white). In humans, the stratum corneum has a thickness of 10 – 20 μm and typically consists of 15 interlocking layers of corneocytes (figure adapted from [9]).

1.3 METHODS TO ENHANCE TRANSDERMAL DRUG DELIVERY

To increase skin permeability, recent advances in transdermal drug delivery have focused on: (1) disrupting the highly ordered stratum corneum, (2) providing a driving force in addition to a chemical gradient across the skin, or (3) bypassing the stratum corneum. Such methods include: (i) electroporation, (ii) iontophoresis, (iii) chemical enhancers, (iv) microneedles, (v) laser-ablation, and (vi) sonophoresis. Briefly, electroporation creates temporary pores in the skin through the application of pulsed electric voltages, increasing the area available for permeant diffusion [10]. Iontophoresis enhances transdermal drug delivery for charged molecules by applying an electric field across the skin [10,11]. Chemical enhancers can enhance transdermal drug delivery by several mechanisms [12], including: (a) disrupting the lipid bilayers and the connective proteins of the stratum corneum [13], (b) interacting with keratin to denature it or to modify its conformation [14], (c) improving the drug partitioning between the donor solution and the stratum corneum [15], and (d) enhancing drug solubility in the donor solution [16]. Microneedles are short, thin needles that are designed to penetrate into the epidermis, effectively

bypassing the stratum corneum [17]. In this case, the injections are pain-free because the microneedles do not penetrate into the dermis, the skin layer with nerves [17]. Laser-ablation removes the stratum corneum from the desired drug delivery site [18]. Sonophoresis, the transdermal drug delivery enhancement method that is the focus of this thesis, utilizes ultrasound to make the stratum corneum more permeable. Each of the above enhancement methods has yielded successful results in increasing the skin permeability in order to facilitate drug transport. Additionally, combinations of these enhancement methods have been attempted with some synergistic effects observed, resulting in even greater enhancements of transdermal drug delivery [15,19-23]. One of the more interesting synergistic effects was observed by combining sonophoresis and chemical enhancers, which will be discussed in more detail in Section 1.4.5.

1.4 SONOPHORESIS

1.4.1 ULTRASOUND (US) BASICS

Sound is created by a mechanical vibration that is transmitted through a medium such that the particles in the medium vibrate. All the particles in the medium oscillate between regions of low and high pressure. The pressure cycle that these particles experience can be characterized by amplitude and frequency (see FIGURE 1-3). Sound waves with frequencies $\geq$ 20 kHz are collectively referred to as ultrasound (US). Various US frequencies have been utilized to enhance transdermal drug delivery. These frequencies are typically divided into three ranges: low frequency (20 – 100 kHz), therapeutic (0.7 – 3 MHz), and high frequency (> 3 MHz).

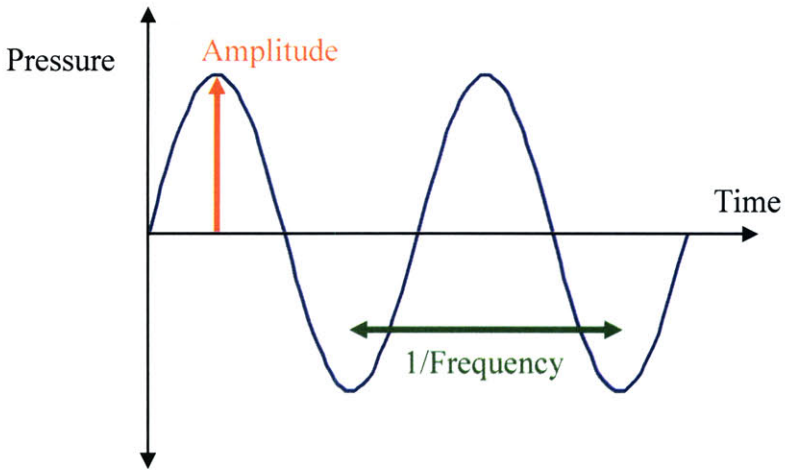

FIGURE 1-3: A sound wave, or a pressure wave, can be characterized by amplitude and frequency.

1.4.2 MECHANISMS OF US ENHANCEMENT

Low-frequency US has been shown to be most effective for enhancing transdermal drug delivery [24,25]. Mechanistically, low-frequency US induces acoustic cavitation bubble formation in the coupling medium between the US horn and the skin [26,27]. The implosion of the cavitation bubbles in the coupling medium near the skin surface leads to the onset of violent shockwaves that can disrupt the skin structure [26,27]. These shockwaves are accompanied by the onset of microjets that are directed toward the skin surface, which drives the coupling medium into the skin [26,27]. Additionally, US creates acoustic streaming in the coupling medium [26,27]. All of these mechanisms contribute to enhancing skin permeability, with cavitation being the main contributor [26,27]. For a more thorough discussion on the mechanisms of US enhancement, the reader is referred to [27].

1.4.3 Localized Transport Regions in US-Treated Skin

Interestingly, US treatment does not result in uniform skin permeability enhancement across the entire skin surface [27,28]. It is now well-established that US treatment creates areas of significantly higher permeability than the surrounding regions. These regions are referred to as localized transport regions (LTRs) and non-LTRs, respectively. They can be visualized when a dye is included in the coupling medium during US treatment (see Figure 1-4). It has recently been proposed that LTRs are regions above which cavitation-induced microjet collapses occurred, and that non-LTRs are regions of enhanced skin permeability resulting from acoustic streaming [29].

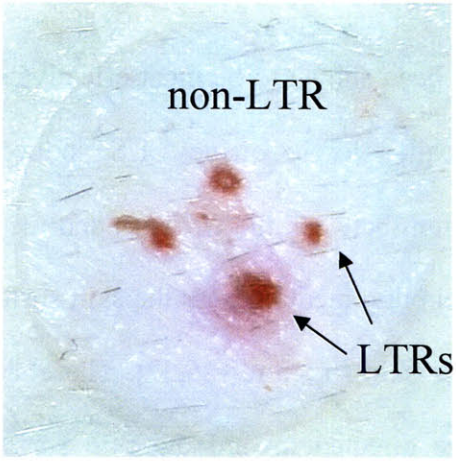

Figure 1-4: Localized transport regions (LTRs) and non-LTRs on the surface of pig skin treated with 20 kHz ultrasound and 40% ethanol (a chemical enhancer). The LTRs are stained with red food coloring.

1.4.4 Motivation for US-Enhanced Transdermal Drug Delivery

There are several attributes of sonophoresis that are advantageous for transdermal drug delivery. Specifically: (i) sonophoresis can enhance the delivery of a broad class of permeants, including hydrophobic and hydrophilic permeants and macromolecules [27,30], (ii) sonophoresis is non-invasive (there is no physical device, such as a needle, that penetrates the skin), (iii) sonophoresis treatment parameters, such as US frequency, intensity, and application time, can be varied to control the degree of skin permeability enhancement needed for topical or systemic deliveries [19,31-33], (iv) sonophoresis has been demonstrated in the clinic to be a patient-friendly treatment; it can be applied to the skin as a brief, pain-free treatment on the order of 10 seconds, prior to the application of a drug-loaded transdermal patch [34-36], and (v) sonophoresis is FDA-approved for transdermal drug delivery [37] (discussed further in Section 1.4.7).

1.4.5 US Synergism with Chemical Enhancers

Sonophoresis and chemical enhancers can be simultaneously applied to skin by including chemical enhancers in the coupling medium during US treatment. Without US, chemical enhancers can permeabilize skin by fluidizing or extracting the lipid bilayers of the stratum corneum and by denaturing the corneocytes. However, the extent of skin permeabilization is limited by the ability of the chemical enhancers to penetrate the skin. As mentioned in Section 1.4.2, US drives the coupling medium into the skin. Therefore, when chemical enhancers are included in the coupling medium, the US assists in the penetration of the chemical enhancers into the skin and their subsequent dispersion in the skin. The combination of these methods increases skin permeability to a greater extent than either method alone [23].

1.4.6 US SYNERGISM WITH SURFACTANTS

The synergism between US and chemical enhancers has been shown to be particularly significant for surfactants [21]. Surfactants are a unique subset of chemical enhancers because they preferentially adsorb at interfaces. Therefore, surfactants are not only present in the bulk coupling medium that is driven into the skin via microjets; they are also adsorbed onto the air/liquid interface of cavitation bubbles as the bubbles collapse towards the skin. Therefore, US more effectively assists with the penetration of surfactants into the skin relative to that of other chemical enhancers [38].

1.4.7 MOTIVATION FOR US/SLS TREATMENT

Several types of surfactants have been applied to skin simultaneously with US [21]. The most common surfactant combined with sonophoresis is sodium lauryl sulfate (SLS), a common anionic surfactant that is also known as sodium dodecyl sulfate (SDS). The combination of US and SLS treatments (referred to hereafter as US/SLS) has even been used in several clinical studies [30]. US/SLS was first applied to expedite the topical delivery of lidocaine, reducing the time of onset of numbness from 30 – 60 minutes to < 5 minutes [36]. A device for self-administration of US/SLS was developed by Sontra Medical (now Echo Therapeutics). This device, called SonoPrep, was FDA approved for use in both adults and children to expedite the onset of anesthesia prior to hypodermic injection, intravenous cannulation, and blood donation [35,36,39-41]. Clinical studies were also conducted to evaluate the technology for the continuous extraction of interstitial fluid for blood glucose monitoring [34]. This application is exciting because it can be coupled with insulin administration to create an automated transdermal system for the continuous treatment of diabetes. Likely due to the clinical validation of this technique,

several groups have been investigating US/SLS for enhancing transdermal drug delivery. This technique is the method of choice for studying enhanced transdermal drug delivery in this thesis.

1.5 THESIS OBJECTIVES

The unifying theme throughout my thesis work has been to advance the transdermal field by developing novel experimental strategies and data analyses that can be utilized in *in vitro* investigations of passive and US-enhanced transdermal drug delivery. The following specific objectives were carried out:

i. Evaluated split-thickness skin as an alternative *in vitro* skin model to full-thickness skin for investigating the US-enhanced delivery of hydrophilic permeants.
ii. Demonstrated the use of complementary, sensitive, quantitative and qualitative methods for evaluating the passive and US-enhanced transdermal delivery of nanoparticles.
iii. Identified novel fluorescent penetration enhancers in order to utilize fluorescence technologies to directly visualize their behavior within skin.

1.6 THESIS OVERVIEW

Following a description of the primary equipment used in this thesis, presented in Chapter 2, Chapters 3 – 5 describe studies on developing new strategies for investigating passive and US-enhanced transdermal drug delivery. Specifically, in Chapter 3, the split-thickness skin (STS) model, which is a common *in vitro* skin model used to investigate passive transdermal drug delivery, was evaluated as an alternative skin model for investigating US/SLS-enhanced transdermal drug delivery. Prior to this study, all *in vitro* investigations in US/SLS-enhanced

transdermal drug delivery had been carried out using full-thickness skin (FTS). In order to study the delivery of therapeutic macromolecules into US/SLS-treated skin, to the Langerhans cells or to the blood capillaries at the epidermis-dermis junction, it is desirable to conduct *in vitro* US/SLS-enhanced transdermal diffusion experiments using STS models, in which much of the dermis is removed in order to simulate the *in vivo* transdermal diffusion to the desired skin component. The motivation for this work was to show that FTS and STS undergo similar extents of skin structural perturbation in response to the US/SLS treatment, a combined mechanical and chemical skin permeability enhancement method, in spite of the fact that the two skin models differ in mechanical strength because of the thinner portion of dermis present in STS.

Chapter 4 describes an investigation aimed at enhancing the potential of rigid nanoparticles to serve as transdermal drug carriers by improving their skin penetration using US/SLS treatment. In this study, two experimental techniques – elemental analysis and confocal fluorescence microscopy – were combined to quantitatively and qualitatively investigate the delivery of nanoparticle drug carriers into US/SLS-treated skin and untreated skin (which is quantified for the first time). In addition, the combination of quantitative and qualitative methods presented here is proposed to clarify some of the controversies reported in the literature regarding the transdermal penetration of nanoparticles and nanoparticle skin toxicity.

Chapter 5 focuses on chemical penetration enhancers, which are used to enhance drug delivery through several biological membranes, particularly the stratum corneum of the skin. Prior to this study, the effect of penetration enhancers on skin structure could only be evaluated indirectly. In addition, the fundamental mechanisms that govern the interactions between penetration enhancers and membranes have not been fully elucidated. Therefore, the goal of this work was to identify naturally fluorescent penetration enhancers in order to utilize well-

established fluorescence techniques to directly visualize the behavior of penetration enhancers within the skin.

Finally, in Chapter 6, the contributions and impact of this thesis is summarized, and detailed recommendations are offered for future studies.

CHAPTER 2

PRIMARY EQUIPMENT

The main purpose of this chapter is to show figures of the primary equipment used in this thesis in order to aid the reader in understanding how the experiments were performed. In addition, the basic principles underlying the use of the equipment are discussed in order to aid the reader in interpreting the results presented in subsequent chapters.

2.1 FRANZ DIFFUSION CELL

A Franz diffusion cell consists of a donor chamber and a receiver chamber, with a skin sample mounted between the two chambers (see FIGURE 2-1). A clamp is used to hold the apparatus together. Electrodes are positioned above and below the skin and the chambers are filled with an aqueous solution in order to measure the skin electrical resistivity. A stirbar may be included to mix the receiver solution during skin permeability measurements. During ultrasound treatment, an ultrasound probe tip (see Section 2.2) is lowered into the donor chamber such that the tip is immersed in a coupling medium between the tip and the skin.

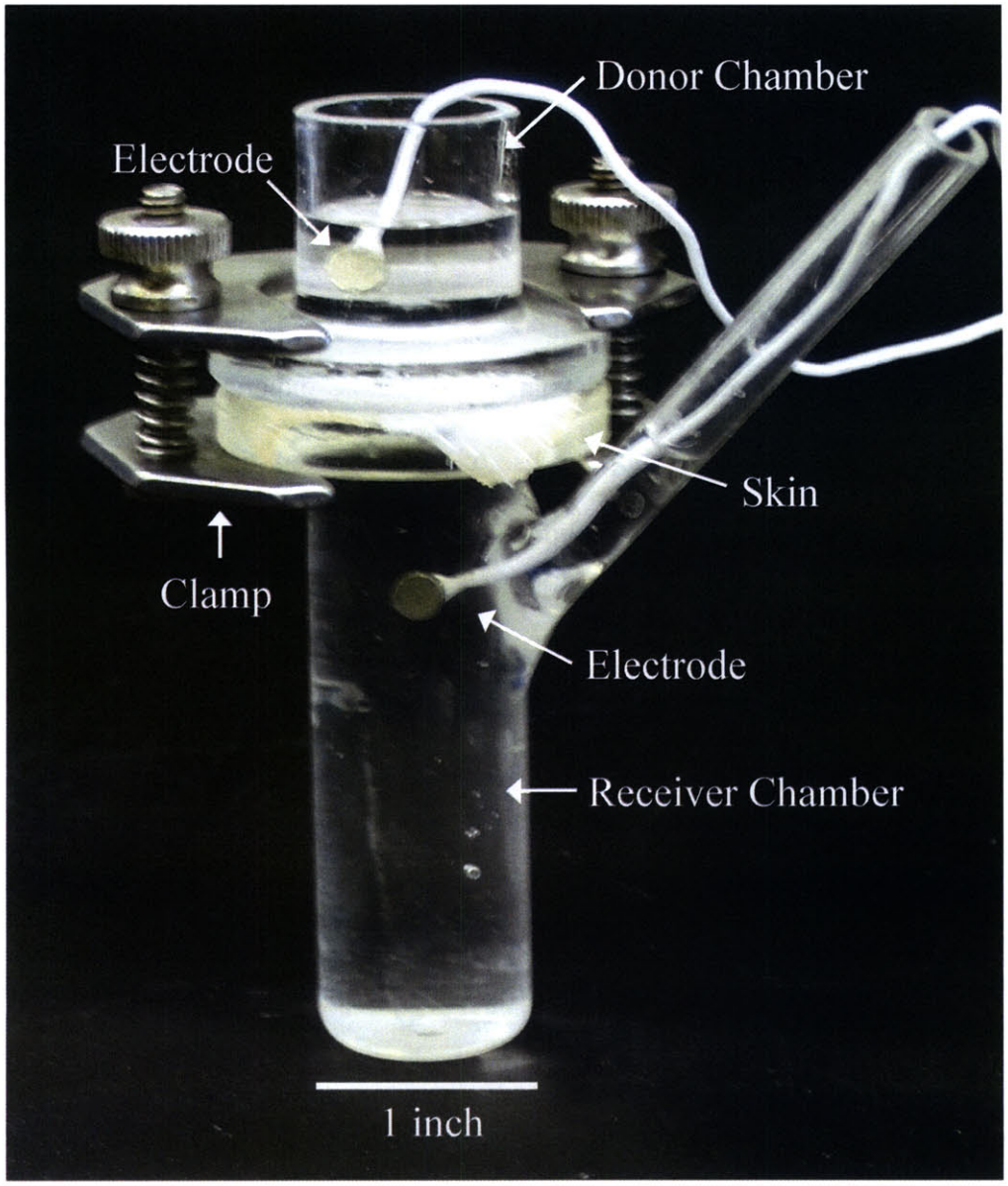

FIGURE 2-1: Franz diffusion cell.

2.2 ULTRASOUND EQUIPMENT

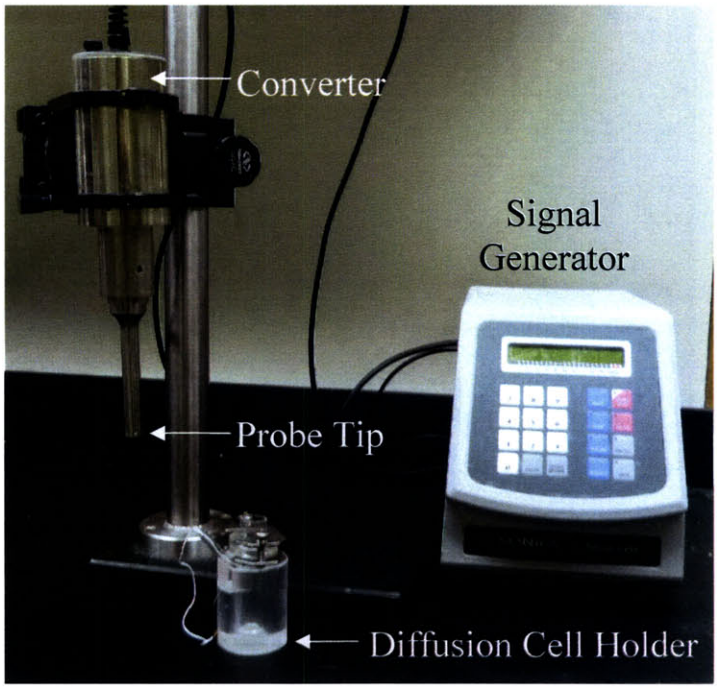

FIGURE 2-2: Ultrasound equipment.

The ultrasound equipment consists of a signal generator, converter, and probe (see FIGURE 2-2). On the signal generator, the ultrasound application time, pulse mode, and amplitude (which is related to the ultrasound intensity) can be specified. The electrical signal is transmitted to a piezoelectric transducer within the converter, where the signal is converted into a mechanical vibration. The probe amplifies the vibration generated by the converter. During ultrasound application, the probe tip is immersed in a coupling medium and is positioned at a specified distance from the skin sample (mounted into a Franz diffusion cell and supported by a diffusion cell holder).

2.3 DERMATOME

FIGURE 2-3: Dermatome.

A dermatome (see FIGURE 2-3) can be thought of as a large razor that is used to shave off a specified thickness of skin from a full-thickness skin sample in order to reduce the thickness of the dermis layer (see FIGURE 2-4). The top layer of skin that is "shaved off" is referred to as dermatomed, or split-thickness, skin.

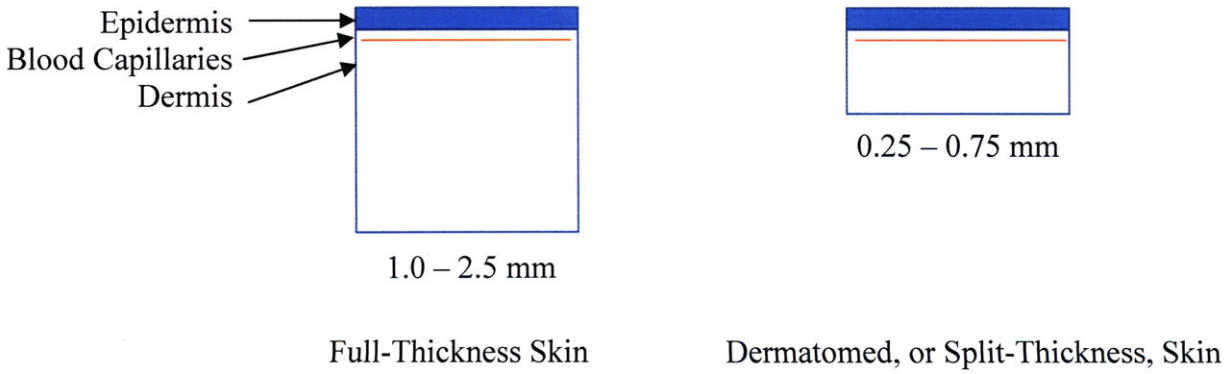

FIGURE 2-4: Comparison of skin thickness with and without dermatoming.

2.4 LIQUID SCINTILLATION COUNTER

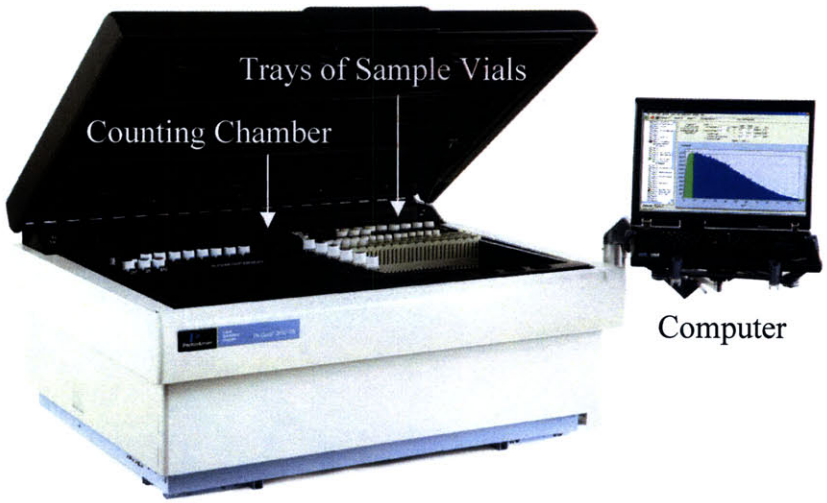

FIGURE 2-5: Liquid scintillation counter (figure from [42]).

A liquid scintillation counter (see FIGURE 2-5) is used to measure the radioactivity of a sample. Prior to loading sample vials into the liquid scintillation counter, scintillation cocktail is added to the vials. The scintillation cocktail absorbs radioactive emissions and emits fluorescence, thereby converting radioactivity into light, or scintillations. The liquid scintillation counter has a computer-automated conveyor system so that many samples can be counted after a single loading. Each vial is automatically placed in a dark counting chamber where a photomultiplier tube counts the scintillations.

2.5 CONFOCAL AND TWO-PHOTON FLUORESCENCE MICROSCOPY

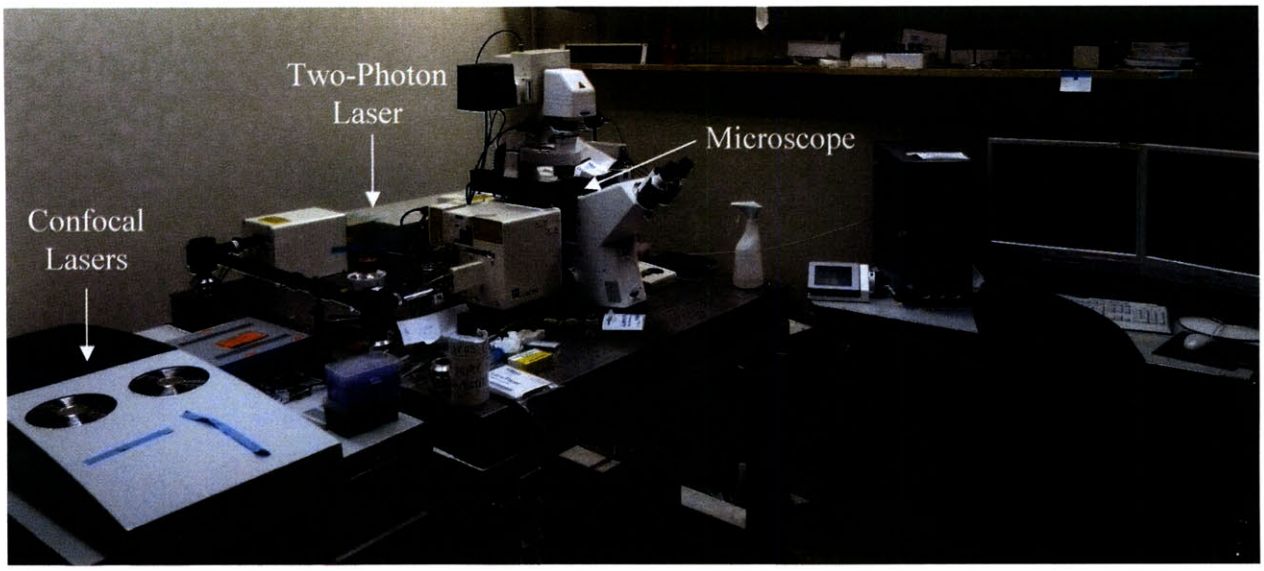

FIGURE 2-6: Confocal and two-photon fluorescence microscopy system.

Confocal and two-photon fluorescence microscopy are used to non-invasively acquire fluorescence images from selected depths within tissue (a process referred to as optical sectioning). The Zeiss LSM 510 system shown in FIGURE 2-6 is equipped for both confocal and two-photon microscopy. The sample is loaded onto the microscope, and various settings can be adjusted in order to acquire a confocal or two-photon image. Images are acquired one pixel at a time. For a two-dimensional image, each pixel is recorded by a computer as the laser scans over the entire plane of interest. A three-dimensional image can be generated by assembling a stack of two-dimensional images from scanning successive focal planes.

For each pixel, a laser is focused by an objective lens onto a focal point within the sample. The subsequent fluorescence (along with scattered light and reflected laser light) is then collected by the objective lens. A series of mirrors, filters, and pinholes are used to isolate the desired fluorescence originating from the focal point. In addition, the sample fluorescence beam

can be split by wavelength and sent to separate photomultiplier tubes in order to separately detect various colors of fluorescence originating from the focal point.

The basic principles of confocal and two-photon microscopy are different. For confocal microscopy, the laser that is utilized consists of photons of sufficient energy to excite the fluorophores within the sample. By focusing the laser beam onto a focal point, most of the fluorescence collected by the objective lens originates from the focal point, and fluorescence from outside of the focal point can be physically excluded through the use of a pinhole. For two-photon microscopy, the laser consists of photons of roughly half of the energy required to excite the sample. Therefore, a fluorophore must simultaneously absorb two photons in order to fluoresce. Within the focal point, the photon density is sufficiently high to generate significant amounts of two-photon-excited fluorescence. Outside of the focal point, where the photon density is lower, the number of two-photon absorption events is very small. Therefore, two-photon microscopy is more efficient than confocal microscopy and does not require a pinhole to block fluorescence from outside of the focal point. However, a high-powered laser is required for two-photon microscopy, since the photon density at the focal point must be roughly one million times that required for confocal microscopy.

2.6 INDUCTIVELY COUPLED PLASMA-MASS SPECTROMETRY (ICP-MS)

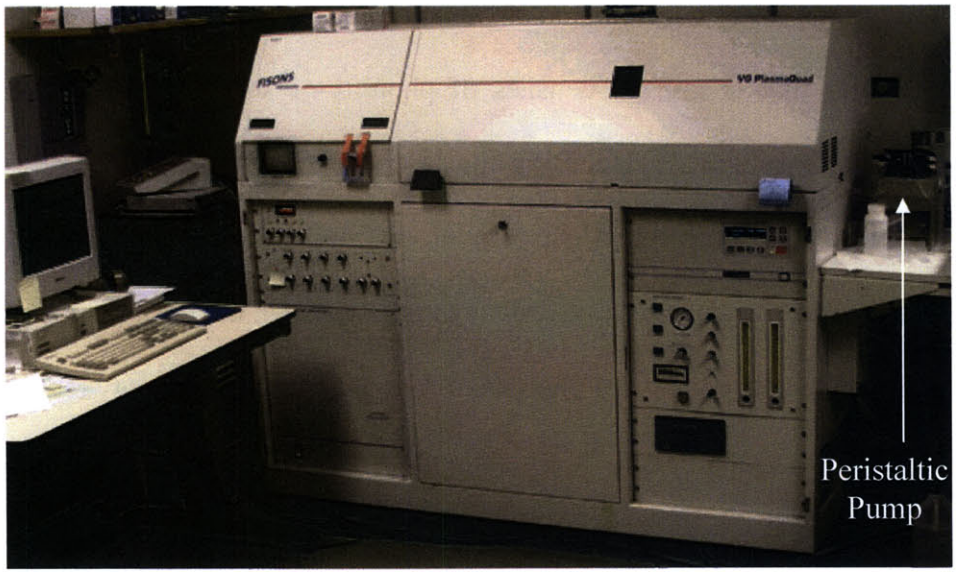

FIGURE 2-7: Inductively coupled plasma-mass spectrometry (figure from [43]).

Inductively coupled plasma-mass spectrometry (ICP-MS), also referred to as elemental analysis, is a sensitive method used to quantify trace levels of elements. Prior to injection into the ICP-MS, solid and liquid samples are digested (i.e. solubilized and homogenized) using nitric acid and an elevated temperature. The resulting aqueous samples are injected into the ICP-MS (see FIGURE 2-7) via a peristaltic pump. Then, the sample is atomized and ionized in a high-temperature argon plasma. Finally, the mass spectrum of the plasma is acquired.

Note that this method is time-consuming because all glassware and vials must be meticulously cleaned (using a process which lasts several days) in order to minimize background levels, allowing for the analysis of trace levels of elements in samples. The process of sample digestion and preparation for injection also occurs over several days.

CHAPTER 3

EVALUATING THE SPLIT-THICKNESS SKIN MODEL FOR THE US/SLS-ENHANCED TRANSDERMAL DELIVERY OF HYDROPHILIC PERMEANTS *

3.0 PREFACE

This study was originally motivated by unsuccessful attempts to quantify the delivery of quantum dots through US/SLS-treated full-thickness skin (FTS). At the start of my thesis work, I had aimed to utilize quantum dots as model permeants for studying the US/SLS-enhanced delivery of nanoparticles. However, using the common quantum dot assaying methods of UV/Vis absorption and spectrofluorimetry, I could not determine if the quantum dots were delivered across the skin and into the receiver chamber of the Franz diffusion cell (see Chapter 2, Section 2.1).

One possibility for not detecting quantum dots in the receiver solution was that the quantum dots were not penetrating into the skin to begin with. To rule this out, I used confocal fluorescence microscopy and two-photon fluorescence microscopy to show that quantum dots were at least penetrating into the stratum corneum and diffusing into the epidermis. Since the

* Most of this chapter has been reproduced from JE Seto, BE Polat, RFV Lopez, D Blankschtein, and R Langer. Effects of ultrasound and sodium lauryl sulfate on the transdermal delivery of hydrophilic permeants: comparative in vitro studies with full-thickness and split-thickness pig and human skin. Journal of Controlled Release 145, 26-32 (2010).

stratum corneum is widely considered to be the major diffusion barrier to hydrophilic permeants, the next logical step was to consider that the dermis was acting as a diffusion barrier to the quantum dots. Next, preliminary experiments were conducted with US/SLS-treated split-thickness skin (STS); STS is prepared by partially removing the dermis from FTS (see Chapter 2, Section 2.3). In these preliminary studies, the use of STS skin led to a higher concentration of quantum dots in the receiver chamber. This could be explained in two ways: (1) compared to FTS, the STS has less dermis ("sink" material) in which steady-state diffusion must be established before quantum dots pass into the receiver chamber, and/or (2) the US/SLS-enhanced permeability of STS is higher than that of FTS. The use of STS to obtain higher concentrations of quantum dots in the receiver chamber would only be justified if it was demonstrated that (2) is not true. Therefore, it became necessary to show that STS and FTS are equivalent skin models for US/SLS-enhanced transdermal permeability studies (i.e. their enhanced permeabilities are comparable), as described in this chapter.

3.1 INTRODUCTION

The simultaneous application of low-frequency ultrasound and the surfactant sodium lauryl sulfate (referred to as US/SLS) to skin enhances transdermal drug delivery in a synergistic mechanical and chemical manner [19,21]. With the advance of US/SLS, as well as of other transdermal drug delivery enhancement methods [44,45], it is now possible to transdermally deliver therapeutic macromolecules (including proteins, vaccines, and drug delivery vehicles) in significant amounts [46-48]. The delivery targets for these macromolecules are the Langerhans cells in the epidermis or the blood capillaries just below the epidermis. In the case of macromolecules, one must now consider the dermis as a potential artificial diffusion barrier in *in*

vitro transdermal drug delivery studies, regardless of the hydrophilicity of the macromolecule. The dermis may act as a reservoir (i.e. a diffusion sink) for absorbed macromolecules due to steric hindrance effects or interactions between the macromolecules and the dermal components [7,49,50]. Therefore, split-thickness skin (STS) would be an attractive alternative skin model to full-thickness skin (FTS) to reduce the barrier properties of the dermis and to more accurately study the US/SLS-enhanced transdermal delivery of therapeutic macromolecules. Yet, all *in vitro* US/SLS studies have been carried out using the well-established FTS model [51-57].

STS is typically prepared from full-thickness skin (FTS) using a dermatome, which removes much of the dermis from FTS (see Chapter 2, Section 2.3). Even though STS is a common skin model for *in vitro* transdermal drug delivery studies, it is not at all clear that STS is a suitable skin model for the application of US/SLS.* This is because US/SLS enhances skin permeability in a synergistic mechanical and chemical manner [19,21], and since FTS and STS differ in the thickness of dermis acting as an underlying mechanical support, FTS and STS may undergo different extents of skin structural perturbation in response to the US/SLS treatment. In fact, the possibility that FTS and STS could respond differently to the application of US motivated a previous comparative study on US-treated skin models [58] that was completed before US was combined with SLS to more effectively enhance skin permeability [15,19,59]. Since the US/SLS treatment was found to be more effective than the previously used US treatment [15,19,59], and since the US/SLS treatment is the currently used one in clinical

* Note that the alternative protocols involving applying US/SLS to FTS and then partially removing the dermis to create STS are not practically feasible. This is mainly because the skin must be clamped into a diffusion cell during the US/SLS treatment, resulting in a partially compressed skin sample from which the STS preparation is difficult. For details, see Appendix, Section 3.5.

applications [35,60], a similar comparative study on US/SLS-treated FTS and STS is clearly needed.

With the above need in mind, the primary objective was to investigate whether US/SLS-treated STS would be a suitable alternative to the well-established US/SLS-treated FTS model. This comparative study was performed on two pig skin models and three human skin models: pig FTS (pFTS), 700-μm-thick pig STS (p700), human FTS (hFTS), 700-μm-thick human STS (h700), and 250-μm-thick human STS (h250). Note that the third human skin model is the thinnest that could be consistently prepared using a dermatome, and that pig STS models with thicknesses $\leq$ 450 μm are not suitable for US/SLS treatment (see Appendix, Section 3.6). The aqueous porous pathway model was utilized to compare the effects of US/SLS treatment on the skin permeability and the effective skin aqueous pore radius of the hydrophilic transport pathways within these five skin models. The following will be shown in this chapter: (1) pig FTS and STS models exhibit similar US/SLS-enhanced permeabilities and pore radii after US/SLS treatment, (2) human FTS and STS models exhibit different permeabilities and pore radii after US/SLS treatment, and (3) a comparison of the US/SLS treatment times for the skin models strongly suggests that intrinsic differences within pig and human skin are contributing to the observed differences in (1) and (2). The strengths and weaknesses of each skin model investigated will be discussed. In addition, two examples will be provided to compare pig STS to FTS for *in vitro* US/SLS experiments in the case of gold nanoparticles and quantum dots, which serve as well-characterized, model hydrophilic macromolecular permeants. Specifically, it will be demonstrated that due to a thinner dermal layer, gold nanoparticles and quantum dots diffuse through STS in greater amounts compared to FTS. These results suggest that the use of pig STS

over FTS may be beneficial in future *in vitro* studies on the US/SLS-enhanced transdermal delivery of hydrophilic macromolecules.

3.2 Materials and Methods

3.2.1 Chemicals

^{14}C-labeled sucrose in sterile water (600 mCi/mmol) was obtained from American Radiolabeled Chemicals (St. Louis, Missouri). Phosphate buffered saline (PBS) tablets and SLS solution (20 w/v% in water) were obtained from Sigma-Aldrich (St. Louis, Missouri). PBS was prepared from PBS tablets according to the manufacturer's instructions. Hionic-Fluor scintillation cocktail was obtained from PerkinElmer (Waltham, Massachusetts). Gold nanoparticles, with a core diameter of 4.6 ± 1.5 nm (mean ± SD) and an 11-mercapto-1-undecanesulphonate ligand shell, were a gift from Professor Francesco Stellacci's group at MIT (synthesized using a published method [61]). Quantum dots with a CdSe core, ZnS shell, amphiphilic polymer and polydiallyldimethylammonium chloride ligand coating, and 20-nm hydrodynamic diameter (catalog no. QSQ-600) were obtained from Ocean NanoTech (Springdale, Arkansas). Nitric acid (BDH, Aristar® Ultra grade), hydrochloric acid (BDH, Aristar® Ultra grade), hydrogen peroxide (EMD Chemicals, Suprapur® grade), and certified gold, cadmium, and indium stock standards (BDH, Aristar® grade) were obtained from VWR International (West Chester, Pennsylvania). Deionized water dispensed from a Milli-Q academic water purification system (Millipore, Bedford, Massachusetts) was used to prepare all solutions.

3.2.2 SKIN PREPARATION

Human FTS (21 – 50 year old Caucasian back and abdominal skin, excised ≤ 12 hours post-mortem, shipped at −80°C) was obtained from National Disease Research Interchange (Philadelphia, Pennsylvania) and stored at −80°C until use. Before each experiment, the skin was thawed, the subcutaneous fat was removed with a razor blade, and excess hair was trimmed with scissors. Female Yorkshire pig FTS (back and flank skin) was harvested within an hour after sacrificing the 70-pound animal (purchased from E.M. Parsons & Sons, Hadley, Massachusetts). The subcutaneous fat was removed, and the skin was sectioned into 1-inch strips before storing at −80°C until use. Before each experiment, the skin was thawed and excess hair was trimmed with scissors. After these preparations, the human and pig FTS thicknesses ranged from 2 to 4 mm and 1 to 2.5 mm, respectively. Then, STS was prepared from 1-inch strips of FTS using an electric dermatome (Zimmer Orthopaedic Surgical Products, Dover, Ohio). Next, the FTS or STS strips were sectioned and placed on top of a 150-μm opening nylon mesh (Sefar Filtration, Depew, New York) for support. High vacuum grease (Dow Corning, Midland, Michigan) was applied to 15-mm inner diameter standard Franz diffusion cells (PermeGear, Hellertown, Pennsylvania) in order to create a water-tight seal between the skin and the diffusion cell. Finally, the skin was clamped into the diffusion cells. This experimental protocol was approved by the Committee on Animal Care at MIT.

3.2.3 MEASUREMENT OF SKIN ELECTRICAL RESISTIVITY

The skin electrical resistivity, R, is a sensitive quantitative indicator of the structural state of the skin [58,62,63]. R was measured according to a previously published method [53,58]. Briefly, a voltage was applied across the skin sample using two Ag/AgCl electrodes (#E242, In

Vivo Metric, Healdsburg, California). The skin electrical current was measured using a multimeter, and the skin electrical resistance was obtained from the skin electrical current using Ohm's Law (taking into account the background resistance). The skin electrical resistance was multiplied by the skin area to obtain the value of R. This method was used to: (1) check the initial structural state of the skin—any skin sample with an initial R value of < 50 kΩ cm^2 was considered damaged [64,65] and was discarded, (2) determine if the desired value of R had been reached during US/SLS treatment, indicating that the desired extent of skin structural perturbation was attained, and (3) determine the average value of R during the time period when the skin permeability to sucrose was measured. The values measured in (3) were used in the analysis described in Section 3.2.9.

3.2.4 US/SLS Pre-Treatment of the Skin

The protocol consisted of first pre-treating skin with US/SLS, and then carrying out a passive sucrose permeation experiment for 26 hours to measure the US/SLS-enhanced steady-state skin permeability to sucrose. For the first step of the protocol, US/SLS was applied to the intact skin samples based on a previously published method [52], with the following modifications: US, with the probe tip immersed in a coupling medium containing 1 w/v% SLS in PBS, was applied to the skin samples with a VCX 500 and a coupler probe (Sonics & Materials, Newtown, Connecticut) at the following typical US parameters [28]: frequency - 20 kHz, intensity - 7.5 W/cm^2, pulse length - 5 seconds on, 5 seconds off, and distance between the probe tip and the skin - 3 mm. The US intensity was calibrated using calorimetry [31]. The US/SLS treatment was stopped at least every 2 minutes to determine if the desired R value was attained and to replace the coupling medium (to minimize thermal effects [21]). The aim of the US/SLS

treatment was to attain a range of R values, corresponding to a range in the extent of skin structural perturbation. The maximum and minimum R values attained were 40 kΩ cm^2 (corresponding to a minimal amount of US/SLS treatment) and 0.4 kΩ cm^2 (within the range of R values attained using an FDA-approved ultrasonic skin permeation device in clinical applications [37,60]), respectively.

3.2.5 Measurement of Skin Permeability to Sucrose

After applying US/SLS treatment to skin (see Section 3.2.4), the skin permeability to sucrose was measured. Sucrose was previously determined to be a reliable hydrophilic probe molecule for using the porous pathway model to estimate the skin aqueous pore radius [66]. US/SLS-treated skin samples were remounted into clean, dry Franz diffusion cells. 12 mL of PBS was added to the receiver chambers, and 2 mL of donor solution containing ^{14}C-labeled sucrose in PBS was added to the donor chambers. Typical donor solution concentrations ranged from 5 μCi/mL for the skin samples with R values of 40 kΩ cm^2 to 0.3 μCi/mL for the skin samples with R values of 0.4 kΩ cm^2. Note that the donor solution concentrations were chosen such that the amount of ^{14}C in the receiver solution aliquots was at least ten times that in PBS (background). Diffusion experiments were conducted at room temperature (25°C) and under occluded conditions by sealing the donor chambers and sampling ports with parafilm. The receiver solutions were magnetically stirred at 400 RPM.

Samples were withdrawn from the diffusion cells during the steady-state domain at five predetermined time points from 18 to 26 hours (the attainment of steady-state diffusion is discussed in the Appendix, Section 3.7). At each time point, R was measured, 200-μL aliquots of the donor solutions were withdrawn, and 400-μL aliquots of the receiver solutions were

withdrawn. Each receiver solution aliquot was immediately replaced with an equal volume of PBS. After mixing each aliquot with 5 mL of scintillation cocktail, the radioactivity of the aliquots was measured using a Tri-Carb 2810TR liquid scintillation analyzer (PerkinElmer, Waltham, Massachusetts). Finally, the skin permeability to sucrose, P, was calculated at steady-state, sink conditions using the following well-known equation:

$$P = \frac{V}{AC_d}\left(\frac{\Delta C}{\Delta t}\right) \tag{3-1}$$

where V is the volume of PBS in the receiver chamber, A (= 1.77 cm^2) is the permeation area, C_d is the average sucrose concentration in the donor chamber, and ($\Delta C/\Delta t$) is the steady-state rate of change in sucrose concentration in the receiver chamber (taking into account the replacement of the receiver aliquots and the background radioactivity) [28]. The experimental conditions for which Eq. (3-1) is valid are discussed in the Appendix, Section 3.7.

3.2.6 Calculation of the Effective Skin Aqueous Pore Radius

The main assumption of the aqueous porous pathway model is that a hydrophilic permeant traverses the skin via the same aqueous porous pathway as the conducting ions in the electrolyte solution surrounding the skin (in PBS, the dominant ions are Na^+ and Cl^-) [66]. The porous pathway model was developed in order to quantify the effects of steric hindrance resulting from the radii of the permeant and of the conducting ions relative to the effective skin aqueous pore radius, r_{pore} [66]. Accordingly, r_{pore} can be determined by comparing the hindered transdermal diffusion of the permeant (related to P) to that of the conducting ions (related to R) [66].

Based on the porous pathway model [66], the relationship between P and R is given by:*

$$\log P = \log C - \log R \tag{3-2}$$

where C is defined as follows [66]:

$$C = \frac{kT}{2z^2 F c_{ion} e_0} \frac{D_p^{\infty} H(\lambda_p)}{D_{ion}^{\infty} H(\lambda_{ion})} \tag{3-3}$$

where k is the Boltzmann constant, T is the absolute temperature, z is the electrolyte valence, F is the Faraday constant, c_{ion} is the electrolyte molar concentration, e_0 is the electronic charge, D_i^{∞} is the diffusion coefficient of solute i (permeant (p) and ion) at infinite dilution, $H(\lambda_i)$ is the diffusive hindrance factor of solute i, and λ_i is the ratio of the radius of solute i, r_i, and r_{pore} (that is, $\lambda_i = r_i/r_{pore}$). In previous applications of the porous pathway model [33,52,53,58,66-69], $H(\lambda_i)$ was evaluated using the Renkin equation for $\lambda_i < 0.4$ as follows:

$$H(\lambda_i) = (1-\lambda_i)^2 [1 - 2.104\lambda_i + 2.09\lambda_i^3 - 0.95\lambda_i^5] \tag{3-4}$$

The hydrodynamic theory of hindered transport has advanced since the Renkin equation was first introduced in 1954. A more accurate expression for $H(\lambda_i)$ was developed in 2006. Specifically, for $\lambda_i \leq 0.95$, $H(\lambda_i)$ is given by [70]:

$$\begin{aligned} H(\lambda_i) = 1 + \frac{9}{8}\lambda_i \ln \lambda_i - 1.56034\lambda_i + 0.528155\lambda_i^2 + 1.91521\lambda_i^3 \\ - 2.81903\lambda_i^4 + 0.270788\lambda_i^5 + 1.10115\lambda_i^6 - 0.435933\lambda_i^7 \end{aligned} \tag{3-5}$$

Note that C in Eq. (3-3) is a function of a single skin structural parameter, r_{pore} (through λ_i

* The logarithmic form is used so that the regressed slopes and intercepts (see Section 3.2.9) are of the same order of magnitude.

= r_i/r_{pore} in $H(\lambda_p)/H(\lambda_{ion})$), as well as of other parameters that are not intrinsic to the skin structure. Furthermore, by evaluating Eq. (3-3) for various values of r_{pore}, one finds that log C increases (i.e. becomes less negative) as r_{pore} increases.

For a log P – log R data set, each data point was extrapolated to the y-axis using a theoretical slope value of −1 (see Eq. (3-2)) to calculate log C. From the extrapolated log C values, the average log C value and associated 95% confidence interval were calculated. Finally, r_{pore} was determined from the average log C value using Eq. (3-3), Eq. (3-5), and the following parameter values: $k = 1.38066 \cdot 10^{-23}$ J/K, $T = 298$ K, $F = 9.6485 \cdot 10^{4}$ C/mol, $e_0 = 1.6 \cdot 10^{-19}$ C, $z =$ 1 (for NaCl, the dominant electrolyte), $c_{ion} = 0.137$ M, $D_{ion}^{\infty} = 1.33 \cdot 10^{-5}$ cm^2/s at 298 K, $r_{ion} = 2.2$ Å, $D_p^{\infty} = 5.20 \cdot 10^{-6}$ cm^2/s at 298 K, and $r_p = 5.55$ Å. The endpoints of the 95% confidence interval for r_{pore} were calculated using the endpoints of the 95% confidence interval for log C.

3.2.7 US/SLS-Enhanced Transdermal Delivery of Gold Nanoparticles

3.2.7.1 Transdermal Delivery of Gold Nanoparticles

Pig FTS and STS samples were pre-treated with US/SLS (as described in Section 3.2.4) to attain R values of 0.8 – 1.2 kΩ cm^2. Then, the US/SLS-treated skin samples were remounted into clean, dry Franz diffusion cells. 12 mL of PBS was added to the receiver chambers, and 0.3 mL of the donor solution (0.1 w/v% gold nanoparticles in water) was added to the donor chambers. Diffusion experiments were conducted for 24 hours at room temperature (25°C), and the receiver solutions were magnetically stirred at 400 RPM.

At the end of each diffusion experiment, the receiver solution and the skin sample were collected. To minimize interference with the ICP-MS analysis of trace metals (see Section 3.2.7.2), the PBS salts were dialyzed out of the receiver chamber solution using a SnakeSkin

3500 molecular weight cut-off regenerated cellulose membrane (Pierce Biotechnology, Rockford, Illinois) that was placed in a stirred beaker of deionized water. The beaker was recharged with fresh water three times over a period of 24 hours. From the skin sample, the skin area exposed to US/SLS pre-treatment and passive gold nanoparticle diffusion was isolated using scissors; then, the epidermis was mechanically separated from the dermis using a spatula [71]. Finally, the dialyzed receiver solution and the dermis were analyzed by ICP-MS as described in Section 3.2.7.2.

3.2.7.2 Quantification of Gold Nanoparticles by ICP-MS

Inductively coupled plasma-mass spectrometry (ICP-MS) was performed using a PlasmaQuad 2+ Quadrupole Mass Spectrometer (Fisons Instruments, Merrimac, Massachusetts) to quantify the amount of gold in various samples, based on a previously published method [72]. Briefly, the receiver solutions and dermis samples (see Section 3.2.7.1) were digested under reflux by the addition of aqua regia in polyfluor alkoxy vials (Savillex, Minnetonka, Minnesota) for 16 hours at 110 – 120°C. Each acid digestion sample was then diluted using 1% nitric acid. To ensure the accuracy and precision of the technique, each sample was spiked with a standard indium (^{115}In) salt solution prior to injection into the ICP-MS system. Calibration plots were generated using gold standard solutions.

3.2.8 US/SLS-Enhanced Transdermal Delivery of Quantum Dots

3.2.8.1 Transdermal Delivery of Quantum Dots

Quantum dots were supplied as a 2 μM solution containing unbound polydiallyldimethyl ammonium chloride ligands. The unbound ligands were removed using the following supplier-

recommended procedure: the quantum dot solution was dialyzed using Spectra/Por 100,000 molecular weight cut-off cellulose ester membranes (Spectrum Laboratories, Rancho Dominguez, California) that were placed in stirred beakers of deionized water. The beakers were recharged with fresh water three times over a period of 24 hours. The dialyzed quantum dot solution had a final concentration of 0.62 ± 0.06 μM, which was used as the donor solution in transdermal diffusion experiments as described in Section 3.2.7.1 (the R values attained were 1.3 – 2.3 kΩ cm^2).

3.2.8.2 Quantification of Quantum Dots by ICP-MS

The quantification of ^{111}Cd (cadmium, an element of the quantum dot core) by ICP-MS was conducted as described in Section 3.2.7.2, with the following modifications: (1) samples were digested under reflux by the addition of nitric acid and hydrogen peroxide, and (2) acid digestion samples were then dried at 60°C before redissolution in 1% nitric acid. Since the quantum dot donor solution concentration was low, experiments without quantum dots were also conducted for measuring background cadmium amounts to determine whether the cadmium amounts in the receiver solution were significantly greater than background amounts. Calibration plots were generated using cadmium standard solutions.

3.2.9 Statistical Analysis

A linear regression was fitted to the log P – log R data set for each skin model considered. The regression parameters were subjected to an analysis-of-variance and an analysis-of-covariance [73] as discussed in Sections 3.3.1 and 3.3.2. Two-sample, two-tailed t-tests assuming unequal variances were used to compare log C values, US/SLS treatment times, gold

amounts, and cadmium amounts. In all analyses, p values < 0.05 were considered to be statistically significant.

Note that a matter of significant importance was that t-tests which assume *unequal* variances were used to compare log C values. Previous analyses based on t-tests assuming equal variances resulted in erroneous conclusions.

3.3 Results and Discussion

3.3.1 Log P – Log R Correlations are Well-Described by the Porous Pathway Model

Figure 3-1 shows the experimental log P – log R correlations obtained for the five skin models investigated, and Table 3-1 lists the log P – log R linear regression parameters. Table 3-1 shows that the regressed slopes for all five skin models are not significantly different from -1. In addition, the r^2 values of the regressions are within the expected range reported in the literature [66,74], and an analysis-of-variance showed that the regressions are statistically significant (the linear regressions "fit" the data, or the observed variations in P are explained by the linear log P – log R correlations).

Since the regressed slopes are -1 and the linear regressions are statistically significant, two conclusions can be drawn. First, within the range of US/SLS treatment conditions examined, the five skin models considered respond to US/SLS in a predictable manner. Specifically, the transdermal transport of sucrose through the five US/SLS-treated skin models is well-described by the porous pathway model. Therefore, the porous pathway model can be applied to compare the structural parameters of the hydrophilic transport pathways within each of the five skin models, which is discussed in Section 3.3.2.

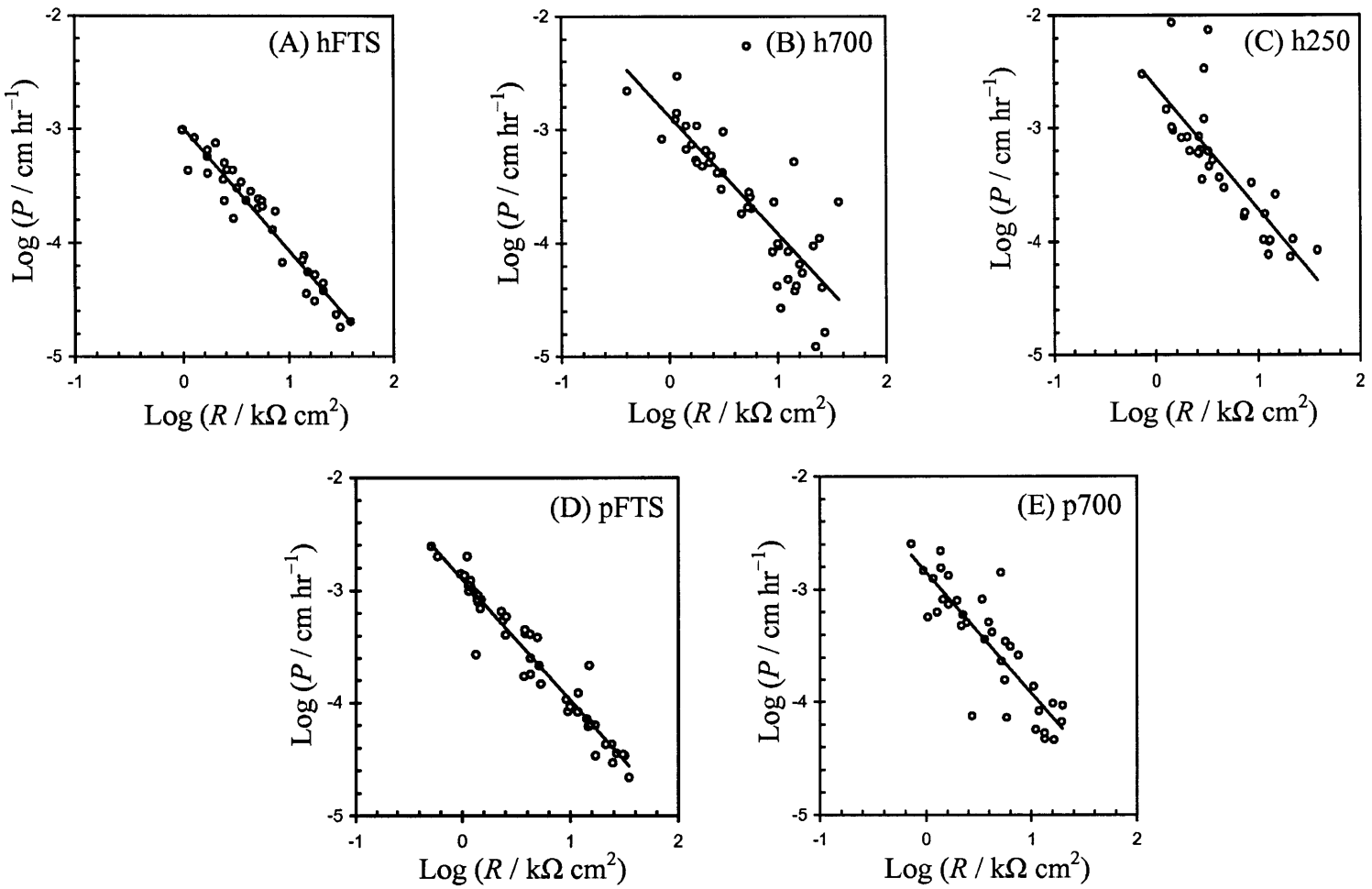

FIGURE 3-1: Comparison of the experimental log P – log R correlations: (A) hFTS, n = 36, (B) h700, n = 44, (C) h250, n = 34, (D) pFTS, n = 47, and (E) p700, n = 35. Each data point represents one experiment. The solid lines represent the linear regressions fitted to each data set. The statistical parameters associated with the linear regressions are listed in TABLE 3-1.

TABLE 3-1: Statistics for the log P – log R data set for each skin model.

Skin Type	Linear Regression Parameters			log C [a,c]
	Slope [a,b]	Intercept [a]	r^2	
hFTS	−1.08 ± 0.10	−2.99 ± 0.09	0.93	−3.05 ± 0.14
h700	−1.04 ± 0.23	−2.88 ± 0.20	0.66	−2.91 ± 0.36
h250	−1.09 ± 0.27	−2.63 ± 0.20	0.68	−2.69 ± 0.31
pFTS	−1.07 ± 0.08	−2.90 ± 0.07	0.94	−2.95 ± 0.16
p700	−1.07 ± 0.23	−2.85 ± 0.16	0.74	−2.89 ± 0.27

[a] Range corresponds to the 95% confidence interval.

[b] Slopes are not significantly different from −1.

[c] The average intercept value, log C, was obtained by extrapolating each data point to the y-axis using a slope of −1 (see Section 3.2.6). Log C is equivalent to the regressed intercept when the regressed slope is exactly −1.

Second, within each skin model investigated, r_{pore} does not vary significantly over the range of R values attained using US/SLS treatment.* In previous studies where US/SLS was applied to pFTS [33] and hFTS [52] to attain a range of R values, the results indicated that r_{pore} did not vary significantly with R (i.e. r_{pore} determined from mannitol delivery did not vary significantly with US/SLS dose). In this respect, the findings for the STS models investigated compare well with the findings for the well-established FTS models investigated and with the previous results reported in the literature for pFTS [33] and hFTS [52].

3.3.2 Comparison of Log P – Log R Correlations Among Skin Models

To compare the extent of structural perturbation within each US/SLS-treated human skin model, a statistical analysis was carried out to compare the regressed slopes and intercepts. For hFTS, h700, and h250, an analysis-of-covariance showed that there is no significant difference among the slopes of the three regression lines, but that the intercepts are significantly different. Pairwise t-tests further showed that the log C values for these three human skin models are significantly different. Recall that log C increases as r_{pore} increases (see Section 3.2.6). Physically, these results indicate that of the three human skin models, h250 undergoes the largest extent of structural perturbation (resulting in the largest r_{pore} value; see Table 3-2), while hFTS undergoes the smallest. These results strongly suggest that dermal thickness is significant during

* Recall that changes in r_{pore} affect the extrapolated intercept value from each data point (see Section 3.2.6). If r_{pore} varied significantly with the extent of skin structural perturbation induced by the US/SLS treatment, then the extrapolated intercepts would vary, and therefore, the regressed slope would be significantly different from -1 and/or the log P – log R correlation would be nonlinear. On the contrary, in Section 3.3.1, it was determined that the regressed slopes are -1 and that the linear regressions are statistically significant. Therefore, this indicate that within each skin model investigated, r_{pore} does not vary significantly over the range of R values attained using US/SLS treatment.

the *in vitro* US/SLS application to human skin.* Therefore, while all three human skin models investigated react to US/SLS in a manner that is well described by the porous pathway model, the three human skin models considered are not interchangeable.

Turning next to pFTS and p700, the statistical analysis described above showed that neither the slopes nor the intercepts of the two regressions are significantly different; therefore, the regression lines coincide. Subsequently, a *t*-test showed that there is no significant difference among the log *C* values (see TABLE 3-1) for pFTS and p700. This result implies that there is no significant difference among the r_{pore} values. Based on the results of the statistical comparison of the regressed slopes, regressed intercepts, and log *C* values for pFTS and p700, there is no significant difference between the structures of the hydrophilic transport pathways within these two pig skin models, which are therefore comparable. This indicates that the hydrophilic transport pathways within pFTS and p700 undergo similar extents of structural perturbation in response to the US/SLS treatment. This is an important finding that suggests that p700 may be utilized as an alternative skin model for *in vitro* studies of the US/SLS-enhanced transdermal delivery of hydrophilic permeants. The results further indicate that dermal thickness is not as significant during the *in vitro* US/SLS application to pig skin compared to human skin.

* The dermal thickness is not significant during the passive sucrose permeability experiments. The larger pore sizes observed in h700 and h250 cannot be attributed to the reduction of dermis in the passive permeability experiments, since the pores of the dermis are considered to be infinitely large in relation to sucrose. A reduction in the dermal layer with infinitely-large pores would logically result in a reduction in the skin model's effective aqueous pore size. On the contrary, the pore sizes of US/SLS-treated h700 and h250 were determined to be greater than that of hFTS (see Table 3-2). Therefore, one can conclude that the reduction in the dermis must play a more important role during the US/SLS pre-treatment phase than during the passive permeability experiments.

TABLE 3-2: Average values of the pore radii measured using sucrose as the probe permeant.

Skin Type	r_{pore} (Å) [a, b]		
	Low	Average	High
pFTS + p700 [c]	26	113	>120
hFTS	23	39	>120
h700	19	>120	>120
h250	55	>120	>120

[a] The low and high values correspond to the endpoints of the 95% confidence interval for r_{pore}.

[b] With sucrose as the probe permeant, the r_{pore} value of ∞ is obtained when $\log C \geq -2.86$. The physical significance of this value is that r_{pore} is significantly larger than the radius of sucrose (5.55 Å), such that the diffusion of sucrose through the aqueous pores is not sterically hindered. This limiting case has previously been studied by measuring the transdermal transport of small hydrophilic permeants through dermis, where the r_{pore} value is considered to be ∞ in relation to the size of the probe permeant since the dermis has a macroscopic porous structure [52,66]. Based on these studies (which utilized Eq. (3-4)), due to experimental error in determining the value of $\log C$, the porous pathway model did not distinguish between r_{pore} values of 100 Å and ∞ when used to quantify the transdermal diffusion of small hydrophilic permeants such as mannitol and sucrose [52,66]. Based on Eq. (3-5), which is more accurate than Eq. (3-4), the limit on r_{pore} becomes 120 Å. Note that permeants larger than sucrose will experience greater steric hindrance within the aqueous pores. Therefore, pore radii >120 Å may be measured using larger probe permeants.

[c] As discussed in Section 3.3.2, there is no significant difference among the $\log C$ values for the pig skin models investigated. Therefore, an r_{pore} value can be calculated from the combined $\log P - \log R$ data set for the two pig skin models [73].

Interestingly, the observed difference in the results for the pig and human skin models is reflected in the US/SLS treatment times for the skin models (see TABLE 3-3). The treatment times for pFTS and p700 are not significantly different, while the treatment times for the human skin models vary with skin thickness. Notably, there is a significant difference between the US/SLS treatment times for h700 and p700, which strongly suggests that intrinsic differences within pig and human skin (e.g. differences in dermal elastic fiber content [75]) are contributing to the differences in the results for pig and human skin. It is important to note that although pig and human skin are similar, they also display significant differences, as outlined in [75].

In comparing the r^2 values for the five skin models, note that those associated with STS are smaller than those associated with FTS (see TABLE 3-1). This difference is attributed to the greater variability in tension that one can experimentally impart onto STS (since it is thinner than FTS) when mounting skin into a diffusion cell. It has previously been proposed that skin permeability is affected by lateral strain in the skin [76]. Furthermore, the elasticity of a biomaterial (such as skin) is an important property that affects ultrasonic cavitation bubble dynamics and microjet formation in the fluid surrounding the biomaterial [77]. Therefore, variability in skin tension likely translates into variability in the mechanism of action of US/SLS on the skin, including more variability in the STS data. Additional experiments would be needed in order to test this hypothesis. In future studies, one should be cognizant of skin tension when mounting skin into a diffusion cell. The development of a procedure to mount STS into a diffusion cell with consistent skin tension may reduce the observed variability in the STS data.

TABLE 3-3: Net US/SLS treatment times for samples treated to attain R values of 1.5 ± 0.6 kΩ cm^2. [a]

Skin Type	n	Time (min) [b]
hFTS	8	10.6 ± 8.8
h700	10	5.1 ± 2.6
h250	6	2.8 ± 2.8
pFTS	14	2.5 ± 0.7
p700	10	2.9 ± 1.7

[a] The treatment times are reported for a small subset of the range of R values investigated (compared to the range investigated that spanned two orders-of-magnitude) in order to make useful statistical comparisons among the treatment times for the skin models. This range of R values was attained in an *in vivo* clinical study (reported in ref. [60] as mean ± SD). Up to 45 seconds of US/SLS treatment time was required to attain this range of R values in the clinical study [60]. However, it is important to note that the clinical ultrasonic skin permeation device was operated at a frequency of 55 kHz. It has previously been shown that the treatment time required to obtain a desired R value varies with US frequency [33,78]. However, by varying US frequency and US/SLS treatment time until different skin samples reach the same skin electrical resistivity value, the skin barriers are permeabilized to similar extents [33,58,78].

[b] Range corresponds to mean ± SD for n samples.

3.3.3 US/SLS-Enhanced Delivery of Gold Nanoparticles is Greater through p700 than through pFTS

The findings reported in Section 3.3.2 suggest that p700 can be considered to be an alternative skin model to pFTS. To illustrate why STS may be preferred over FTS in *in vitro* experiments in the case of macromolecules, gold nanoparticles were used as well-characterized, model hydrophilic macromolecular permeants to compare their US/SLS-enhanced transdermal delivery through pFTS and p700. In *in vitro* transdermal delivery experiments, hydrophilic molecules that permeate through the skin are ordinarily quantified in the receiver solution [79] because the dermis is not considered a significant barrier for these drugs. However, as proposed in this work, the dermis can also act as a barrier to hydrophilic macromolecules. Accordingly, the gold, present in the core of the gold nanoparticles studied, was analyzed both in the receiver solution and in the dermis.

Between pFTS and p700, there was no significant difference in the total amount of gold found in the dermis and the receiver solution (see Figure 3-2A), which indicates that the total amounts of gold nanoparticles penetrating past the epidermis (the major diffusion barrier to hydrophilic permeants) over 24 hours are similar. This finding is consistent with the conclusion that pFTS and p700 undergo similar extents of structural perturbation in response to the US/SLS treatment (see Section 3.3.2). Interestingly, the fraction of gold nanoparticles penetrating past the epidermis but remaining in the dermis after 24 hours was significantly larger when pFTS was used (see Figure 3-2B). This suggests that the thicker dermis in pFTS acts as a greater transdermal diffusion barrier to the gold nanoparticles, even though the gold nanoparticles are hydrophilic. It is speculated that the dermis may act as a reservoir (i.e. a diffusion sink) for absorbed macromolecules due to steric hindrance effects or interactions between the

macromolecules and the dermal components [7,49,50], or that there may be a longer lag time for macromolecular diffusion through the thicker FTS dermis (which would support the hypothesis that the dermis acts as an artificial barrier to hydrophilic macromolecules).

3.3.4 US/SLS-Enhanced Delivery of Quantum Dots is Greater through p700 than through pFTS

The experiments described in Section 3.3.3 were repeated using quantum dots as a second hydrophilic macromolecular permeant, and similar results were obtained. Between pFTS and p700, there was no significant difference in the total amount of cadmium found in the dermis and the receiver solution (see Figure 3-3A), which indicates that the total amounts of quantum dots clearing the epidermis (the major diffusion barrier to hydrophilic permeants) over 24 hours are similar. This finding is consistent with the conclusion that pFTS and p700 undergo similar extents of structural perturbation in response to the US/SLS treatment (see Section 3.3.2) and with the findings for gold nanoparticles in Section 3.3.3. The fraction of quantum dots clearing the epidermis but remaining in the dermis was slightly (but not significantly) larger when pFTS was used (see Figure 3-3B). This result is similar to the findings for gold nanoparticles, but the variability in the pFTS data (likely resulting from variability in the dermal thickness) was too great to detect a difference between pFTS and p700 at the 95% confidence level ($p = 0.077 > 0.05$). However, the amount of quantum dots reaching the receiver solution was still significantly greater in p700 than in pFTS (see Figure 3-3C), which is consistent with the findings for gold nanoparticles (see Figure 3-2C).

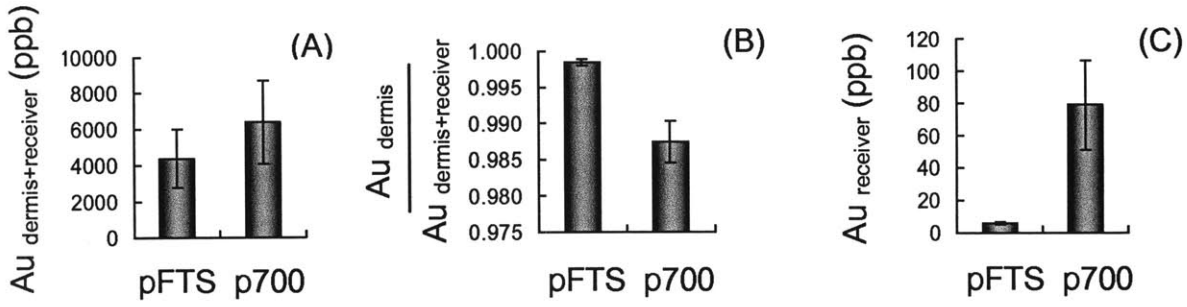

FIGURE 3-2: Quantification of gold (Au) in the dermis and in the receiver solution after 24 hours of gold nanoparticle diffusion through US/SLS-treated pFTS and p700. (A) Total amount of gold found in the dermis and receiver solution, indicating the total amount of gold nanoparticles penetrating past the epidermis. (B) Fraction of gold nanoparticles penetrating past the epidermis but remaining in the dermis. (C) Amount of gold found in the receiver solution. The amounts found in pFTS and p700 are not significantly different in (A) but are significantly different in (B) and (C). Data shown are the mean ± SD of n replicates; $n = 4$ for pFTS, $n = 5$ for p700.

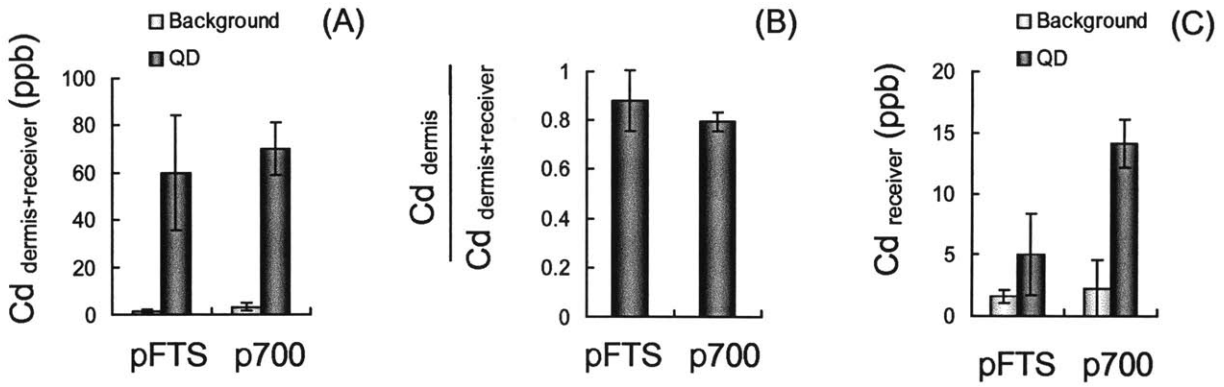

FIGURE 3-3: Quantification of cadmium (Cd) in the dermis and in the receiver solution after 24 hours of quantum dot (QD) diffusion through US/SLS-treated pFTS and p700. (A) Total amount of cadmium found in the dermis and receiver solution, indicating the amount of quantum dots penetrating past the epidermis. (B) Fraction of quantum dots penetrating past the epidermis but remaining in the dermis. (C) Amount of cadmium found in the receiver solution. The quantum dot amounts found in pFTS and p700 are not significantly different in (A) and (B) but are significantly different in (C). In (C), the background and quantum dot cadmium amounts measured using pFTS are not significantly different. Data shown are the mean ± SD of n replicates; $n = 6$ for quantum dots, $n = 3 - 7$ for background.

3.3.5 STRENGTHS AND WEAKNESSES OF THE SKIN MODELS INVESTIGATED

This section discusses the strengths and weaknesses of the skin models investigated. Excised human skin is considered the "gold standard" for *in vitro* transdermal studies. However, it is difficult to obtain regularly. Pig skin is a common animal skin model used in *in vitro* transdermal studies, particularly in US/SLS studies [28]. Excised pig skin is easier and cheaper to obtain than excised human skin, and the US/SLS treatment time for pig skin is shorter than that for human skin (see TABLE 3-3). Based on this comparison, pig skin is preferred over human skin.

Next, FTS and STS are compared. In the general transdermal field, STS is typically favored over FTS [80]. However, all previous *in vitro* US/SLS studies have been carried out with FTS [51-57], probably because STS had not been evaluated as a suitable *in vitro* skin model for US/SLS studies. One weakness of FTS is that its thickness varies with the location of skin procurement and the method used to remove the subcutaneous fat. The thickness of STS is much more uniform than that of FTS. However, there is more variability in the permeability data of US/SLS-treated STS (see the r^2 values in TABLE 3-1) compared to that of FTS. As discussed in Section 3.3.2, this variability may be minimized by mounting STS into a diffusion cell with consistent skin tension. If the variability cannot be adequately minimized, then one may need a larger number of replicates in a study using STS.

The choice of using STS or FTS depends on the final purpose of the study and on the permeant quantification methods available, including whether dermis solubilization is required to determine the amount of delivered permeant. It is generally easier to quantify the amount of permeant in the receiver solution than in the dermis because the sample collection is simpler and no tissue solubilization or extraction is required. If dermis solubilization is not required, then the

diffusion cell can be sampled at more than one time point, and the skin permeability (as defined in Eq. (3-1)) and absorption kinetics can be measured. Therefore, in spite of greater variability in the STS permeability data, one may choose to use STS to: (1) obtain a larger amount of delivered permeant into the receiver chamber solution for easier quantification (as shown in FIGURE 3-2C and FIGURE 3-3C), or (2) reduce the permeant donor concentration in order to obtain the same amount of permeant in the receiver solution that one would obtain using FTS, thereby reducing the amount and cost of material required for a study. On the other hand, if the amount of permeant in the receiver solution is below the limit of quantification for a desired method, then permeant quantification in the dermis using tissue solubilization may be required. In this case, it is beneficial to use p700 over pFTS because the dermis thickness is less variable (note that in FIGURE 3-3, the quantum dot amounts in p700 were less variable than in pFTS). The above issues are particularly important in the case of hydrophilic macromolecules, which pass through skin in low amounts and may not attain steady state transdermal diffusion within 24 hours.

3.4 CONCLUSIONS

The log P – log R correlations between pig and human FTS and STS were compared in the context of the aqueous porous pathway model, which was utilized to characterize the extent of structural perturbation of the hydrophilic transdermal transport pathways in response to US/SLS treatment. For the US/SLS conditions and the range of R values considered, US/SLS enhances P in each skin model in a predictable manner that is well-described by the porous pathway model. The key result of the investigation is that pFTS and p700 respond similarly to US/SLS treatment, while hFTS, h700, and h250 respond differently to US/SLS. The significant difference in US/SLS treatment times for p700 and h700 strongly suggests that the difference in

the results for pig and human skin is due to intrinsic differences within pig and human skin. In comparing FTS and STS, it was shown that STS permeability data may be more variable, but the thicker dermis in FTS acts as a greater transdermal diffusion barrier to macromolecules (demonstrated using gold nanoparticles and quantum dots as model hydrophilic macromolecular permeants; this result is graphically depicted in FIGURE 3-4). Because the dermis acts as an artificial diffusion barrier, and pig skin is more readily obtained and responds faster to the US/SLS treatment compared to human skin, the findings strongly suggest the use of p700 for future *in vitro* studies on the US/SLS-enhanced transdermal delivery of hydrophilic permeants (particularly, hydrophilic macromolecules).

Based on the results presented in this chapter, the original goal of investigating the transdermal delivery of quantum dots (see Section 3.0) was pursued, using pig STS. In the next chapter, then, the US/SLS-enhanced delivery of quantum dots was investigated using complementary qualitative and quantitative methods (confocal fluorescence microscopy and elemental analysis, respectively). In addition to the advantages of using STS described in Section 3.3.5, the use of STS in Chapter 4 provided additional benefits. Because STS has minimal variation in dermal thickness, the use of STS reduced the variability in: (i) the amount of quantum dots quantified in the dermis by elemental analysis (see Section 4.2.6.1), and (ii) the compression of the skin when it is mounted into an imaging chamber for confocal microscopy analysis (see Section 4.2.6.2), which affects the observed quantum dot penetration depth.

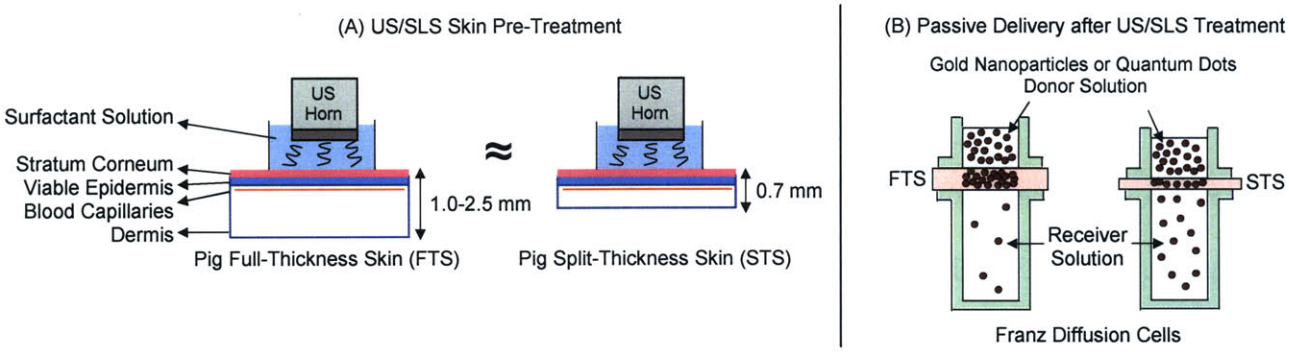

FIGURE 3-4: Graphical depiction of key results. (A) Pig FTS and STS respond similarly to the US/SLS treatment. (B) Macromolecules (gold nanoparticles and quantum dots) clear the STS dermis and reach the receiver solution in greater amounts.

3.5 APPENDIX A: METHODS TO PREPARE US/SLS-TREATED SPLIT-THICKNESS SKIN

Two methods may be utilized to prepare US/SLS-treated STS: (1) treat FTS with US/SLS, and then use a dermatome to obtain US/SLS-treated STS, or (2) dermatome untreated FTS to obtain STS, and then treat the STS with US/SLS.

Method (1) would really be the ideal method for preparing skin so that studies such as the one described in this chapter are not necessary to validate STS of various thicknesses for US/SLS treatment. However, from a practical standpoint, Method (1) is inefficient and not feasible. FIGURE 3-5 illustrates why Method (1) is not practically *feasible*. Skin must be clamped firmly into the Franz diffusion cell in order to ensure accurate measurements of R to meet initial skin structural integrity requirements as described in Section 3.2.3. In addition, skin is clamped firmly during the US/SLS treatment. Recall that the treatment times reported in TABLE 3-3 are *net* US/SLS treatment times. Since US is applied in a pulsed mode with an on/off ratio of 1:1 (see Section 3.2.4), a sample treated with US/SLS for one *net* minute really spends two minutes under the US horn. Furthermore, in order to minimize the temperature rise in the coupling medium and to determine if the desired value of R has been reached, at least once every two minutes of US/SLS treatment, it takes ~1 minute to replace the 1% SLS coupling medium with PBS, measure R, and replace the PBS with 1% SLS coupling medium for the next US/SLS treatment period. Therefore, the total time that a skin sample is firmly clamped into a diffusion cell during US/SLS treatment can be as long as 1 hour, particularly for the hFTS samples. From experience, the outer, greased, and partially compressed skin area does not recover from being clamped in a diffusion cell after US/SLS treatment. Because of this, it would be very difficult to dermatome an uneven skin surface after US/SLS treatment.

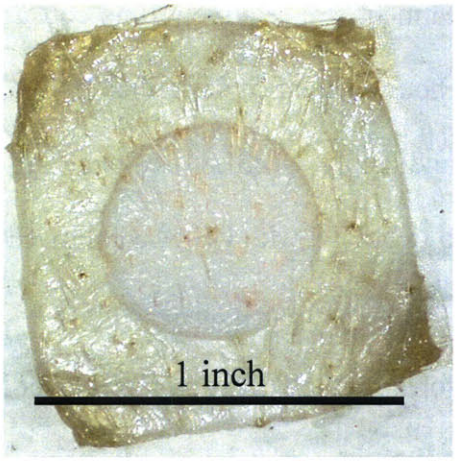

FIGURE 3-5: Skin, after being clamped in a diffusion cell for US/SLS treatment. The small, unclamped area in the center would be difficult to dermatome.

Furthermore, assuming that one could dermatome just the unclamped surface of the skin that is exposed to US/SLS treatment, then the resulting STS would need to be mounted into a smaller diffusion cell for the subsequent passive permeation experiment. However, US/SLS treatment enhances skin permeability in a heterogeneous manner, producing localized transport regions (LTRs) of greatly enhanced permeability compared to the surrounding regions of US/SLS-treated skin (see Chapter 1, Section 1.4.3). Typically, LTRs cluster in the center of the exposed skin beneath the US probe [28,51,81]; therefore, mounting the resulting STS into a smaller diffusion cell may artificially enhance the skin permeability. Until LTR formation is transformed into a homogeneous phenomenon, this alternative protocol is not feasible.

Second, Method (1) is *inefficient* because it is difficult to preserve the structural integrity of the skin while dermatoming. From experience, dermatoming compromises ~20% of the skin (as quantified by comparing the percentage of FTS and STS samples that have an initial R value $> 50\ k\Omega\ cm^2$). In addition, dermatoming is a relatively quick step in the experimental protocol.

On the other hand, US/SLS treatment is a relatively time consuming step of the protocol, with some samples taking up to 1 hour to treat as described above. Therefore, it would be more efficient to dermatome skin and apply US/SLS treatment to the samples that are deemed structurally intact, rather than to treat FTS with US/SLS followed by dermatoming, which would structurally compromise ~20% of the US/SLS-treated samples.

For all of the above reasons, Method (2) is preferred over Method (1) because it would be more efficient and practical to first dermatome FTS and then verify that the resulting STS is structurally intact (see Section 3.2.3) before applying US/SLS treatment to the STS.

3.6 APPENDIX B: PIG STS WITH THICKNESSES ≤ 450 μM ARE NOT SUITABLE FOR US/SLS STUDIES

Pig skin was dermatomed to thicknesses of 300 – 400 μm, and the skin permeabilities to sucrose (with and without US/SLS enhancement) were compared to that of 700-μm thick pig STS. The resulting skin permeabilities to sucrose were significantly more variable and greater than that of 700-μm thick STS (see FIGURE 3-6). Subsequently, pig STS of 450-μm thickness was prepared, and the skin permeabilities to sucrose (with and without US/SLS enhancement) were measured. The passive skin permeability to sucrose was similar to that of 700-μm STS (see FIGURE 3-6). However, after treating 450-μm thick STS with US/SLS, the enhanced skin permeability to sucrose was not reproducible and was significantly higher than that of 700-μm STS (see FIGURE 3-6). This suggests that the pig skin membrane at this thickness is too fragile to withstand the US/SLS treatment. It is likely that the mechanical action of US/SLS was forceful enough to enlarge the hair shafts in the pig skin into macroscopic holes. Additional studies are

required to investigate intermediate thicknesses between 700 μm and 450 μm in order to determine the threshold thickness for which pig STS is suitable for US/SLS studies.

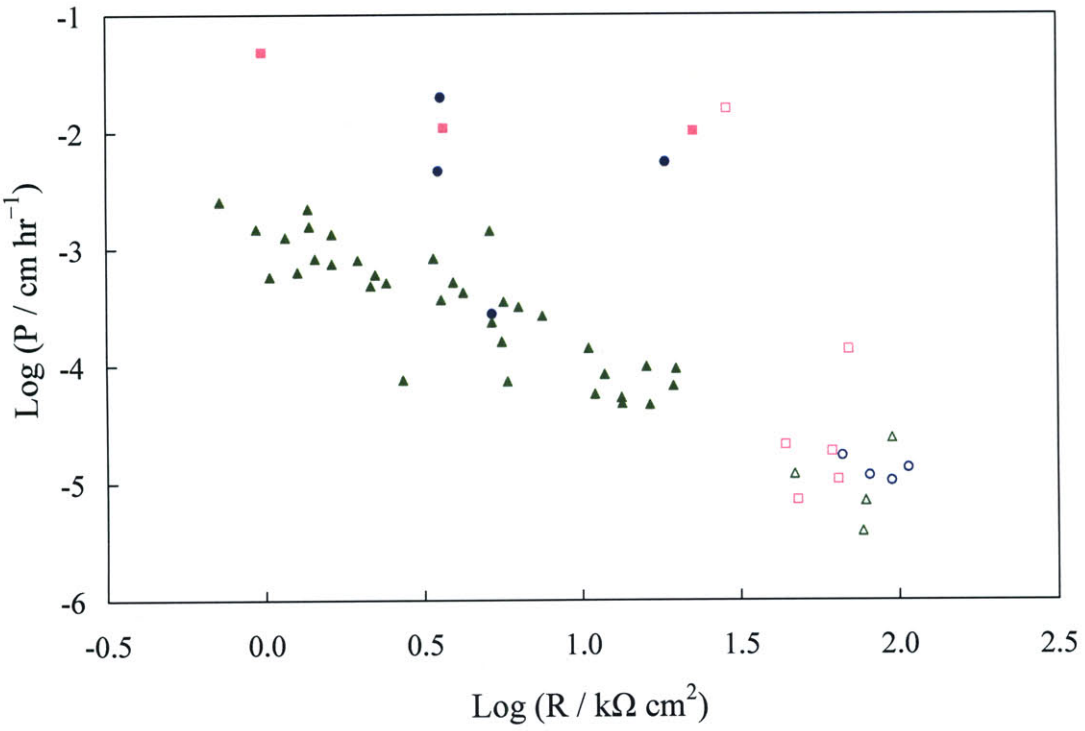

FIGURE 3-6: Evaluation of log P – log R correlations for pig STS with thicknesses ≤ 700 μm for passive and US/SLS-enhanced diffusion experiments. Each data point represents one experiment.

Figure Key

□ 300 – 400 μm thick skin, untreated

■ 300 – 400 μm thick skin, US/SLS-treated

○ 450 μm thick skin, untreated

● 450 μm thick skin, US/SLS-treated

Δ 700 μm thick skin, untreated

▲ 700 μm thick skin, US/SLS-treated

3.7 APPENDIX C: VALIDITY OF EQUATION (3-1) AT STEADY-STATE, SINK CONDITIONS

Equation (3-1) is only valid under the following conditions: (a) steady-state diffusion is attained before the sampling period (i.e. the concentration gradient across the skin is constant and the rate of sucrose accumulation in the receiver chamber is constant), and (b) the donor solution behaves as an infinite source (i.e. the donor concentration is constant and is significantly greater than the receiver concentration). In each diffusion experiment, if significant experimental error was evident, or if the experimental conditions required for Eq. (3-1) to be valid were not maintained, the diffusion data were discarded.

Note that diffusion cells were sampled manually, and not with an autosampling system. With manual sampling, there were many opportunities for experimental error to occur. In order to ensure that significant experimental error did not occur, three conditions (denoted below as I, II, and III) were used to evaluate the consistency of the data from each diffusion experiment (note that conditions (II) and (III) refer to the linear regression that was used to calculate $\Delta C/\Delta t$ from the five data points generated from the receiver solution aliquots; see Section 3.2.5): (I) For each sampling time point, the difference in concentration between the donor and the receiver solutions ($C_d - C_r$) was calculated. Then, the maximum relative change in ($C_d - C_r$) over the five time points was calculated as $1 - ((C_d - C_r)_{min}/(C_d - C_r)_{max})$. If this value was greater than 7.9% (the basis for selecting this threshold is discussed below), then the data were discarded because conditions (a) and (b) above were not maintained; (II) If the correlation coefficient (r^2) of the regression was less than 0.771 (this threshold value was calculated using an analysis-of-variance, which requires that the slope of a linear regression computed from five data points be significantly different from zero [82]), then the linear regression was not statistically significant.

Therefore, the data were discarded because condition (a) above was not maintained; and (III) If the lower bound of the 95% confidence interval for the y-intercept of the regression was positive, i.e. the entire 95% confidence interval was positive, then the data were discarded because this corresponds to a non-zero ^{14}C concentration in the receiver chamber at the start of the diffusion experiment. The above conditions resulted in discarding data from 20% of the experiments. The use of an autosampling system would likely improve the protocol by reducing the number of opportunities for experimental error to occur.

Regarding condition (I), the 7.9% threshold value was chosen because it is one standard deviation greater than the average value of 2.89 ± 4.99% (mean ± SD; this is the experimental error in measuring the concentration difference across the skin at steady-state, sink conditions). This experimental error was calculated using the data set from the diffusion experiments conducted for this study. After applying conditions (II) and (III) to the dataset, there were 209 skin samples from which the threshold was calculated. Based on this threshold, 13 samples were discarded. The data from the remaining 196 skin samples are reported in this chapter.

CHAPTER 4

QUANTITATIVE AND QUALITATIVE METHODS FOR EVALUATING THE TRANSDERMAL DELIVERY OF NANOPARTICLES *

4.1 INTRODUCTION

The evaluation of skin penetration of rigid nanoparticles (e.g. metallic and polymeric) and soft nanoparticles (e.g. liposomes and transfersomes) has recently attracted significant attention [50,83]. This chapter focuses on rigid nanoparticles. Rigid nanoparticles are being investigated for: (i) designing transdermal drug carriers (e.g. [84,85]), (ii) elucidating their mechanism of transdermal penetration (e.g. [86]), and (iii) evaluating their biocompatibility (e.g. [87]). Compared to traditional topical formulation strategies, drug-loaded nanoparticles offer advantages which include protection of unstable active agents against degradation and prolonged release of active agents [83]. In addition, the physicochemical properties of the active agents are masked, and the physicochemical properties of the nanoparticle carrier (e.g. size, surface charge, hydrophilicity, and shape [88-90]) can be designed to enhance the transdermal delivery of the active agent. Furthermore, the nanoparticle carrier can be targeted to deliver the drug to specific skin components, such as dendritic cells [91].

* Most of this chapter has been reproduced from RFV Lopez†, JE Seto†, D Blankschtein, and R Langer. Enhancing the transdermal delivery of rigid nanoparticles using the simultaneous application of ultrasound and sodium lauryl sulfate. Biomaterials 32, 933-941 (2011). †co-first authors

While rigid nanoparticles have potential as transdermal drug carriers, the penetration of nanoparticles into the skin is significantly inhibited by the skin's inherent barrier properties. Many studies have qualitatively shown that skin penetration is primarily limited to the stratum corneum, the outermost skin layer (e.g. [90,92,93]). The ability of nanoparticles to penetrate into the dermis has been debated, based on visual observations made using confocal microscopy (e.g. [88-90,92]). The conflicting reports suggest that nanoparticle penetration into the dermis may occur in very small amounts (e.g. [89]), but this amount has not been quantified previously. Clearly, the success of nanoparticles as transdermal drug carriers depends on the ability of the carrier to penetrate the skin at sufficient depths and in sufficient quantities.

In order to improve nanoparticle skin penetration, one may consider several methods that have been developed to enhance skin permeability [83]. One method, the simultaneous application of low-frequency ultrasound and the surfactant sodium lauryl sulfate (referred to as US/SLS), has received FDA approval as a skin treatment method for enhancing topical lidocaine uptake [37]. US/SLS has also been used to enhance the transdermal delivery of therapeutic macromolecules *in vivo* [46]. This chapter reports on the first investigation of the application of US/SLS treatment to enhance the passive skin penetration of rigid nanoparticles.

There is significant evidence that the extent of nanoparticle skin penetration depends on the surface charge of the nanoparticle (e.g. [88,90]). Therefore, this investigation compared the penetration of cationic, neutral, and anionic nanoparticles into US/SLS-treated and untreated skin. Quantum dots (QDs) are the nanoparticles selected for this study because: (i) QDs can be coated with various ligands, and therefore, QDs of various surface charges can be obtained, and (ii) their fluorescent properties allow for the visualization of their transdermal route of penetration. More specifically, this investigation compared the following properties of 10- and

20-nm cationic, neutral, and anionic QDs: (a) the penetration of these QDs into US/SLS-treated skin and untreated skin, and (b) the penetration pathway of these nanoparticles. Based on the findings, conclusions are drawn regarding the potential of US/SLS as a method to enhance the skin penetration of nanoparticle drug carriers.

4.2 MATERIALS AND METHODS

4.2.1 CHEMICALS

Phosphate buffered saline (PBS) tablets and SLS solution (20 w/v% in water) were obtained from Sigma-Aldrich (St. Louis, Missouri). PBS was prepared from PBS tablets according to the manufacturer's instructions. NaCl was obtained from Mallinckrodt (Paris, Kentucky). 70% isopropanol wipes were obtained from VWR (West Chester, Pennsylvania). Deionized water dispensed from a Milli-Q academic water purification system (Millipore, Bedford, Massachusetts) was used to prepare solutions. The chemicals used for the ICP-MS analysis (see Section 4.2.6.1) are provided in Chapter 3, Section 3.2.1.

4.2.2 QUANTUM DOTS (QDS)

Spherical, water soluble, CdSe/ZnS quantum dots with one of three different surface groups were obtained from Ocean NanoTech (Springdale, Arkansas). The surface groups include: (1) cationic polydiallyl dimethyl ammonium chloride, (2) anionic carboxylic acid, and (3) neutral amine. The physicochemical properties of the four QDs studied, referred to hereafter as QDs A – D, are listed in TABLE 4-1. QD hydrodynamic diameter and zeta potential measurements were performed at 25°C using a ZetaSizer ZS90 (Malvern Instruments, Malvern, Worcestershire, England). QD solutions were dialyzed (as described in Chapter 3, Section

3.2.8.1) and 0.2-μm filtered prior to analysis. Size measurements were performed at count rates of 100 – 130 kcps. Sizes were obtained from a volume-based particle size distribution. Zeta potentials were measured at the physiologically relevant pHs of 5 and 6 [94]. For zeta potential measurements at pH 6, QDs were dispersed in 10% PBS. For zeta potential measurements at pH 5, QDs were dispersed in 1% PBS, and NaCl was added such that the ionic strength of the solution was equal to that of 10% PBS. Zeta potentials were calculated from electrophoretic mobilities using the Smulochowski approximation.

TABLE 4-1: Physicochemical properties of the QDs.

QD	Hydrodynamic diameter (nm) [b]	Zeta potential (mV) at pH 5 [c]	Zeta potential (mV) at pH 6 [c]	Classification
A [a]	9.9 ± 0.8	−27.6 ± 3.2	−27.0 ± 1.7	Anionic
B	21.0 ± 0.6	−1.2 ± 0.3	−2.5 ± 3.2	Neutral
C	21.8 ± 1.2	27.6 ± 0.8	26.9 ± 1.3	Cationic
D	21.4 ± 2.0	36.9 ± 1.1 [d]	30.0 ± 1.6 [d]	Cationic

[a] This is the largest anionic QD available from this vendor.

[b] Mean ± SD of 6 – 9 measurements.

[c] Mean ± SD of 3 – 6 measurements.

[d] QD D is more cationic than QD C ($p < 0.05$).

4.2.3 SKIN PREPARATION

The following methods have been described in detail in Chapter 3, Sections 3.2.2 and 3.2.3. Briefly, 700-μm thick pig split-thickness skin (STS) samples were prepared according to a protocol which was approved by the Committee on Animal Care at MIT. Then, each skin sample was mounted in a Franz diffusion cell (PermeGear, Hellertown, Pennsylvania) with a 15-mm inner diameter. Any skin sample having an initial electrical resistivity of < 50 kΩ cm^2 was considered damaged and was discarded.

Pig STS, which has minimal variation in dermal thickness, was used in order to minimize variation in: (1) the amount of QDs quantified in the dermis by ICP-MS (see Section 4.2.6.1), and (2) the compression of the skin (when it is mounted into an imaging chamber for confocal microscopy analysis; see Section 4.2.6.2), which affects the observed QD penetration depth. In addition, Chapter 3 showed that pig STS is a convenient skin model for investigating the *in vitro* US/SLS-enhanced transdermal delivery of hydrophilic macromolecules, including one of the QDs studied in this chapter (QD C).

4.2.4 US/SLS TREATMENT OF SKIN

US/SLS treatment was applied to some of the skin samples until the desired skin electrical resistivity value of 1.25 ± 0.25 kΩ cm^2 was attained,* using the method described in Chapter 3, Section 3.2.4, which is summarized next: US, with the probe tip immersed in a coupling medium containing 1 w/v% SLS in PBS, was applied to the skin samples with a VCX 500 and a coupler probe (Sonics & Materials, Newtown, Connecticut) at the following typical US conditions [28]: frequency - 20 kHz, intensity - 7.5 W/cm^2, pulse length - 5 seconds on, 5

* This range of skin electrical resistivity values was attained in a US/SLS clinical study [60].

seconds off, and distance between the probe tip and the skin - 3 mm. The US intensity was calibrated using calorimetry. The US/SLS treatment was stopped at least every minute to determine if the desired skin electrical resistivity value was attained, as well as to replace the coupling medium with a fresh one (to minimize thermal effects).

4.2.5 Transdermal Delivery of QDs

US/SLS-treated and untreated skin samples were mounted into clean, dry Franz diffusion cells. 12 mL of PBS was added to the receiver chambers, and 0.25 mL of 1 μM QDs in water was added to the donor chambers. Passive diffusion experiments were conducted for 24 hours at room temperature (25°C) and under occluded conditions by sealing the donor chambers and sampling ports with parafilm. The receiver solutions were magnetically stirred at 400 RPM. Control experiments were also conducted with water in the donor chamber for: (1) measuring background cadmium amounts (recall that cadmium is present in the core of the QDs) for ICP-MS analysis (see Section 4.2.6.1), and (2) configuring confocal microscopy settings (see Section 4.2.6.2).

4.2.6 Analysis of QD Skin Penetration

In *in vitro* transdermal delivery experiments, molecules that permeate the skin are ordinarily quantified in the receiver solution [79]. However, it was shown in Chapter 3 that the dermis acts as a significant diffusion barrier to QDs. Therefore, both the receiver solution and the dermis were analyzed for the presence of QDs.

Immediately following the end of each diffusion experiment, the receiver solution and the skin sample were collected. To prepare the receiver solution for ICP-MS analysis, the receiver

solution was dialyzed to reduce the amount of PBS salts (see Chapter 3, Section 3.2.7.1). Then, the entire volume of the dialyzed receiver solution was analyzed by ICP-MS. From each skin sample, the skin area that was exposed to US/SLS treatment and subsequent passive application of QDs (1.77 cm^2) was cleaned carefully with isopropanol and PBS and then isolated using scissors. Then, the STS sample was either analyzed by confocal microscopy or further prepared for analysis of QD penetration into the dermis. For the latter analysis, the epidermis was mechanically separated from the dermis using a spatula [71]. Then, the exposed dermal surface was cleaned with isopropanol and PBS in order to minimize potential contamination resulting from inadvertently transferring QDs from the epidermis to the dermis. Finally, the isolated dermis sample was analyzed by either ICP-MS or confocal microscopy as described next.

4.2.6.1 Quantification of QD Penetration by ICP-MS

Inductively coupled plasma-mass spectrometry (ICP-MS) was performed using a PlasmaQuad 2+ Quadrupole Mass Spectrometer (Fisons Instruments, Merrimac, Massachusetts) to quantify the amount of ^{111}Cd (cadmium, an element of the QD core) in the receiver solutions and the dermis samples based on a previously published method [72]. The Cd amounts were converted into QD concentrations using calibration plots for each QD studied. It was verified that the skin did not interfere in the quantification of QDs by contacting STS with known concentrations of QDs.

The quantification limit for each type of QD considered (see Table 4-1) was established as follows: Background Cd amounts were determined using at least three controls (see Section 4.2.5) in each set of experiments. The maximum amount of Cd found in these controls was doubled; this factor of 2 was chosen to reasonably distinguish between QD and background Cd

levels. Using this method, the following quantification limits were determined: (i) 0.007 pmol for QD A, (ii) 0.019 pmol for QD B, (iii) 0.118 pmol for QD C, and (iv) 0.004 pmol for QD D. Note that in order to obtain these quantification limits, (1) all glassware, stirbars, and polyfluor alkoxy vials needed to be meticulously cleaned, and (2) in Section 4.2.5, the Ag/AgCl electrodes were not introduced into the receiver chamber of the diffusion cells in order to minimize the presence of trace metals. Detailed ICP-MS protocols are provided in the Appendix, Section 4.6.

For each US/SLS-treated skin sample, the following two quantities were calculated: (1) the total amount of QDs penetrating past the epidermis (the major transdermal diffusion barrier), which corresponds to the sum of the amount of QDs quantified in the dermis and in the receiver chamber, and (2) the fraction of QDs that penetrated past the epidermis and remained in the dermis, which corresponds to the amount of QDs quantified in the dermis divided by (1).

4.2.6.2 Visualization of QD Penetration by Confocal Microscopy

Within 1 – 3 hours after the QD skin penetration experiments, STS samples and dermis samples were examined using a LSM 510 confocal microscope, Plan-Neofluar 10x/0.3 objective, and AIM 4.2 software (Carl Zeiss, Jena, Germany). Skin samples were inserted into a 0.5-mm thick imaging chamber (Coverwell PCI-A-0.5, Grace Bio-Labs, Bend, Oregon) with PBS as the mounting medium. The imaging chamber was sealed on both sides with a No. 1.5 glass coverslip. Confocal images were obtained in the plane parallel to the sample surface (xy-mode), and optical sections were made in the z-stack mode. All images are 900 μm x 900 μm. Skin samples without QDs were used as negative controls for configuring the microscope settings.

The top surface of the STS samples or of the dermis samples was defined by the scanning depth yielding the highest average fluorescence intensity [86]. After examining the top surface,

the samples were turned upside-down, and the underside of the dermis was also examined in search of deep QD penetration into the dermis. As a visual aid, a mark on the coverslip was used to identify the bottom surface of the dermis.

In all figures, a red color scheme is utilized to illustrate routes of QD penetration. In addition, as indicated in the figure captions for FIGURE 4-2C, FIGURE 4-2D, FIGURE 4-4B, FIGURE 4-5B, and FIGURE 4-6, these images were processed using ImageJ software (National Institutes of Health, Bethesda, Maryland) [95]. The brightness and contrast of the specified images was adjusted first by using the 'Auto' feature in order to enhance the visibility of the regions of QD penetration, and second by increasing the minimum displayed pixel value. These adjustments were propagated to three control images to ensure that the control images remained black. For all images, it is important to recognize that they serve to provide *qualitative* information regarding routes of QD penetration.

4.2.7 STATISTICAL ANALYSIS

Two-sample, two-tailed *t*-tests assuming unequal variances were used to compare QD amounts and zeta potentials. In all analyses, p values < 0.05 were considered to be statistically significant.

4.3 RESULTS

4.3.1 QUANTIFICATION OF QD PENETRATION INTO UNTREATED SKIN

The QDs penetrated into the dermis of untreated skin (see TABLE 4-2, Dermis of untreated skin), but QD permeation across the skin and into the receiver chamber of the Franz diffusion cell setup was not quantifiable using ICP-MS (not shown). Among the four QDs, QD C

penetrated into the dermis in the largest amounts (0.078% of the applied dose), in spite of the fact that it was not the most cationic QD. QD A penetrated the skin in the smallest amounts (0.006%), in spite of the fact that it was the smallest QD.

4.3.2 Quantification of QD Penetration into US/SLS-Treated Skin

The US/SLS treatment significantly enhanced the penetration of the QDs past the epidermis (see Table 4-2, Total) by 500 – 1300%. In most cases, QDs fully permeated US/SLS-treated skin and reached the receiver chamber in quantifiable amounts (see Table 4-2, Receiver). QD C penetrated the skin in the largest amounts, while QD A penetrated the skin in the smallest amounts. For all four QDs, the fraction of QDs that penetrated past the epidermis and remained in the dermis was high, ranging from 0.80 to 0.99 (see Table 4-2, Dermis/Total). Interestingly, the two cationic QDs (C and D) exhibited very different behaviors once they penetrated past the epidermis; out of the four QDs studied, QDs C and D exhibited the smallest and largest fractional retentions in the dermis, respectively.

TABLE 4-2: Quantification of QD skin penetration after 24 hours of diffusion. Data shown are the mean ± SD of *n* replicates; $n = 5 - 6$ for US/SLS-treated skin, $n = 3 - 5$ for untreated skin.

QD	Dermis of untreated skin (pmol)	US/SLS-treated skin			
		Dermis (pmol)	Receiver (pmol)	Total (pmol) [a]	Dermis/Total
A	0.015 ± 0.006	0.115 ± 0.024	0.007 ± 0.006 [b]	0.122 ± 0.025	0.945 ± 0.045
B	0.113 ± 0.055	0.644 ± 0.098	0.044 ± 0.031	0.689 ± 0.095	0.935 ± 0.043
C	0.195 ± 0.055	1.054 ± 0.218	0.244 ± 0.039	1.311 ± 0.239	0.800 ± 0.026
D	0.042 ± 0.021	0.582 ± 0.236	0.006 ± 0.005 [b]	0.587 ± 0.238	0.990 ± 0.006

[a] Total = Dermis + Receiver. These amounts are significantly greater than the QD amounts quantified in the dermis of untreated skin ($p < 0.05$).

[b] In two of the individual skin samples included in this average, the amount of QDs in the receiver chamber was below the quantification limit (see Section 4.2.6.1).

4.3.3 VISUALIZATION OF QD TRANSDERMAL PENETRATION PATHWAYS

Confocal microscopy was used to obtain images of selected skin regions of interest, where QDs penetrated into the stratum corneum and the dermis. These images were used to corroborate the ICP-MS results regarding QD penetration into the dermis and the receiver chamber. Furthermore, these images provided qualitative information regarding the nature and depth of QD penetration into US/SLS-treated skin and untreated skin. It is important to recognize that the images presented here are regions of interest, in the sense that QD penetration was not observed in the majority of the skin. Instead, QD fluorescence was localized in some hair follicles (see FIGURE 4-1) and in regions with diameters typically on the order of 5 μm, but occasionally ranging up to 300 μm for untreated skin and up to 500 μm for US/SLS-treated skin. Furthermore, the regions of QD penetration were generally smaller and observed less frequently in untreated skin compared to those in US/SLS-treated skin.

FIGURE 4-2 serves to highlight several aspects of QD transdermal penetration. Based on FIGURE 4-2, one can observe that: (1) the intensity of the QD fluorescence in the surface of the stratum corneum (see FIGURE 4-2B) and in the section of the dermis at a depth of 25 μm (see FIGURE 4-2D) of US/SLS-treated skin are both higher than those of untreated skin (see FIGURE 4-2A and FIGURE 4-2C, respectively). This corroborates the findings based on ICP-MS that US/SLS treatment of the skin enhances QD penetration into the skin; (2) QDs penetrate into both US/SLS-treated skin and untreated skin in localized regions (i.e. the distribution of QDs in the skin is heterogeneous; additional examples are provided in FIGURE 4-3); (3) US/SLS treatment increases the fractional surface area of skin through which QD penetration occurs (i.e. the amount of red in FIGURE 4-2B and FIGURE 4-2D is greater than that in FIGURE 4-2A and FIGURE 4-2C, respectively); and (4) QDs penetrate into the dermis of untreated skin (see FIGURE 4-2C),

which provides visual confirmation of the ICP-MS result in TABLE 4-2. Observations (1) – (4) were made for all four QDs studied. The number and size of QD penetration regions varied among the QDs, but the discrete nature of QD skin penetration and the increased amount of QD penetration into US/SLS-treated skin compared to that of untreated skin was consistently observed for all four QDs studied.

Both FIGURE 4-4 and FIGURE 4-5 serve to corroborate the difference in ICP-MS results for the penetration of the cationic QDs into US/SLS-treated skin (see Section 4.3.2). QD C was observed to penetrate more deeply into the dermis (see the 55.0 μm depth image in FIGURE 4-4A). In addition, the QD fluorescence was observed in the bottom layers of the dermis (see FIGURE 4-4B). This confirms the uptake of QD C into the deeper portions of the dermis, thus corroborating the ICP-MS analysis which indicated the presence of these QDs in the receiver chamber (see TABLE 4-2). On the other hand, while QD D was visually confirmed to penetrate into the dermis, the fluorescence intensity decreased significantly with penetration depth (see FIGURE 4-5A). QD D was observed in the bottom layers of US/SLS-treated skin (see FIGURE 4-5B). However, these regions of deep dermal penetration were small and difficult to find. Note that only two regions of fluorescence are visible in FIGURE 4-5B, while hundreds of small regions of fluorescence are visible in FIGURE 4-4B, indicating that QD C was more evenly distributed throughout the bottom layers of the dermis. These observations are consistent with the quantitative findings using ICP-MS which indicated that QD C reached the receiver chamber in greater amounts compared to QD D.

Finally, in untreated skin, QDs were observed to penetrate into the dermis (e.g. see FIGURE 4-6), but were not observed in the bottom layers of the dermis (not shown). This corroborates the ICP-MS finding that without US/SLS enhancement, QDs did not reach the receiver chamber in quantifiable amounts.

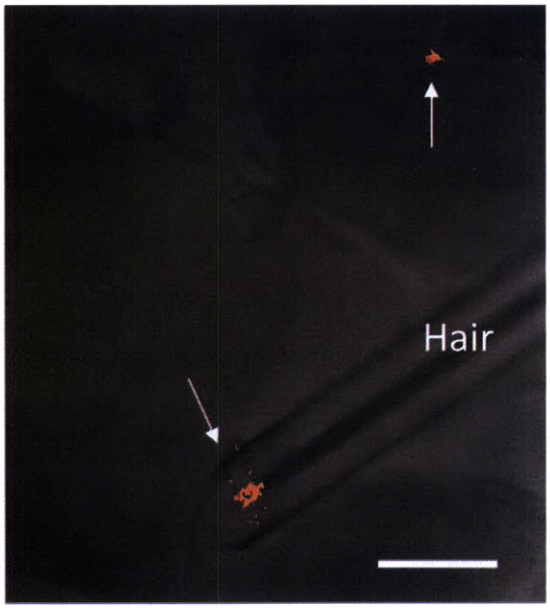

FIGURE 4-1: QD D penetration into US/SLS-treated skin in patches that were not limited to within hair follicles. Optical section of the isolated dermis, made parallel to the epidermis-dermis surface at a depth of 10 μm below the surface. The arrows indicate regions of QD penetration. The image is an overlay of fluorescence and bright-field images. Bar = 200 μm.

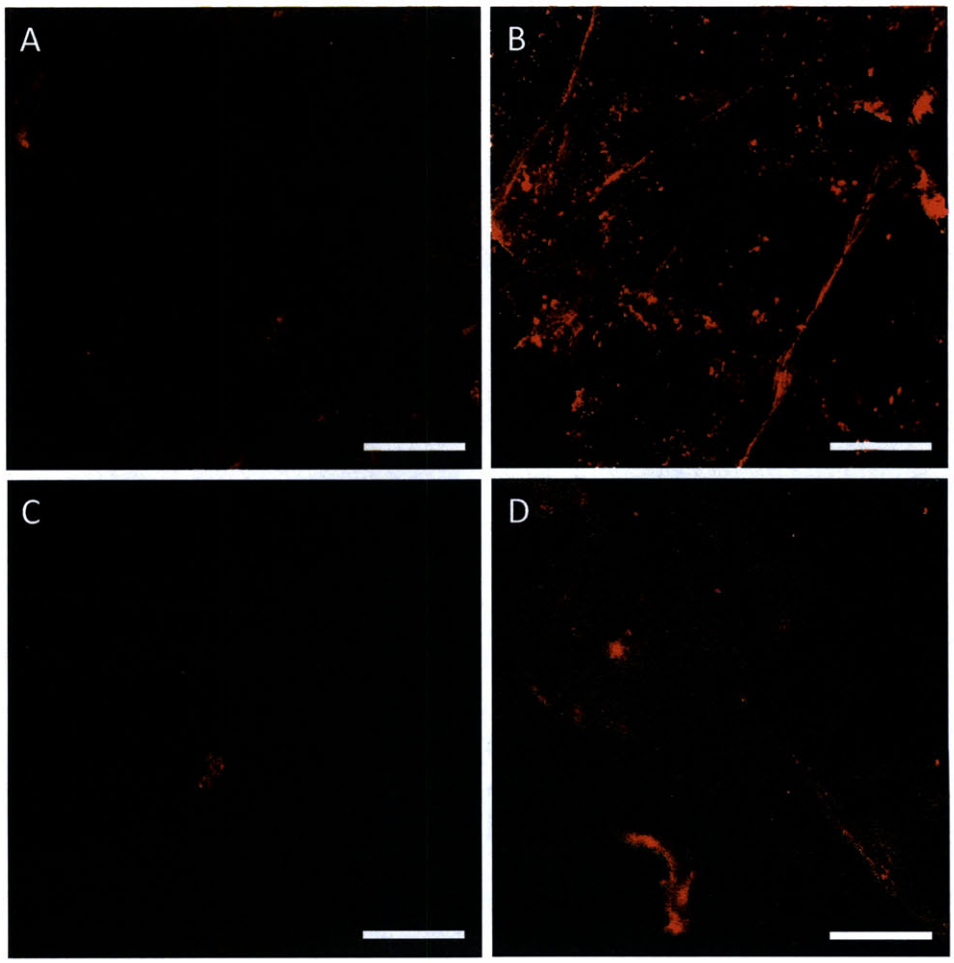

FIGURE 4-2: Confocal images of selected regions of interest in the skin after 24 hours of QD penetration into skin. (A) Surface of the stratum corneum after QD C penetration into untreated skin, (B) Surface of the stratum corneum after QD C penetration in US/SLS-treated skin, (C) Optical section of the isolated dermis, made parallel to the epidermis-dermis surface at a depth of 25 μm below the epidermis-dermis surface, after QD D penetration into untreated skin, and (D) Optical section of the isolated dermis, made to a depth of 25 μm below the epidermis-dermis surface, after QD D penetration into US/SLS-treated skin. Brightness/contrast enhancement was applied to (C) and (D). Bar = 200 μm.

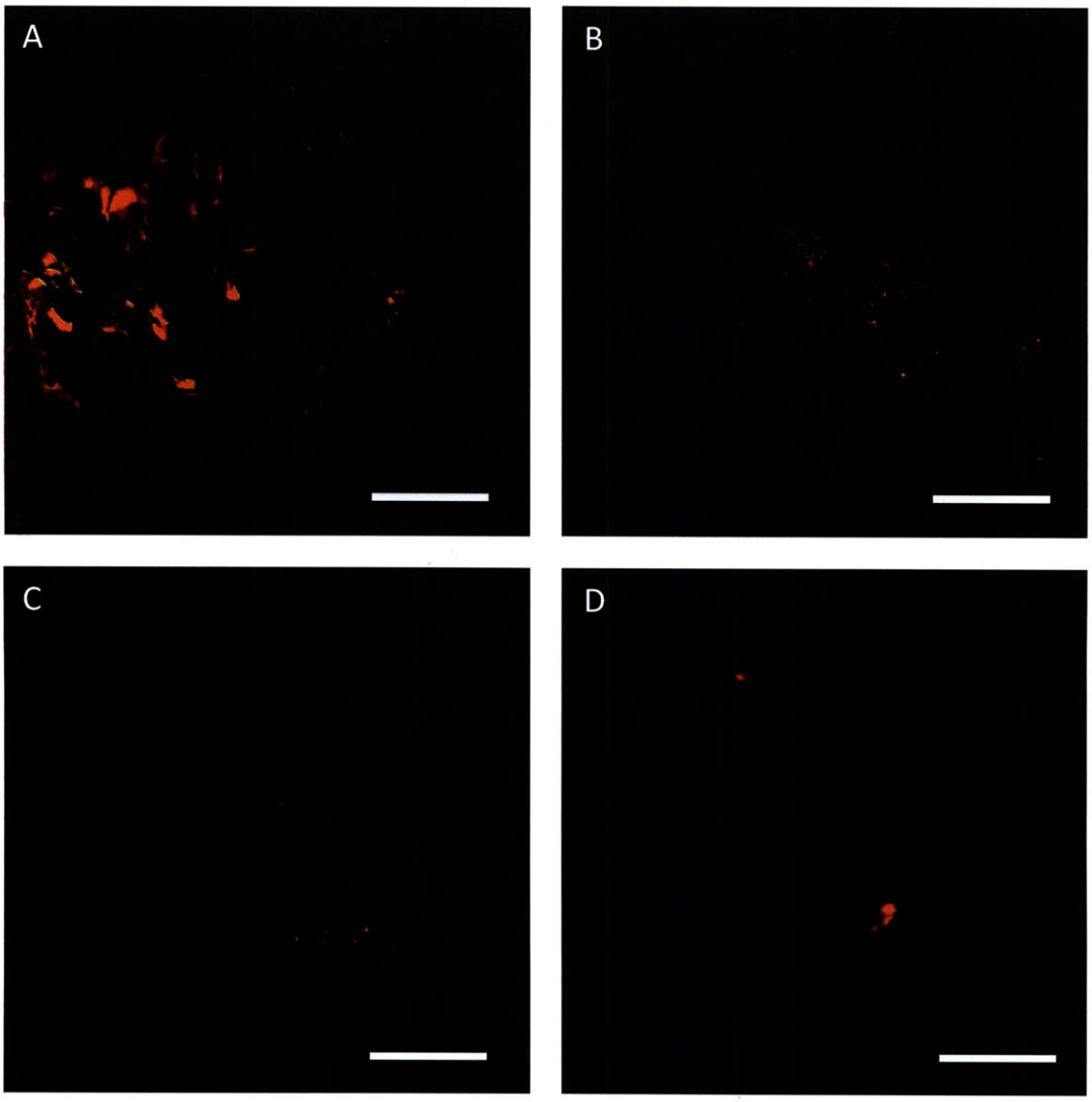

FIGURE 4-3: Selected confocal images of QD transdermal penetration into US/SLS-treated skin. Optical sections of the isolated dermis, made parallel to the epidermis-dermis surface. The depth of each optical section ranges from 6 to 12 μm. Bar = 200 μm. (A) QD A, (B) QD B, (C) QD C, (D) QD D. As can be seen, the distribution of QDs in the skin is heterogeneous.

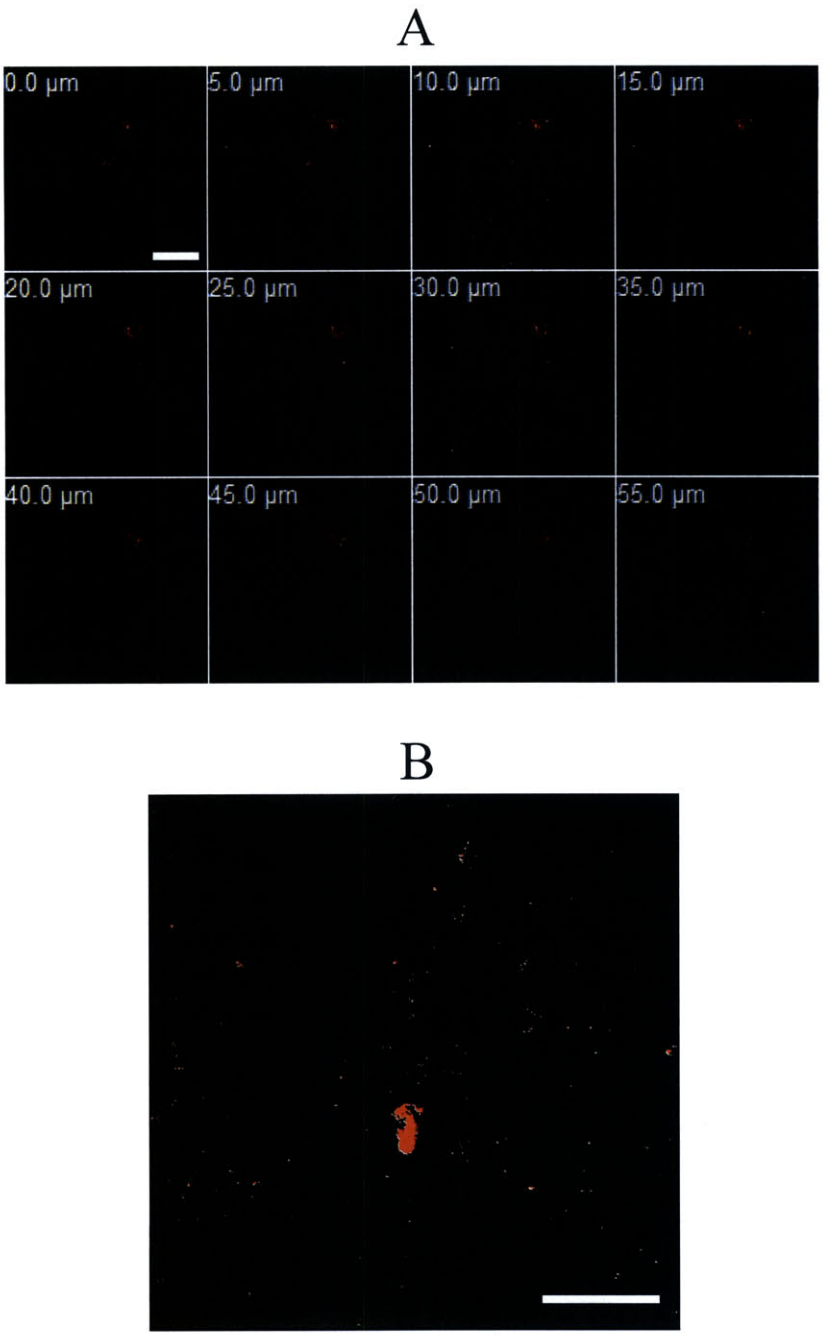

FIGURE 4-4: Confocal images of a selected region of interest in the isolated dermis after 24 hours of QD C permeation across US/SLS-treated skin. (A) Optical sections parallel to the top dermis surface (corresponding to 0.0 µm) to a depth of 55.0 µm below the top dermis surface. (B) Optical section from 30 µm above the bottom dermis surface. Brightness/contrast enhancement was applied to (B). Note that the thickness of the dermis is on the order of 600 µm. Bar = 200 µm.

A

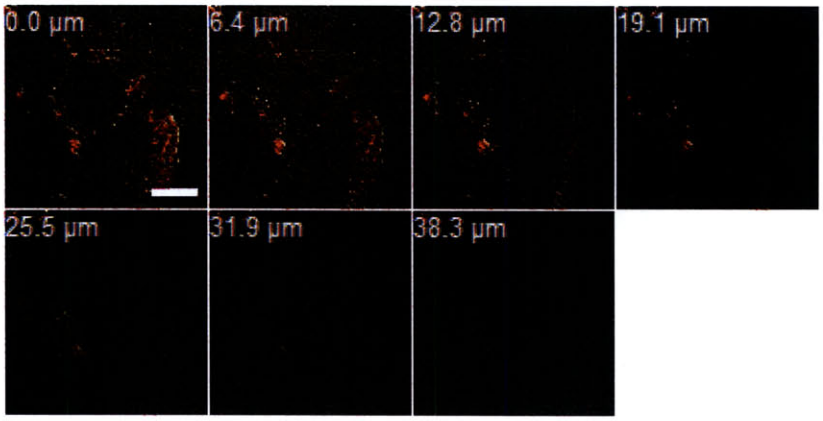

B

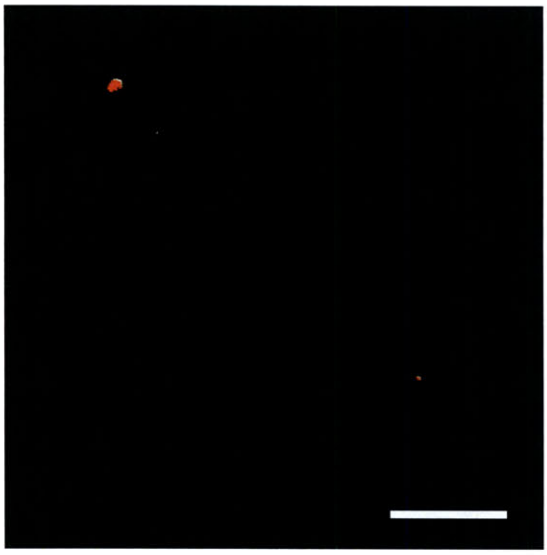

FIGURE 4-5: Confocal images of a selected region of interest in the isolated dermis after 24 hours of QD D penetration into US/SLS-treated skin. (A) Optical sections parallel to the top dermis surface (corresponding to 0.0 µm) to a depth of 38.3 µm below the top dermis surface. (B) Optical section from 30 µm above the bottom dermis surface. Brightness/contrast enhancement was applied to (B). Note that the thickness of the dermis is on the order of 600 µm. Bar = 200 µm.

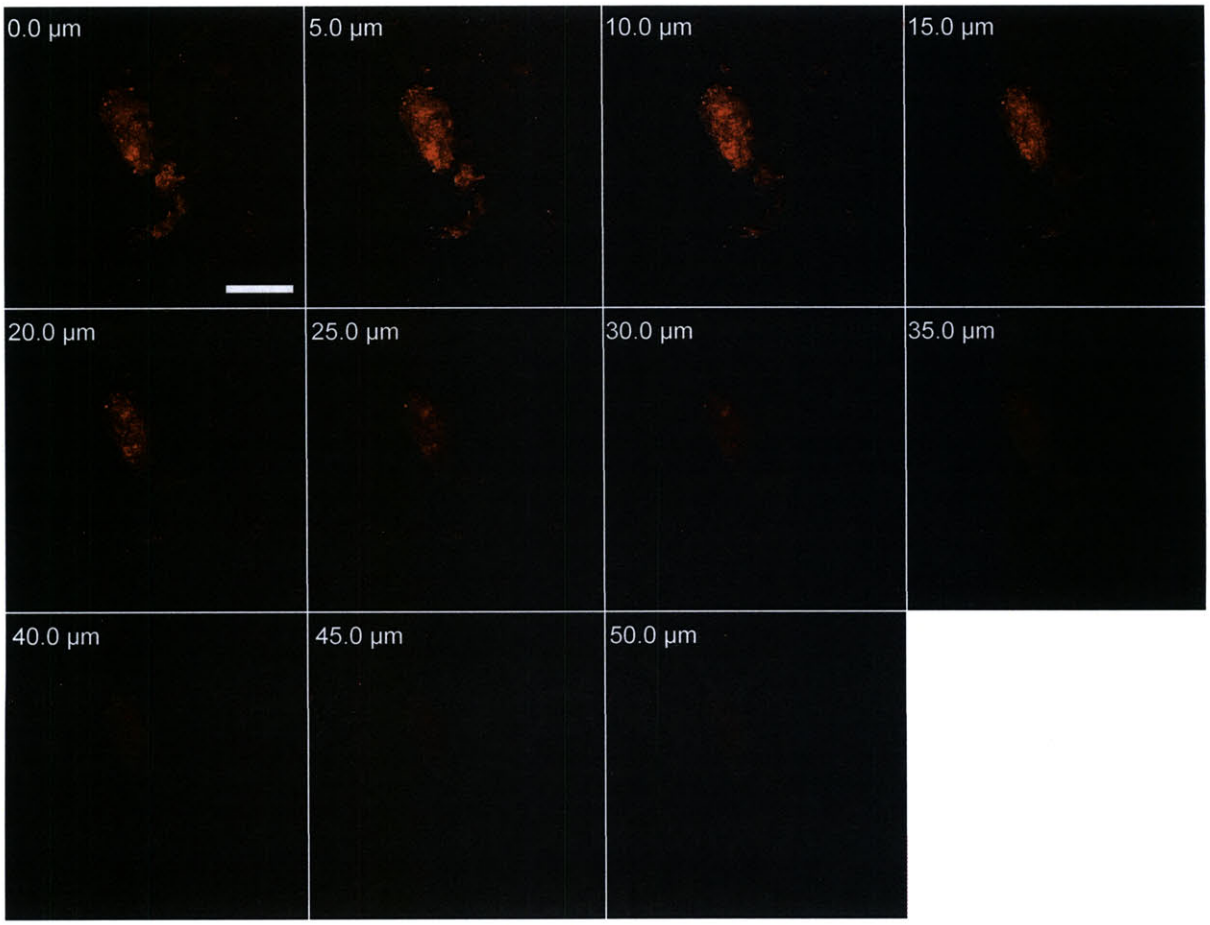

FIGURE 4-6: Confocal images of a selected region of interest in the isolated dermis after 24 hours of QD C penetration into untreated skin. Optical sections from the dermis surface (corresponding to 0.0 µm) to a depth of 50.0 µm below the dermis surface. Brightness/contrast enhancement was applied. Bar = 200 µm.

4.4 DISCUSSION

4.4.1 QD PENETRATION INTO UNTREATED SKIN

The permeation of rigid nanoparticles through untreated skin has previously been investigated (e.g. [84,88-90,92,93]), and conflicting results have been reported. In particular, some research groups claim that observations made using confocal microscopy show no nanoparticle penetration beyond the stratum corneum of pig STS (e.g. [90,92]). Yet, others have used confocal microscopy and qualitatively observed nanoparticle penetration into the dermis of pig STS (e.g. [88,89]). In addition, in previous attempts at quantifying nanoparticle skin penetration, no nanoparticles have been detected in the receiver chamber beneath pig STS using either fluorescence measurements or elemental analysis [88,89]. Furthermore, there have been no previous quantitative reports demonstrating nanoparticle penetration into the dermis of untreated skin.

In the present study, the QDs were not detected to permeate untreated skin to reach the receiver chamber, which is consistent with the previous findings described above. However, the QDs did penetrate the dermis, which was quantified for the first time. Some previous reports have claimed that nanoparticle penetration mainly occurs via hair follicles (e.g. [89,96]). However, QD penetration into the dermis was observed in hair follicles as well as in localized regions outside of hair follicles. To explain this observation, next, possible routes of passive transdermal penetration of nanoparticles are discussed. One commonly proposed route is via aqueous pores located in the head-to-head regions of the stratum corneum's lipid matrix [50,88,89,93]. However, the QDs studied here are much larger than the reported average effective aqueous pore diameter of untreated pig STS (3.3 nm [97]). Therefore, QD penetration into the dermis via aqueous pores is unlikely. A more likely route of QD penetration is via

lacunar regions (imperfections [57]) present in the lipid bilayers of the stratum corneum. The reported mean length of lacunar regions is 183.9 ± 95.03 nm, and the reported mean width is 48.1 ± 12.09 nm [57]. Therefore, the QDs may have permeated across the stratum corneum (the major skin diffusion barrier) through these large lacunar regions. However, the area occupied by these imperfections is small (area density, 0.44 ± 0.11% [57]), leading to the penetration of a very small amount of QDs into the dermis of untreated skin, which was quantifiable by ICP-MS. ICP-MS quantification limits were determined and confocal microscopy was used to visually confirm that the amount of cadmium quantified in the dermis cannot be solely attributed to contamination during sample preparation, to leaching of elemental cadmium from the QDs, or to background cadmium amounts in the skin.

Next, commentary is provided on the conflicting reports in the literature about the ability of nanoparticles to penetrate the dermis of untreated skin. Zhang *et al.* previously stated that the failure to detect nanoparticles in the receiver solution indicates a lack of dermal absorption [89]. However, the combination of quantitative and qualitative results presented in this chapter (in addition to previous qualitative results [88]) clearly shows that such an analysis is insufficient to determine if nanoparticles can penetrate into the dermis. Furthermore, in the previous applications of confocal microscopy to assess nanoparticle skin penetration, mechanical cross-sections of the skin (i.e. sections made perpendicular to the skin surface) were examined by confocal microscopy (e.g. [88-90,92]). However, since nanoparticle penetration was not observed in the majority of the skin (i.e. nanoparticle penetration is heterogeneous), it is anticipated that many cross-sections of the skin will not contain evidence of deep nanoparticle penetration. In this approach, skin is typically prepared in 20-μm-thick sections, which makes it practically impossible to thoroughly inspect the thousands of sections that can be theoretically

produced. Furthermore, since the sectioning knife that creates the cross-sections may inadvertently transfer nanoparticles among the surfaces of the cross-sections, the volume of dermis that can be inspected is reduced, which reduces the probability of observing nanoparticle penetration. All of these reasons explain why this method of sample preparation has yielded inconsistent results. The present study demonstrated that the nanoparticles studied indeed penetrate the dermis in small, localized regions, which was observed after thorough inspection of the intact dermis that was isolated after nanoparticles were applied to the skin. Therefore, the method of inspecting the isolated, intact dermis for nanoparticle penetration is recommended over inspecting mechanical cross-sections of the skin.

Finally, there are additional controversial areas in which the combination of sensitive quantitative and qualitative methods may be applied. First, these methods can be used to address hypotheses based on fluorescence measurements that nanoparticle penetration into human and pig skin may be different, since it was observed that fluorescence measurements alone are insufficient to address this topic (see Appendix, Section 4.7). Second, while QDs were utilized as model nanoparticle drug carriers in this work, the results on the ability of nanoparticles to penetrate into the dermis may also be interpreted in the context of nanoparticle toxicity. The exposure of skin to nanoparticles is currently a controversial and sensitive topic because it would have a significant impact on the regulation of several industries, e.g. waste management, cosmetics, and personal care products [98]. The *in vitro* results in this chapter indicate that upon applying an aqueous QD solution to skin for 24 hours, the QDs have the ability to penetrate into the dermis. However, one must use caution when interpreting these results in the context of nanoparticle toxicity. While the results may be concerning because the dermis is the vascularized layer of the skin that can provide access for systemic absorption [88], it must be noted that the

exposure of skin to an aqueous solution for 24 hours is an extreme condition. In addition, water is a penetration enhancer [99], and therefore, skin hydration may facilitate QD skin penetration. Nevertheless, the application of the quantitative and qualitative methods described in this chapter may be useful to address some of the conflicting reports in the field of nanoparticle skin toxicity.

4.4.2 QD PENETRATION INTO US/SLS-TREATED SKIN

The US/SLS skin treatment promoted the permeation of the QDs across the skin into the receiver chamber in significant amounts, which was quantified using ICP-MS (see TABLE 4-2) and visually confirmed by using confocal microscopy to observe QDs in the bottom layers of the dermis (see FIGURE 4-4B and FIGURE 4-5B). In addition, while the majority of the QDs penetrating past the epidermis remained in the dermis, it is important to recognize that, *in vivo*, systemic transdermal drug delivery does not require permeation across the entire dermis layer [49]. Indeed, once the blood capillaries near the epidermis/dermis junction are reached, the drug can be delivered. The findings suggest that the US/SLS skin treatment represents a viable method to significantly increase the penetration depth and quantity of nanoparticle carriers, thereby enhancing the potential of nanoparticles to serve as useful transdermal drug carriers.

Next, commentary is provided on the extent of transdermal drug delivery enhancement attained with the US/SLS skin treatment. In this study, the amount of QDs penetrating past the epidermis of US/SLS-treated skin ranged from $1/100^{th}$ to $1/1000^{th}$ of the amount in the aqueous topical formulation (250 pmol). It is important to recognize that in this study, QDs served as model nanoparticle drug carriers, and the efficacy of the US/SLS-enhanced transdermal delivery method will depend on various factors that are application-specific, e.g. the US/SLS skin treatment parameters, various physicochemical properties of the carriers (including size, charge,

hydrophilicity, and shape), the loading of the drug carrier, the drug potency, the amount of drug required for therapeutic effect, and the topical formulation. All of these factors must be considered in order to evaluate the viability of a particular US/SLS-enhanced transdermal drug delivery application.

The ability of the QDs to fully permeate US/SLS-treated skin, and the discrete nature of the QD penetration pathways into US/SLS-treated skin, can be explained by several mechanisms: (1) the US/SLS skin treatment increases the area density, length, and connectivity of the lacunar regions within the stratum corneum [57], (2) the US/SLS treatment increases the average effective aqueous pore diameter of pig STS from 3.3 nm [97] to 22.6 nm [100], and (3) the US/SLS treatment enhances skin permeability in a heterogeneous manner. Regarding (3), this phenomenon of heterogeneity in US/SLS-treated skin has been well-documented in pig full-thickness skin (FTS) [28,29]. Specifically, at an US frequency of 20 kHz, the US/SLS treatment creates localized transport regions (LTRs; see Chapter 1, Section 1.4.3) with a reported average effective aqueous pore diameter of greater than 60 nm [29]. The surrounding regions (referred to as non-LTRs) have a reported average effective aqueous pore diameter of 3.7 nm [29]. Note that untreated pig FTS and STS have similar pore diameters [97], and that US/SLS-treated pig FTS and STS have similar pore diameters [100]. Therefore, it is reasonable to assume that the distribution of LTRs and non-LTRs (and their respective pore diameters) within FTS and STS are similar. Next, this assumption is used in order to discuss the results.

First, in ref. [29], US/SLS treatment was applied to pig FTS to attain three skin electrical resistivity values of 0.8, 0.6, and 0.5 $k\Omega\ cm^2$. Skin samples treated to 0.8 $k\Omega\ cm^2$ had an average LTR fractional area of 11%, which varied inversely with skin electrical resistivity [29]. In the present study, skin samples were treated to attain electrical resistivities of $1.25 \pm 0.25\ k\Omega\ cm^2$,

which required less US/SLS treatment than that utilized in ref. [29]. Therefore, one can safely over-estimate the fractional area of LTRs in the present study to be 11%. This implies that the non-LTRs occupied at least 90% of each US/SLS-treated skin sample. Since the non-LTRs occupy the majority of the skin, and since the reported non-LTR average pore size (3.7 nm [29]) is much smaller than the size of the QDs studied here (10 – 20 nm), the finding that QD penetration was not observed in the majority of the skin (corresponding to non-LTRs) is reasonable.

Second, the reported LTR pore size of > 60 nm [29] explains why the QDs were able to penetrate US/SLS-treated skin in localized regions. The observation of the QDs penetrating the dermis (see FIGURE 4-3, FIGURE 4-4, and FIGURE 4-5) provides visual support to the previously proposed hypothesis that LTRs dominate transdermal transport even in the dermis [33]. As suggested previously, the transformation of LTR formation from a heterogeneous to a homogeneous phenomenon has the potential to further enhance the transdermal penetration of macromolecules [28], including nanoparticles.

4.4.3 EFFECT OF SURFACE CHARGE ON QD TRANSDERMAL PENETRATION

It has previously been shown that cationic nanoparticles have an affinity for the negatively-charged skin pores, in contrast to anionic nanoparticles, when they are applied to untreated skin [88,90]. Based on these previous findings, one might expect QD D to penetrate skin in greater amounts compared to QDs A – C. However, it has been quantitatively and qualitatively demonstrated that among the four QDs studied, the QD that exhibited the greatest ability to penetrate both untreated skin and US/SLS-treated skin was not the most cationic QD. This suggests that there is an optimum cationic surface charge for nanoparticle skin penetration.

A nanoparticle that is too cationic may experience hindered diffusion due to strong electrostatic interactions with the negatively-charged skin. Furthermore, the two cationic QDs (C and D) exhibited very different behaviors once they penetrated past the epidermis; out of the four QDs studied, QDs C and D exhibited the smallest and largest fractional retentions in the dermis, respectively. This result was corroborated by FIGURE 4-4 and FIGURE 4-5, which show that QD C more readily penetrated into the deep layers of the dermis compared to QD D. Therefore, surface charge plays a role in the penetration depth of the nanoparticle. In future studies, one may want to optimize the nanoparticle surface charge such that the nanoparticle drug carrier penetrates the skin at sufficient depths and in sufficient quantities. The desired nanoparticle penetration depth will differ for systemic and topical drug delivery applications. For topical applications, perhaps, a drug carrier's surface charge can be tuned to target specific entities found at different depths within the skin.

Finally, QD A penetrated both untreated skin and US/SLS-treated skin in the smallest amounts, in spite of being smaller than the other QDs. Therefore, the findings strongly suggest that the anionic surface charge is the least favorable for nanoparticle skin penetration, which is consistent with previous experimental findings [88,90]. In addition, this result is consistent with the theoretical finding that a charged particle diffusing through a pore of like charge will experience reduced mobility compared to a neutral particle of the same size [101]. Because the skin pores are negatively charged, anionic nanoparticles are expected to permeate the skin in smaller amounts compared to neutral ones.

4.5 CONCLUSIONS

In this study, sensitive, complementary, quantitative and qualitative methods were utilized to evaluate the delivery of nanoparticles into the dermis. These methods will be useful in future assessments of nanoparticle skin penetration. Using ICP-MS, QD penetration into the dermis of untreated skin was quantified for the first time. In addition, confocal microscopy was utilized in a manner that allows for an improved assessment of dermal penetration compared to previously published methods, and QDs were observed to penetrate skin heterogeneously. ICP-MS and confocal microscopy were combined to show that the US/SLS skin treatment can significantly enhance the skin penetration of nanoparticles, thereby enhancing the potential of nanoparticles to serve as transdermal drug carriers. Unexpectedly, the QD that exhibited the greatest skin penetration was not the most cationic QD. In addition, the most cationic QD studied exhibited the lowest clearance from the dermis of US/SLS-treated skin. These findings suggest that an optimum surface charge exists for nanoparticle skin penetration, and motivate the application of nanoparticle carriers to US/SLS-treated skin for enhanced transdermal drug delivery.

In this chapter, it was demonstrated that the proper application of fluorescence techniques can lead to new insights when used in conjunction with a quantitative method. In the next chapter, then, this concept was applied to gain new insights into the mechanisms of chemical penetration enhanced transdermal drug delivery. Chapter 5 describes the first study of fluorescent penetration enhancers (FPEs) and demonstrates the combination of FPEs with fluorescence technologies to directly visualize the behavior of FPEs within skin. New insights obtained using this approach will aid in designing effective penetration enhancers for drug delivery applications.

4.6 Appendix A: Detailed ICP-MS Protocols

4.6.1 Cleaning Protocols

These protocols were used to meticulously clean the glassware, stir bars, and polyfluor alkoxy vials (Savillex, Minnetonka, Minnesota) in order to reduce background amounts of metal that would otherwise interfere with the quantification of trace cadmium amounts from the quantum dots that penetrated into the skin.

4.6.1.1 Glassware

1. Place diffusion cell donor and receiver chambers in a base bath (1M NaOH in 50 vol% ethanol) for 4 hours.
2. Rinse cells with de-ionized (DI) water.
3. Place cells in 1 N HCl (reagent grade) overnight.
4. Rinse cells with DI water.
5. Sonicate cells in DI water for 99 minutes.
6. Rinse cells with DI water. Refill bath sonicator with clean DI water.
7. Sonicate cells again in DI water for 99 minutes.
8. Rinse cells, and let cells sit in DI water overnight.
9. Rinse and dry cells.

4.6.1.2 Stir Bars

1. Place stir bars in a small vial and add 1 N HCl (reagent grade).
2. Sonicate the vial for 99 minutes.

3. Rinse the vial contents with DI water and refill with DI water.
4. Sonicate for 99 minutes.
5. Rinse the vial contents with DI water.
6. Place the vial on a stir-plate and stir vigorously.
7. Rinse the stir bars with DI water.

4.6.1.3 POLYFLUOR ALKOXY (PFA) VIALS FOR ICP-MS

Note: Polyfluor alkoxy (PFA) vials should not be cleaned in the base bath.

1. Perform this step if PFA vials are greasy. Leave vials in aqua regia for 1 day over medium heat. Rinse with DI water.
2. Rinse vials with mega-pure water.
3. Place vials in a large jar for leaching.
4. Fill the jar with 1 N HCl (reagent grade).
5. Cap and invert the jar several times.
6. Triple-bag the jar so that any evaporated acid will not damage the oven.
7. Place the jar in an oven at 60°C for 2 days.
8. Take the jar out of the oven using gloves and place in a hood to cool down for 2 hours.
9. Pour out the HCl from the jar.
10. Rinse the jar with mega-pure water, twice.
11. Remove the vials and rinse vials individually with mega-pure water.
12. Fill the vial bottoms to the brim with 0.1N HCl (ultra grade) and cap with the vial tops.
13. Place the vials into a glass jar.
14. Place the jar in an oven at 60°C for 1 day.

15. Using gloves, turn the jar upside down and leave the jar in the oven for an additional day.
16. Remove the jar from the oven using gloves and let cool.

4.6.2 Digestion Protocols

In these protocols, samples are digested in preparation for trace-metal analysis. All HCl solutions in this procedure should be ultra grade.

4.6.2.1 Digestion of Dermis Samples

1. Discard the 0.1N HCl that is remaining in the 22-mL PFA vials from the cleaning step.
2. Add dermis samples to the PFA vials using a clean pipette tip for each sample. Prepare one control PFA vial for background cadmium amounts (without adding skin to the vial).
3. Withdraw a 1 mL pipette tip and rinse the tip 3x in 1% HCl and 3x in 0.01% HCl to minimize trace metal contamination.
4. If an intermediate container was used to transfer the dermis sample to the PFA vial, add 1 mL 70% HNO_3 to the intermediate container to collect any residual cadmium. Close the intermediate container and shake well. Then, pour the contents into the appropriate PFA vial.
5. Add 70% HNO_3 to each PFA vial to attain a final volume of 3 mL. That is, if 1 mL was used to rinse an intermediate container, add 2 mL. Otherwise, add 3 mL.
6. Cap each PFA vial tightly and swirl. Transport vials to a hood within a clean room.
7. Place PFA vials onto a hotplate heated to 100-110°C for two days. Note that during this step, the samples are being digested.

8. Turn off the hotplate and wait at least 15 minutes for the vials to cool down. Uncap the vials and set the hotplate to 60°C to evaporate the samples to dryness (takes up to 6 hours).

4.6.2.2 Digestion of Receiver Solution Samples

1. Discard the 0.1N HCl that is remaining in the 60-mL PFA vials from the cleaning step.
2. Add dialyzed receiver solution samples to the PFA vials. Transport vials to a hood within a clean room.
3. Place PFA vials (uncapped) onto a hotplate heated to 60°C for 6 hours, or until vial contents are evaporated.
4. Add 5 mL 70% HNO_3 to each vial. Prepare one control PFA vial for background Cd amounts (containing only 5 mL 70% HNO_3). Cap the vials.
5. Place PFA vials onto a hotplate heated to 100-110°C for two days. Note that during this step, the samples are being digested.
6. Turn off the hotplate and wait at least 15 minutes for the vials to cool down. Uncap the vials and set the hotplate to 60°C to evaporate the samples to dryness (takes up to 6 hours).

4.6.3 General Re-Dissolution Protocol

After the samples are digested, the samples are redissolved into a specified volume of dilute acid according to the general protocols described below. In each protocol, the volume of acid was selected to minimize clogging of the ICP-MS equipment by skin particulates and to maximize Cd detection. All HCl solutions in this protocol should be ultra grade. All conical tubes should be

"metal-free" grade. As described below, all samples were spiked with a standard indium salt solution to ensure the accuracy and precision of the ICP-MS method.

- Untreated dermis. Add 5 mL 1% HNO_3 to PFA vials. Heat vials at 60°C for 5 minutes, then swirl the vials to re-dissolve their contents. Then, transfer 1 mL of the vial contents to a 15 mL conical tube containing 4 mL 1% HNO_3. Note that this protocol is equivalent to dissolving the sample in 25 mL of 1% HNO_3. Add 25 μL indium standard to the conical tube to attain a final concentration of 1 ppb. This protocol is described in detail below.

- US/SLS-treated dermis. Add 5 mL 1% HNO_3 to PFA vials. Heat vial at 60°C for 5 minutes, then swirl the vials to re-dissolve their contents. Then, transfer 0.5 mL of the vial contents to a 15 mL conical tube containing 4.5 mL 1% HNO_3. Note that this protocol is equivalent to dissolving the sample in 50 mL of 1% HNO_3. Add 25 μL indium standard to the conical tube to attain a final concentration of 1 ppb.

- All receiver solution samples. Add 10 mL 1% HNO_3 to PFA vial. Heat vial at 60°C for 5 minutes, then swirl the vials to re-dissolve their contents. Then, transfer all of the vial contents to a 15 mL conical tube and add 50 μL indium standard to attain a final concentration of 1 ppb.

Example detailed protocol for re-dissolving untreated dermis:

1. Rinse a pipette tip 3x in 1% HCl and 3x in 0.01% HCl to minimize trace metal contamination.
2. Add 4 mL 1% HNO_3 to all Falcon tubes.
3. Add 5 mL 1% HNO_3 to all PFA vials.
4. Cap PFA vials and shake. Open and check for undissolved residues.
5. Place vials onto a hotplate heated to 60°C for 5 minutes. Swirl the vials and ensure that all solids are dissolved.
6. For each sample, rinse a new pipette tip with the PFA vial contents. Transfer 1 mL of the PFA vial contents to a Falcon tube. Pipette up and down to mix well.
7. Rinse a new pipette tip 3x in 1% HCl and 3x in 0.01% HCl. Add 25 μL indium standard to all tubes to attain a final concentration of 1 ppb.
8. Vortex all tubes.
9. At this point, samples are ready to be injected into the ICP-MS. If necessary, the samples can be filtered to remove skin particulates, which will minimize clogging of the ICP-MS.

4.7 Appendix B: QD Fluorescence Quenching in the Presence of Skin

4.7.1 Materials and Methods

An area of 700 μm-thick pig STS equal to the area available for QD diffusion (1.77 cm^2) was isolated and solubilized using 5 mL of Soluene®-350 (PerkinElmer, Waltham, Massachusetts). This was repeated using 700 μm-thick human STS; human STS was prepared as described in Chapter 3, Section 3.2.2. Then, QD C was added to the following three solutions to attain a QD concentration of 68 nM: (1) Soluene, (2) pig skin in Soluene, and (3) human skin in Soluene. In addition, control skin/Soluene solutions were prepared. A SPEX FluoroMax-3 spectrofluorimeter (HORIBA Jobin Yvon, Edison, New Jersey) was used to excite each sample at 350 nm and to measure the fluorescence intensity at 600 nm (the peak emission wavelength of QD C).

4.7.2 Results and Discussion

The normalized fluorescence intensities of the QD solutions were significantly greater than those of the control solutions (see Figure 4-7). In addition, both pig and human skin were found to quench QD fluorescence, however the emission of the QD/Pig/Soluene solution is significantly greater than that of the QD/Human/Soluene solution ($p < 0.05$). These results indicate that QD fluorescence quenching can be more prominent in human skin than in pig skin. This is likely to be caused by differences between the pig and human skin components [102]. These results are reported because there are arguments in the literature that pig skin is more permeable to nanoparticles than human skin (e.g. [98,103]). These arguments are based on comparisons of nanoparticle fluorescence intensities within pig and human skin. However, the results indicate that fluorescence measurements are insufficient to compare nanoparticle

penetration into pig and human skin. Furthermore, these results explain why smaller nanoparticle fluorescence intensities have been observed within human skin compared to pig skin. A quantitative method such as ICP-MS is suggested to more accurately evaluate whether pig and human skin models are equally permeable to nanoparticles.

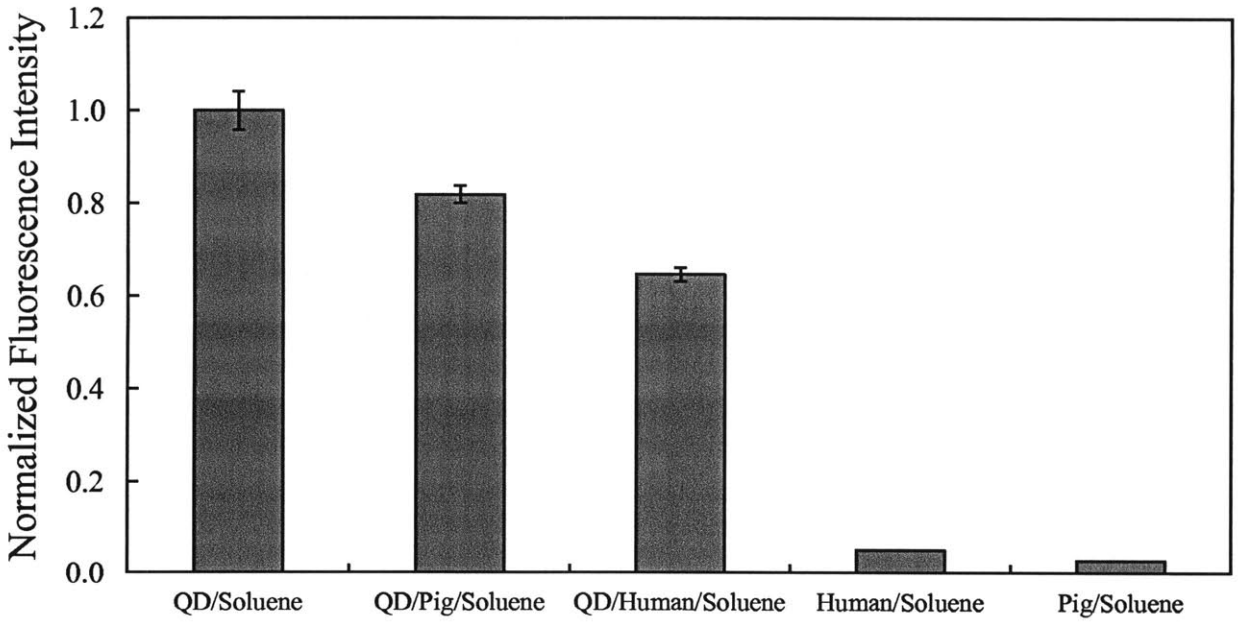

FIGURE 4-7: Fluorescence intensities of QD/Skin/Soluene solutions, normalized with respect to that of the QD/Soluene solution. Data shown are the mean ± SD of two replicates.

CHAPTER 5

FLUORESCENT PENETRATION ENHANCERS FOR TRANSDERMAL APPLICATIONS

5.1 INTRODUCTION

Chemical penetration enhancers (referred to hereafter as penetration enhancers) are molecules that facilitate drug delivery through a biological membrane. These membranes are often composed of lipid assemblies, including the stratum corneum of the skin, epithelial membranes (e.g. corneal, buccal, and intestinal), and cellular membranes. Many molecules have been identified that can enhance drug delivery [14,104-107], particularly amphiphiles, which are molecules that contain polar moieties ("head" groups) and non-polar moieties ("tail" groups). Unfortunately, potent penetration enhancers are often also potent irritants [106]. Several investigations have been carried out to elucidate the molecular mechanisms involved in penetration enhancement and in membrane irritation (primarily regarding transdermal drug delivery [14,106,107], the focus of this thesis). For example, proposed transdermal enhancement mechanisms include extraction or fluidization of lipid bilayers, formation of segregated phases within the bilayers, and others [14]. However, the mechanisms are still not fully understood. Accordingly, the development of new approaches to evaluate the interactions between penetration enhancers and biological membranes would significantly contribute to a better

understanding of the mechanisms involved. In turn, this would aid in designing potent, yet safer, penetration enhancers for drug delivery.

In the life sciences, the generalized problem of studying the behavior of molecules within biological tissues has often made use of fluorescence-based techniques. Using techniques such as fluorescence resonance energy transfer (FRET), time-resolved fluorescence (TRF), fluorescence polarization (FP), fluorescence recovery after photobleaching (FRAP), fluorescence correlation spectroscopy (FCS), fluorescence lifetime imaging microscopy (FLIM), and confocal and multi-photon fluorescence microscopy, one can study structure, function, and interactions of molecules in biological systems [108]. These well-established techniques require that the molecules of interest be either naturally fluorescent or fluorescently-labeled.

To the best of our knowledge, penetration enhancers have never been synthetically modified with a fluorescent label, presumably because it is believed that the relatively large size of fluorescent labels would significantly affect the activity of the enhancers. Therefore, the goal of this work was to identify naturally fluorescent penetration enhancers (FPEs) in order to utilize fluorescence technologies to directly study the behavior of FPEs within the skin for the first time. In this study, 12 FPE candidates with amphiphilic characteristics (see Section 5.2.1) were selected and ranked according to their potency as skin penetration enhancers. Because amphiphiles are known to adsorb at an oil/water interface, and thereby to lower the interfacial tension, oil/water interfacial tension measurements were carried out to assist in analyzing and interpreting the results. In addition, based on the determined ranking, FPE design principles are discussed for future studies.

Subsequently, two-photon fluorescence microscopy (TPM) was used to directly visualize and compare the skin penetration profiles of FPE candidates that ranked high and low as

transdermal FPEs. In addition, TPM was used to demonstrate that new insights can be obtained by directly visualizing the behavior of FPEs within skin. In transdermal applications, penetration enhancers are often part of a multi-component skin treatment or topical formulation that is designed to overcome the skin barrier in a safe and effective manner. FPEs can now be used to visualize the effect of skin treatments on FPE penetration into skin. This chapter presents the first direct visualization of passive, glycerol-mitigated, and ultrasound-assisted FPE penetration into skin. The glycerol and ultrasound (US) treatments are well-established skin treatments that are utilized for decreasing and increasing skin penetration, respectively. Glycerol, a well-known skin moisturizer (humectant), is often used in combination with irritating substances in order to mitigate irritation [109]. On the other hand, low-frequency US is a physical skin penetration enhancer that is often combined with chemical enhancers, resulting in synergism in enhancing transdermal drug delivery [27,30,97]. TPM has previously been used to study the effect of these two skin treatments on penetration enhancers by treating skin either simultaneously or successively with a penetration enhancer and a fluorescent probe in order to *indirectly* visualize the effects of the penetration enhancer on the skin [21,54,110]. Similarly, dual-channel TPM (which allows for the simultaneous imaging of an exogenous fluorescent probe and the intrinsic skin fluorophores [111]) has previously been used to delineate penetration enhancer-induced changes in permeant diffusion with respect to the skin structural features [54,110,111]. These effects can now be *directly* visualized and investigated using FPEs.

5.2 Materials and Methods

5.2.1 Selection of Fluorescent Penetration Enhancer (FPE) Candidates

Many potent penetration enhancers are amphiphiles [14,104-107]. Therefore, 12 molecules that have amphiphilic characteristics were selected as FPE candidates. Fluorescent molecules with various head group chemistries, tail group lengths, and fluorophores were selected as FPE candidates. A list of these 12 molecules is provided in Table 5-1, and the corresponding chemical structures are shown in Figure 5-1. Molecules 1 – 4 were selected because they are fluorescent and exhibit the following additional desirable features which are favorable for penetration enhancers: (i) long, saturated, unbranched hydrocarbon chains (or tail groups) [112], and (ii) low molecular weight (less than 500 Daltons) [113]. Molecule 5 was selected because it is one of a handful of fluorescent dyes that is marketed as an amphiphile; this one was selected because of its relatively low molecular weight among amphiphilic dyes. Molecule 6 was selected because it is fluorescent, has a low molecular weight, and was determined to be surface-active in our preliminary experiments (using the procedure described in Section 5.2.7, molecule 6 lowered the oil/water interfacial tension by 2.8 ± 0.5 mN/m (95% confidence interval)).

Molecules 7 – 12 are all rhodamine derivatives. The selection of these molecules was inspired by recent findings by Polat *et al.* regarding the amphiphilic nature of the fluorescent dye, sulforhodamine B (SRB) [114]. SRB has repeatedly been utilized as a hydrophilic dye. However, SRB is actually an amphiphile, despite being a bulky molecule. SRB was shown to act as a penetration enhancer when combined with a low-frequency US skin treatment (low-frequency US is a physical skin penetration enhancer [27,30]). However, in preliminary passive experiments (without US), SRB was determined to be an insignificant penetration enhancer (as

will be shown in Section 5.3.1). It was hypothesized that without US, SRB is too bulky to penetrate into skin in significant amounts, and that smaller rhodamine derivatives may better penetrate into skin and may be mischaracterized in the literature as hydrophilic instead of amphiphilic (as was the case with SRB). Therefore, several rhodamine derivatives whose molecular weights are smaller than that of SRB were selected as FPE candidates.

5.2.2 Sources of FPE Candidates

Acridine orange 10-nonyl bromide (AO), methyl orange sodium salt (MO), rhodamine 110 chloride (R110), rhodamine B chloride (RB), and SRB sodium salt were obtained from Sigma-Aldrich (St. Louis, Missouri). 5-dodecanoylaminofluorescein (FLUOR), BODIPY® 500/510 C_8, C_5 (BODIPY1), and BODIPY® FL C_{11} (BODIPY2) were obtained from Invitrogen (Carlsbad, California). Rhodamine 6G chloride (R6G) was obtained from Acros Organics (Geel, Belgium). Sulforhodamine G sodium salt (SRG) was obtained from Biotium (Hayward, California). 5-carboxytetramethylrhodamine (TAMRA) was obtained from ChemPep (Wellington, Florida). 2-{3-Cyano-4-[4-(dodecyl-methyl-amino)-phenyl]-5,5-dimethyl-5*H*-furan-2-ylidene}-malononitrile (DCDHF) was a gift, synthesized at Kent State University, Kent, Ohio. MO, RB, and SRG were purified via Büchner funnel vacuum filtration in order to remove water-soluble impurities prior to use (see Section 5.2.4). All the other FPE candidates were used as received.

TABLE 5-1: Name and molecular weight (MW) of each of the 12 FPE candidates. Chemical structures are provided in FIGURE 5-1.

Acronym	Name	MW (Da)	Structure
AO	acridine orange 10-nonyl bromide	473	1
BODIPY1	BODIPY® 500/510 C_8, C_5	404	2
BODIPY2	BODIPY® FL C_{11}	404	3
DCDHF	2-{3-Cyano-4-[4-(dodecyl-methyl-amino)-phenyl]-5,5-dimethyl-5*H*-furan-2-ylidene}-malononitrile	459	4
FLUOR	5-dodecanoylaminofluorescein	530	5
MO	methyl orange, sodium salt	327	6
RB	rhodamine B chloride	479	7
R6G	rhodamine 6G chloride	479	8
R110	rhodamine 110 chloride	367	9
SRB	sulforhodamine B, sodium salt	581	10
SRG	sulforhodamine G, sodium salt	553	11
TAMRA	5-carboxytetramethylrhodamine	430	12

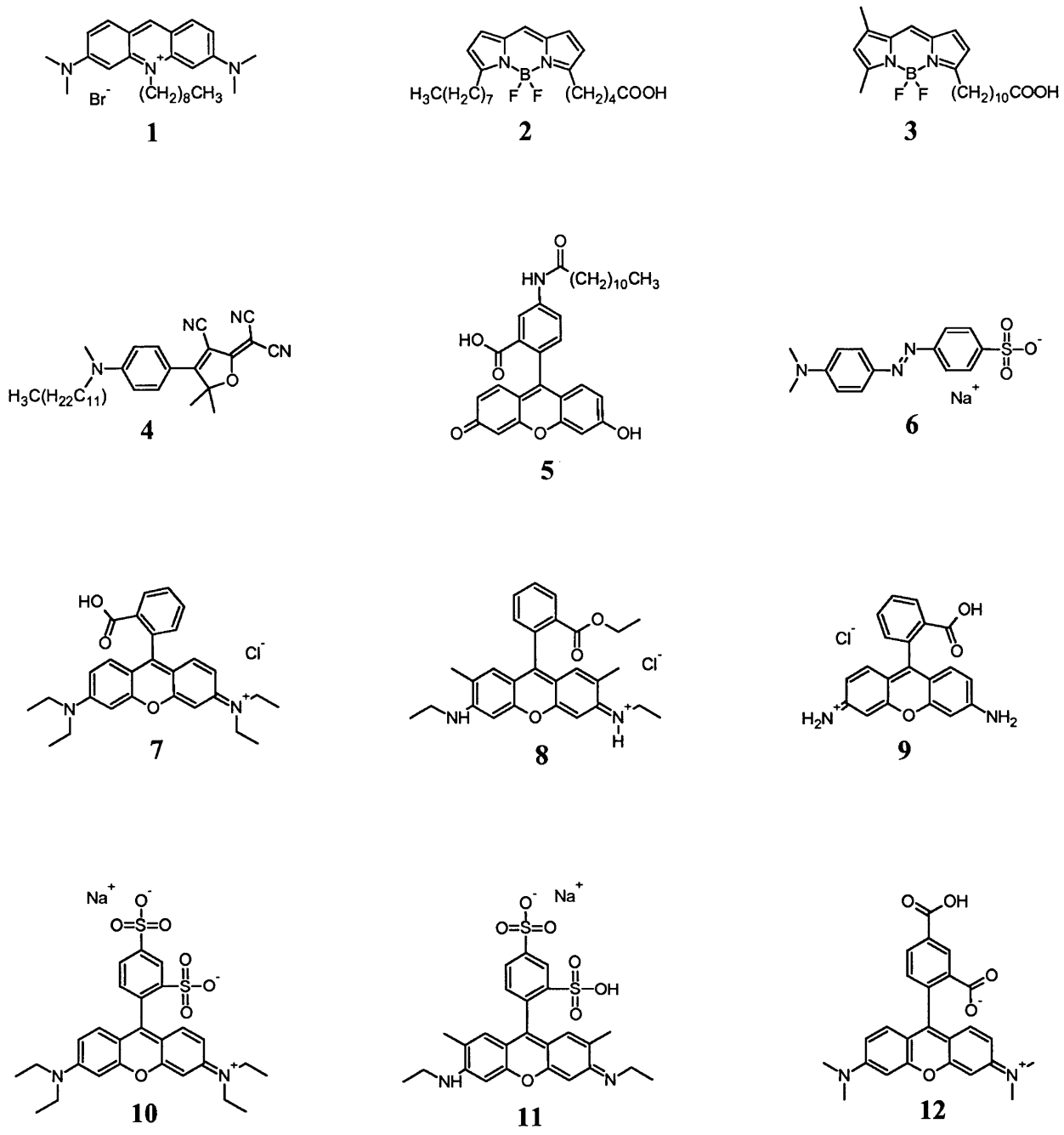

FIGURE 5-1: Chemical structures of the fluorescent penetration enhancer (FPE) candidates.

5.2.3 Sources of General Chemicals

Phosphate buffered saline (PBS) tablets, 1-octanol, and sodium lauryl sulfate (SLS) were obtained from Sigma-Aldrich (St. Louis, Missouri). PBS was prepared from PBS tablets according to the manufacturer's instructions. Glycerol was obtained from Mallinckrodt Baker (Paris, Kentucky). 200 proof ethanol was obtained from EMD Chemicals (Gibbstown, New Jersey). 99+% n-decane was obtained from TCI America (Portland, Oregon). Deionized water dispensed from a Milli-Q academic water purification system (Millipore, Bedford, Massachusetts) was used to prepare all solutions. All general chemicals were used as received.

5.2.4 Purification of MO, RB, and SRG from Water-Soluble Impurities

MO, RB, and SRG were purified by the following procedure in order to separate them from water-soluble impurities. First, these molecules were added to vials containing water, which were subsequently heated to 60°C and then sonicated. After even dispersions were obtained, which usually occurred within 20 minutes, vials were transferred to a salt water/ice bath. Solutions were allowed to recrystallize for 30 minutes. Then, solutions were vacuum-filtered using a Büchner funnel and Grade 1 filter paper (Whatman, Piscataway, New Jersey). Retentates were rinsed several times with water and then dried in an oven overnight at 70°C.

5.2.5 General Protocol for Diffusion Experiments

The following methods have been described in Chapter 3, Sections 3.2.2 and 3.2.3. Briefly, pig skin was obtained from E.M. Parsons & Sons (Hadley, Massachusetts) according to a protocol which was approved by the Committee on Animal Care at MIT. Human cadaver skin was obtained from National Disease Research Interchange (Philadelphia, Pennsylvania). Skin

samples were prepared to a thickness of 700 μm and then mounted into Franz diffusion cells (PermeGear, Hellertown, Pennsylvania) consisting of a donor chamber and a receiver chamber. Any skin sample having an initial electrical resistivity of < 50 kΩ cm^2 (measured with PBS in both chambers) was considered damaged and was discarded.

Subsequently, for all the 24-hour diffusion experiments described below, the PBS solution in the donor chamber was exchanged for 40:60 (by volume) ethanol:PBS (referred to hereafter as 40% ethanol) containing the specified solute concentration. Note that 40% ethanol was used in order to solubilize all the FPE candidates. The donor chamber was sealed using parafilm, and the diffusion cell was covered with aluminum foil to minimize photobleaching. Experiments were conducted at room temperature (25°C).

5.2.6 Evaluating the Potency of the FPE Candidates

The potency of the FPE candidates was quantified by the skin current enhancement ratio (ER), based on previous methods for screening penetration enhancers [106,107,115]. 1 mM FPE candidate solutions were applied to pig skin (for DCDHF, 0.02 mM was used due to low solubility). Initial skin currents were measured 10 – 15 minutes after the start of the experiment in order to obtain stable current measurements [115]. Final skin currents were measured after 24 hours. The ER is defined as the ratio of the final to the initial skin currents. Note that both currents were measured through the 40% ethanol solution present in the donor chamber. 1 mM

SLS (a well-known potent penetration enhancer) was used as the positive control, and 40% ethanol was used as the negative control*.

5.2.7 Oil/Water Interfacial Tension Measurements

The interfacial tension between water and decane, in the presence and absence of solute, was measured based on a previously published method [119]. For each solute, a 2 mM aqueous solution was prepared. Decane was added to attain a volume ratio of 1:1. The interfacial tension was measured at 25 ± 1°C with a Krüss K11 tensiometer and a platinum ring (Hamburg, Germany), using the "interfacial pull" method as described in the instrument manual. The following speeds were used for the various movement steps in the measuring procedure: (i) "measuring", 10 mm/min, (ii) "immersion", 10 mm/min, and (iii) "search", 2 mm/min. Measurements were taken every 20 – 30 seconds until equilibrium was attained, which typically required 1 – 2 hours. The final 10 measurements were averaged for each sample. The lowering of interfacial tension is reported as the absolute difference between the oil/water interfacial tension values in the presence and in the absence of solute. SLS was used as a positive control. Measurements were carried out in triplicate.

* It was observed that the negative control ERs exhibited by pig skin harvested in November and December were significantly greater than those reported in this chapter (which were measured using pig skin harvested in earlier months in the year). This may be explained due to seasonal variation in skin permeability [116-118]. Therefore, only pig skin batches that yielded low negative control ERs were utilized in this study (i.e. skin from November-December were not used), so that the penetration enhancement induced by the 40% ethanol would not mask the enhancement induced by the FPE candidates.

5.2.8 Two-Photon Microscopy (TPM) Case Study Methods

The purpose of these case studies was to use two-photon fluorescence microscopy (TPM) to demonstrate several applications where the direct visualization of FPEs within skin can provide new physical insight. Specifically, the following applications are demonstrated: (I) comparison of the skin penetration profiles of a significant and an insignificant penetration enhancer, (II) visualization of the effect of skin treatments on increasing and decreasing skin penetration, and (III) simultaneous imaging of a FPE and the skin structure.

First, a rationale is provided for selecting which FPE candidate should be used to demonstrate applications I – III. As will be shown in Section 5.3.1, SRB ranked the lowest in potency out of the 12 FPE candidates evaluated. Since the chemical structure of SRB is similar to that of SRG (see Figure 5-1), which exhibited potency similar to that of SLS (see Section 5.3.1), TPM was used to independently substantiate the interesting findings involving SRB and SRG (application I). Subsequently, SRG became a convenient choice to demonstrate glycerol-mitigated and ultrasound-assisted FPE skin penetration (application II) because baseline images of SRG skin penetration were already obtained for application I. Finally, SRG is the most potent FPE whose fluorescence could be filtered from that of the skin for dual-channel TPM imaging (application III).

5.2.8.1 Preparation of Skin Samples for TPM Imaging

For SRB-treated skin (application I), 1 mM SRB was applied to pig skin for 24 hours. For SRG-treated skin (applications I and II), 1 mM SRG was applied to pig skin for 24 hours. For skin treated with SRG and glycerol (application II), the donor solution was prepared as follows: (1) glycerol was added to 40% ethanol to attain 10 wt% glycerol (5 – 15 wt% glycerol is

commonly used in studies on the role of glycerol in cosmetic and pharmaceutical formulations [120]), and (2) SRG was subsequently added to attain 1 mM SRG. For skin treated with SRG and US (application II): ultrasound, with the solid probe tip immersed in a coupling medium containing 1 mM SRG in 40% ethanol, was applied to pig skin with a VCX 130 (Sonics & Materials, Newtown, Connecticut) at the following ultrasound parameters [29]: frequency - 40 kHz, intensity - 7.3 W/cm^2 (for a coupling medium of 40% ethanol, this corresponds to a 40% amplitude setting, as verified using calorimetry), pulsing - 5 seconds on, 5 seconds off, tip displacement - 3 mm, treatment time - 2 minutes ("on" time). The coupling medium was replaced at least every 30 seconds to reduce thermal effects. Note that the duration of the SRG and US treatment was 4 minutes (taking into account the US pulsing), while the duration of all the other skin treatments was 24 hours.

For dual-channel TPM imaging (application III), 2 μg/mL (3.6 μM) SRG was applied to human skin for 24 hours. The dilution of SRG (compared with 1 mM for applications I and II) reduces the SRG fluorescence signal such that it is comparable with that of the skin, which enables the detection of both signals. Note that human skin was used for application III because it is the most commonly used skin model for dual-channel TPM imaging [54,111].

Immediately following the end of each skin treatment, the skin surface was rinsed with 40% ethanol and blotted with a kimwipe to remove excess solute. The treated skin area was isolated using scissors and inserted into an imaging chamber (Coverwell PCI-A-0.5, Grace Bio-Labs, Bend, Oregon) with PBS as the mounting medium. The imaging chamber was sealed with a No. 1.5 glass coverslip.

5.2.8.2 TPM IMAGING

Images were obtained on a Zeiss LSM 510 microscope using a 63x oil objective and a Spectra-Physics Mai Tai laser tuned to 780 nm. TPM imaging was conducted based on previously published methods [54,111,121]. The following settings were used for the three TPM applications: (a) for SRB-, SRG-, and SRG/glycerol-treated pig skin, the laser power was measured at the sample to be 0.4 mW. Emission wavelengths $\leq$ 685 nm were collected. Configurations were set such that in the absence of fluorophores, no signal was detected, (b) for SRG/US-treated pig skin, the laser power was 0.7 mW for imaging 0 – 20 μm below the skin surface and 5 mW for imaging depths > 20 μm. Emission wavelengths in the range of 565 – 615 nm were collected. Configurations were set such that in the absence of SRG, no signal was detected, and (c) for dual-channel imaging of SRG and human skin autofluorescence, the laser power was 34 mW. In the "green" channel, emission wavelengths < 515 nm were collected (corresponding to skin autofluorescence [122]). In the "red" channel, emission wavelengths in the range of 565 – 615 nm were collected (corresponding to SRG fluorescence). Using the stated experimental conditions and microscopy configurations, the skin autofluorescence intensities in the presence and in the absence of SRG were found to be comparable, thus verifying that SRG did not introduce noise in the green channel. Configurations were set such that in the absence of SRG, no signal was detected in the red channel (see FIGURE 5-2).

Up to six 200 μm x 200 μm sites were imaged within each skin sample. Images were obtained in the plane parallel to the skin surface (xy-mode), and optical sections were made in the z-stack mode (e.g. see FIGURE 5-3). In all the figures presented, a red color scheme is utilized to illustrate routes of FPE penetration. It is important to recognize that the images serve to provide *qualitative* information regarding the visualization of FPE penetration patterns.

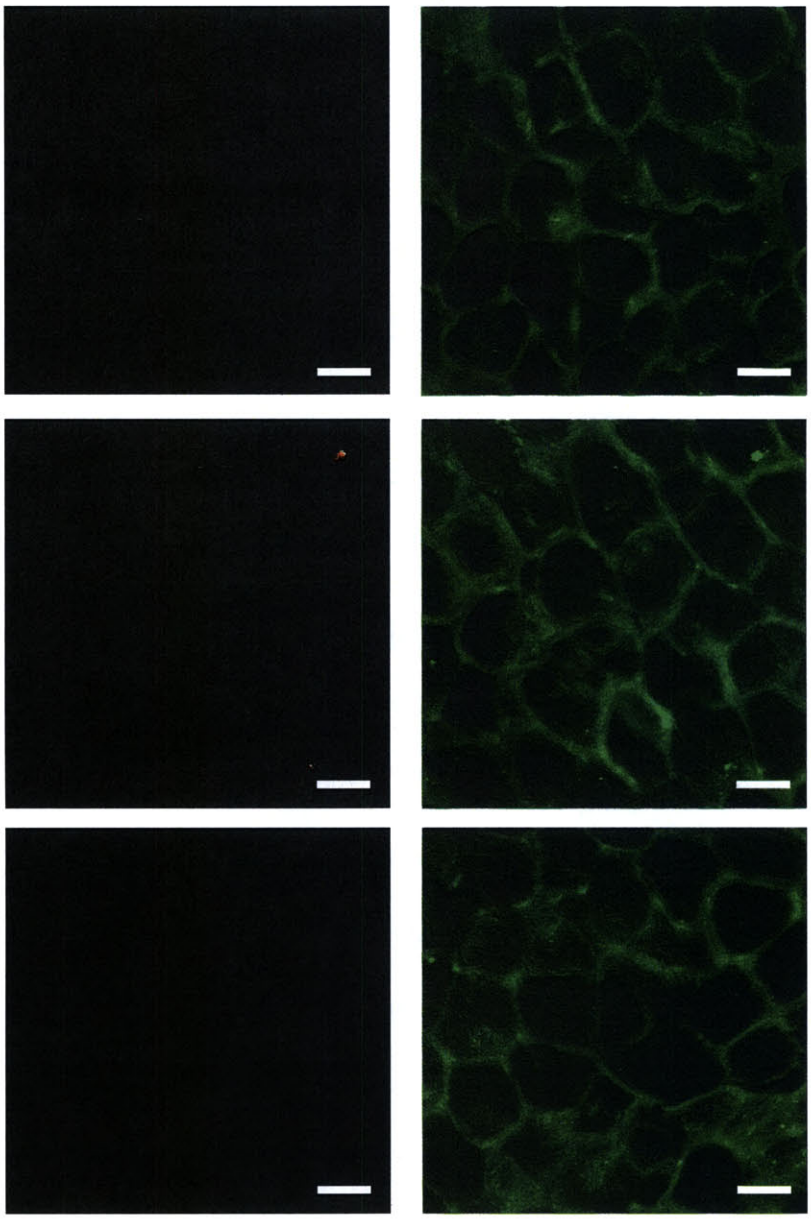

FIGURE 5-2: Representative dual-channel control images of human skin autofluorescence at the skin surface. 40% ethanol (without SRG) was applied to the skin for 24 hours. Left column, SRG channel; right column, skin autofluorescence channel (the presence of skin fluorophores is indicated by the green color). Bar = 20 μm.

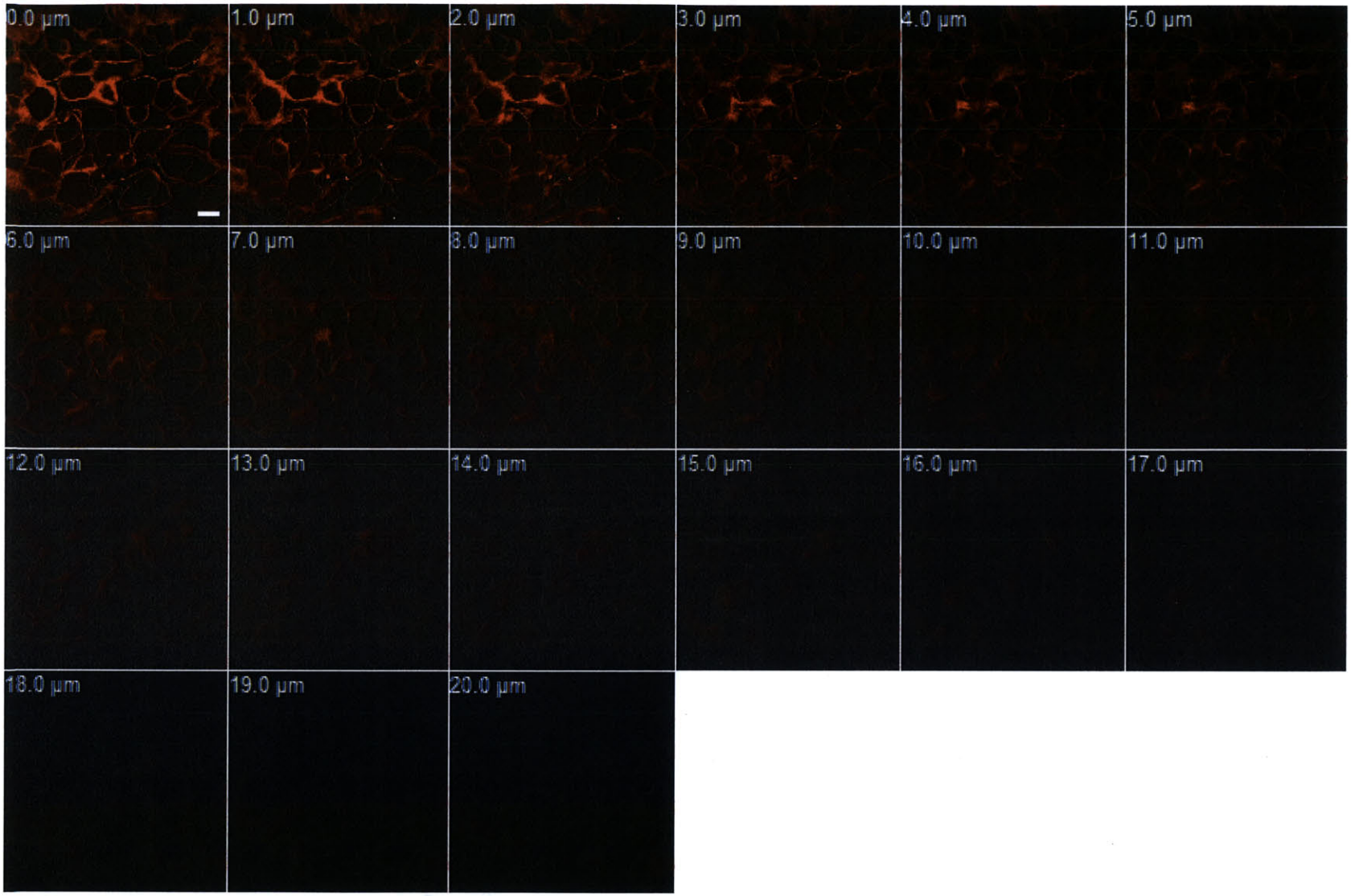

FIGURE 5-3: Representative series of optical sections of SRG penetration into the top 20 µm of pig skin. The presence of SRG is indicated by the red color. Note that the series of images ("z-stack") is scanned at a single site (i.e. the x/y-coordinates are fixed while the z-coordinate increases by 1 µm between scans). The z-stack shows that SRG penetration decreases with skin depth. Bar = 20 µm.

5.2.8.3 IMAGE ANALYSIS

Images were analyzed using ImageJ software (National Institutes of Health, Bethesda, Maryland) [95]. The "Plot Z-axis profile" function was used to calculate the average fluorescence intensity vs. skin penetration depth from each series of images obtained in the z-stack mode (e.g. FIGURE 5-3). These data were averaged over all of the sites imaged for each skin treatment. In addition, for all figures, the brightness and contrast of the images was adjusted first by using the "Auto" feature in order to enhance the visibility of the regions of FPE penetration, and second by increasing the minimum displayed pixel value. These adjustments were propagated to control images to ensure that the control images remained black.

It is very important to recognize that SRB fluoresces more brightly than SRG in non-polar environments (for details, see below)*. Therefore, in order to compare the penetration of SRB and SRG into skin, the SRB fluorescence intensities were normalized by the ratio of the SRB and SRG fluorescence intensities within PBS-saturated octanol (a common chemical model for the skin's lipid bilayers [123], where SRB and SRG localized as shown in FIGURE 5-4).

The normalization constant was calculated after the following experiment was performed in triplicate for SRB and for SRG. 20 μL of the 1 mM donor solution was added to 7 mL of PBS-saturated octanol. After the solution was sonicated, a SPEX FluoroMax-3 spectrofluorimeter (HORIBA Jobin Yvon, Edison, New Jersey) was used to excite the sample at 780 nm, and the resulting emission spectrum (see FIGURE 5-5) was integrated from 450 nm to 685 nm (corresponding to the longest emission wavelength collected during TPM imaging). The mean area under the curve for SRB was divided by the mean area under the curve for SRG, yielding a value of 1.92 ± 0.17 (mean ± SD).

* Interestingly, in aqueous solutions, SRG fluoresces more brightly than SRB (data not shown).

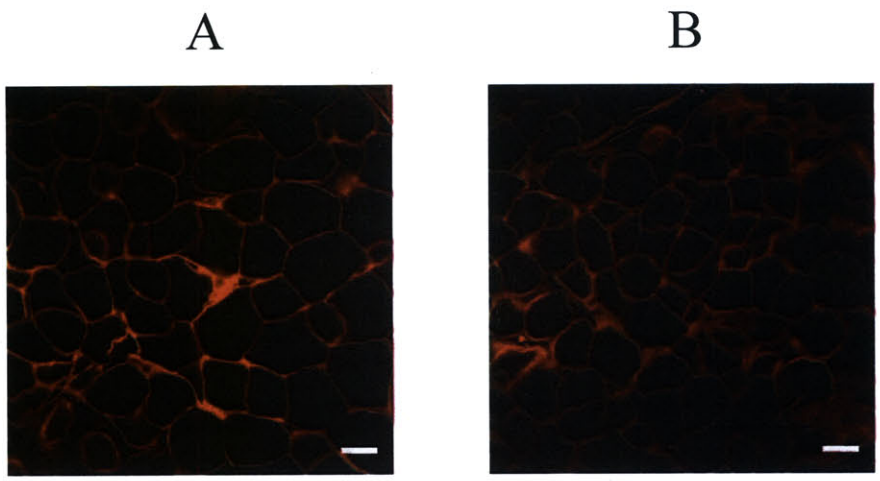

FIGURE 5-4: Intercellular penetration profiles of SRB (A) and of SRG (B). SRB and SRG were applied to pig skin at 1 mM concentration. The presence of SRB and of SRG is indicated by the red color. Image depth, 2 μm below the skin surface. Bar = 20 μm.

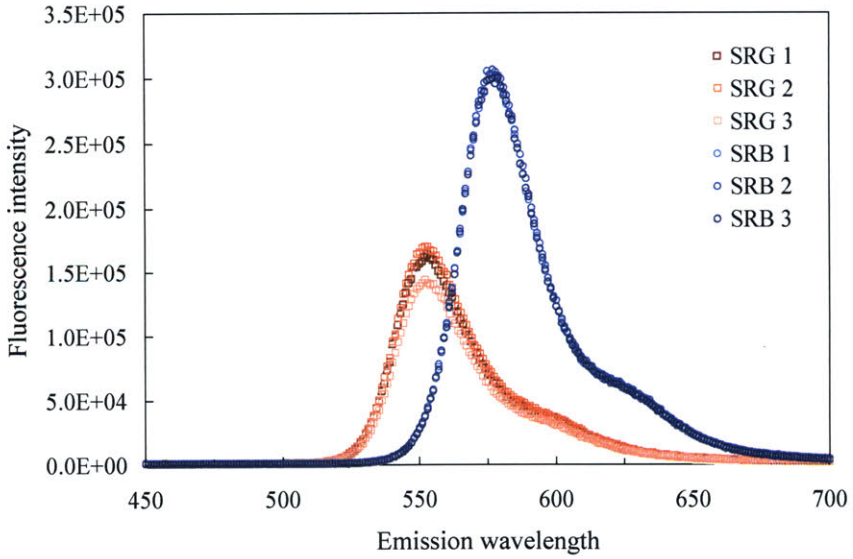

FIGURE 5-5: Emission spectra of SRG and SRB in PBS-saturated octanol. The labels 1 – 3 indicate different samples. Solutions were excited at 780 nm. As can be seen, SRB is nearly twice as bright as SRG in a non-polar environment.

5.2.9 Statistical Analysis

Two-sample, two-tailed *t*-tests assuming unequal variances were used to compare skin current ERs, fluorescence intensities, and oil/water interfacial tension values. In all analyses, *p* values < 0.05 were considered to be statistically significant.

5.3 Results and Discussion

5.3.1 Ranking of the FPE Candidates as Skin Penetration Enhancers

The potency of the FPE candidates as skin penetration enhancers was quantified by the skin current enhancement ratio (ER). Skin electrical current is a sensitive quantitative indicator of skin permeability [58,63]. The results of these experiments are summarized in Figure 5-6. Eight of the twelve FPE candidates (BODIPY1, AO, SRG, RB, R6G, DCDHF, MO, and BODIPY2) exhibited ERs significantly different from that of the negative control; therefore, they are transdermal FPEs. In fact, the best candidates exhibited ERs similar to that of SLS, a well-known potent penetration enhancer (positive control). These results demonstrate that the presence of a fluorescent group in the structure does not prevent molecules from acting as potent penetration enhancers.

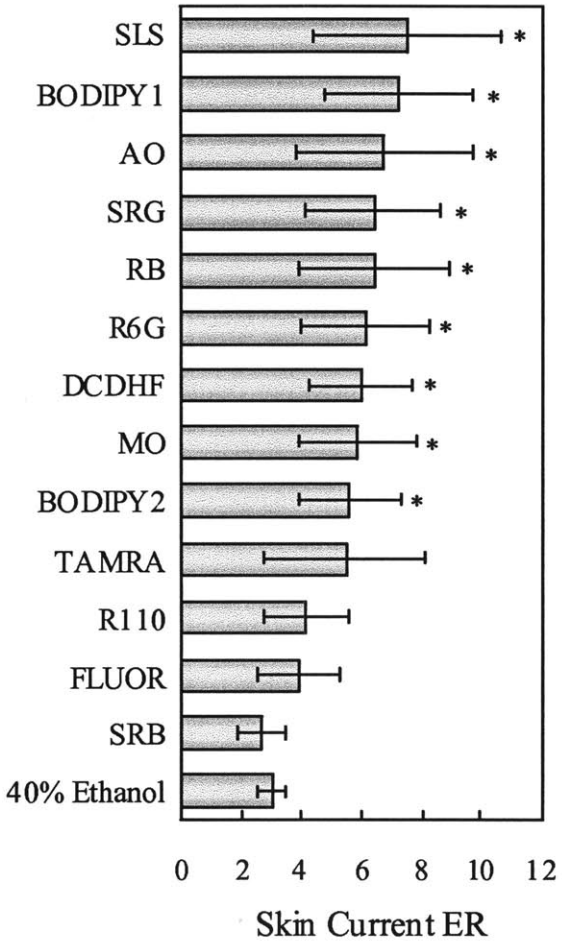

FIGURE 5-6: Skin current enhancement ratios (ERs) exhibited by the FPE candidates considered. SLS served as a positive control. Solute concentrations were 1 mM (except for DCDHF, 0.02 mM). Error bars indicate 95% confidence intervals. * indicates significant difference compared to 40% ethanol (negative control). $n = 40$ for 40% ethanol; $n = 9 - 13$ for all others.

Next, several comments can be made regarding the correlation of the rank of the FPE candidates with their chemical structure. First, the rhodamine candidates (molecules 7 – 12 in TABLE 5-1) are generally bulkier than the candidates with long, saturated carbon chains (molecules 1 – 5 in TABLE 5-1). Based on this comparison, one would intuitively expect the candidates with long carbon chains to better penetrate into skin and perturb the skin lipid bilayers. Nevertheless, the ERs of these candidates and of the rhodamine candidates are evenly interspersed between the ERs of the positive and negative controls. In fact, some candidates from both groups exhibited ERs close to that of the positive control. These results are in agreement with previous findings. First, recall that many drugs that are successfully administered via a transdermal patch are hormones with multiple rings [44], similar to the rhodamine candidates. Second, Mitragotri and co-workers previously designed over 300 mutated chemical skin penetration enhancers based on potency and safety [106]. Their 6 best compounds were ones with either long, saturated carbon chains or with multiple rings.

Second, it is reasonable that BODIPY1 exhibited a greater ER than BODIPY2. While both molecules have long hydrocarbon chains, the fluorophore in BODIPY1 is positioned in the middle of the chain, and the fluorophore in BODIPY2 is positioned at the end of the chain. Penetration enhancers with long hydrocarbon chains can readily intercalate into the structured lipid bilayers of the stratum corneum and disrupt the lipid packing, thereby increasing lipid fluidity and reducing the skin diffusion barrier [124]. However, it is hypothesized that the location of the fluorophore at the end of the hydrocarbon chain (as in BODIPY2) would hinder the chain from intercalating into lipid bilayers. It has previously been shown that the depth of penetration into a lipid membrane depends on the steric bulk of the intercalant [125]. Since BODIPY1 is a better penetration enhancer than BODIPY2, this result suggests that the ideal

location for the fluorophore is adjacent to the head group. It would be interesting to evaluate such a molecule, which is speculated to result in a more potent FPE. Note that BODIPY is a popular fluorophore because its robust fluorescence properties are highly favorable for many imaging applications [126]. Therefore, a modified BODIPY-based FPE has the potential to be utilized in many types of imaging studies.

Third, it is interesting that DCDHF, while applied to skin at $1/50^{th}$ of the concentration of the other candidates, still exhibited a significantly large ER. This indicates that this structure has great potential as a FPE. There are three distinguishing features of DCDHF that may contribute to its significant penetration enhancer activity: (i) nitrile head groups, which have been linked with skin irritation and toxicity [127] (and these properties are often exhibited by potent penetration enhancers [106]), (ii) a 12-carbon tail, which has previously been shown to be the optimal tail length for skin penetration enhancers [112], and (iii) a compact fluorophore with a small number of rings, located adjacent to the nitrile head groups. However, in spite of the fact that DCDHF exhibited potency at a low concentration, it is limited by its poor water solubility. This structure, which has been shown to be readily derivatized [128,129], may be improved by adding a water-soluble group such as sulfonic acid (e.g. fluorophore 21 in [129], shown in FIGURE 5-7).

Fourth, in spite of the fact that SRG and SRB have similar chemical structures, SRG is a significant FPE, while SRB is not. In Section 5.3.2.2, TPM was utilized to visualize the skin penetration profiles of SRG and SRB in order to independently substantiate these interesting results with data from image analyses. As discussed in Section 5.2.1, SRG was selected as a FPE candidate because it is smaller than SRB. However, FIGURE 5-8 shows that over the range of molecular weights studied (327 – 581 Daltons), there is no correlation between molecular weight

and potency as a transdermal FPE. Subsequently, SRG was hypothesized to be more amphiphilic than SRB. A basic feature of amphiphiles is that they can reduce surface or interfacial tensions. Therefore, to compare the amphiphilicity of SRG and SRB, their reduction of the interfacial tension between oil (decane) and water was measured. FIGURE 5-9 shows that SRG is significantly more effective than SRB at lowering the oil/water interfacial tension. This indicates that SRG is indeed more amphiphilic than SRB. One difference in their chemical structures is that the 3-ring xanthene structure of SRB has a delocalized charge of +1 due to resonance; the xanthene structure of SRG is not necessarily protonated. Therefore, the structure of SRG allows for a better distribution of charges and a clearer distinction between head and tail regions. In addition, the +1 charge of the xanthene structure of SRB may result in different interactions with the negatively-charged skin, or may result in intramolecular interactions with the sulfonate-containing pendant group. It would be interesting to investigate the structure-activity differences (i.e. the relationship between the chemical structure and the penetration enhancer activity [123,130,131]) between SRG and SRB in future studies.

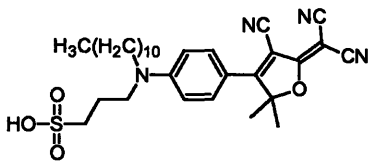

FIGURE 5-7: DCDHF functionalized with sulfonic acid to impart water solubility (molecule 21 in [129]).

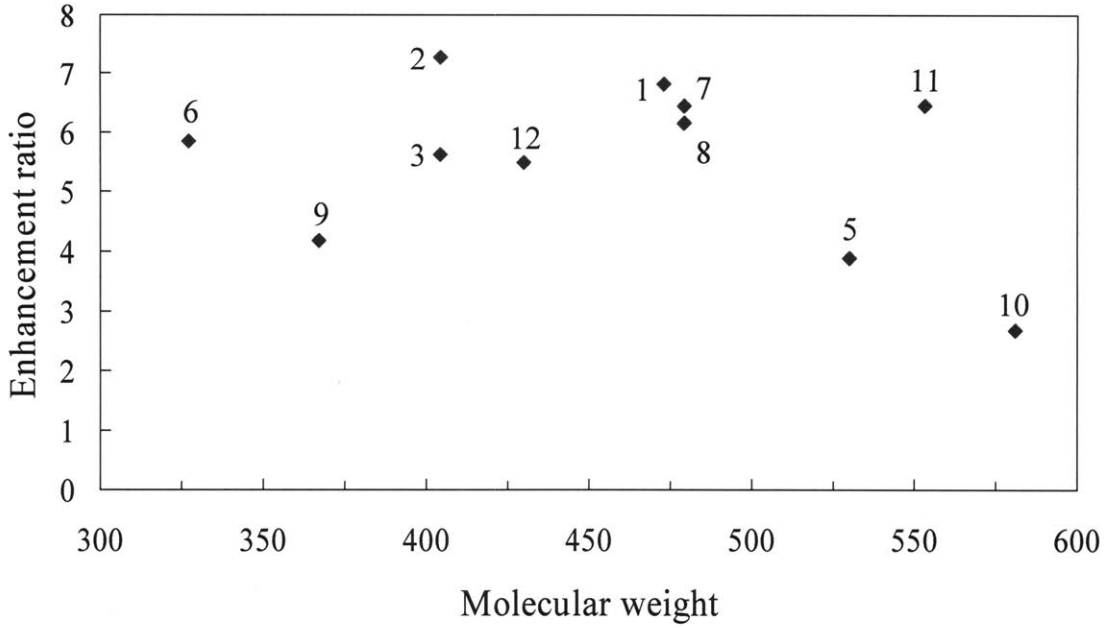

FIGURE 5-8: Skin current enhancement ratio vs. molecular weight of the FPE candidates considered. The numbers adjacent to the blue diamonds correspond to the various FPEs listed in TABLE 5-1. Note that DCDHF is excluded from this figure because the skin treatment conditions differed from that of the other candidates.

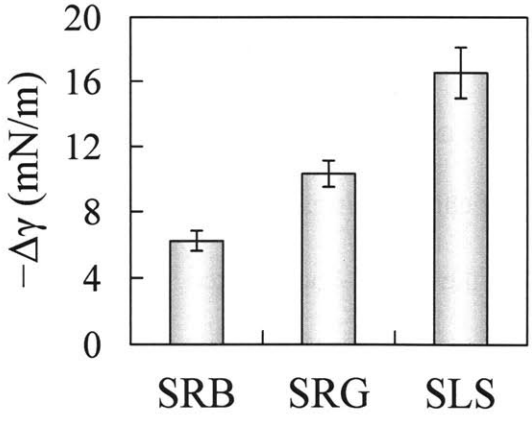

FIGURE 5-9: Lowering of oil/water interfacial tension ($\Delta\gamma$). SLS served as a positive control. Error bars indicate 95% confidence intervals. $n = 3$.

5.3.2 TPM CASE STUDIES: VISUALIZATION OF FPE PENETRATION INTO SKIN

In the previous section, several FPE candidates were demonstrated to be skin penetration enhancers. These FPEs now enable the use of a multitude of fluorescence techniques to investigate FPE-enhanced transdermal applications. As an example, two-photon fluorescence microscopy (TPM) was used to demonstrate several applications where the *direct* visualization of FPEs can provide new physical insight.

5.3.2.1 VISUALIZATION OF THE EFFECT OF SKIN TREATMENTS ON SRG PENETRATION

Representative TPM images of SRG-, SRG/glycerol-, and SRG/US-treated skin samples are shown in FIGURE 5-10. Recall that glycerol and US treatments are well-established skin treatments that are utilized for decreasing and increasing skin penetration, respectively. First, the effect of glycerol on SRG penetration into skin is discussed. In SRG-treated skin, the SRG remained localized within the lipid bilayers surrounding the corneocytes (see FIGURE 5-10A); this localization was observed uniformly throughout the skin sample. With the addition of glycerol, the SRG penetration pattern remained the same (see FIGURE 5-10B), however, SRG fluorescence intensities were smaller. The images were analyzed to determine the average SRG intensity profiles in the presence and in the absence of glycerol. These data, presented in FIGURE 5-11, show that glycerol significantly mitigated the penetration of SRG into skin (by 20%), which is consistent with the well-documented anti-irritant properties of glycerol [109,110,120,132]. Note that it was verified that glycerol does not directly affect the fluorescence intensity of SRG (i.e. the SRG donor solution fluorescence intensities with and without 10% glycerol were the same; data not shown).

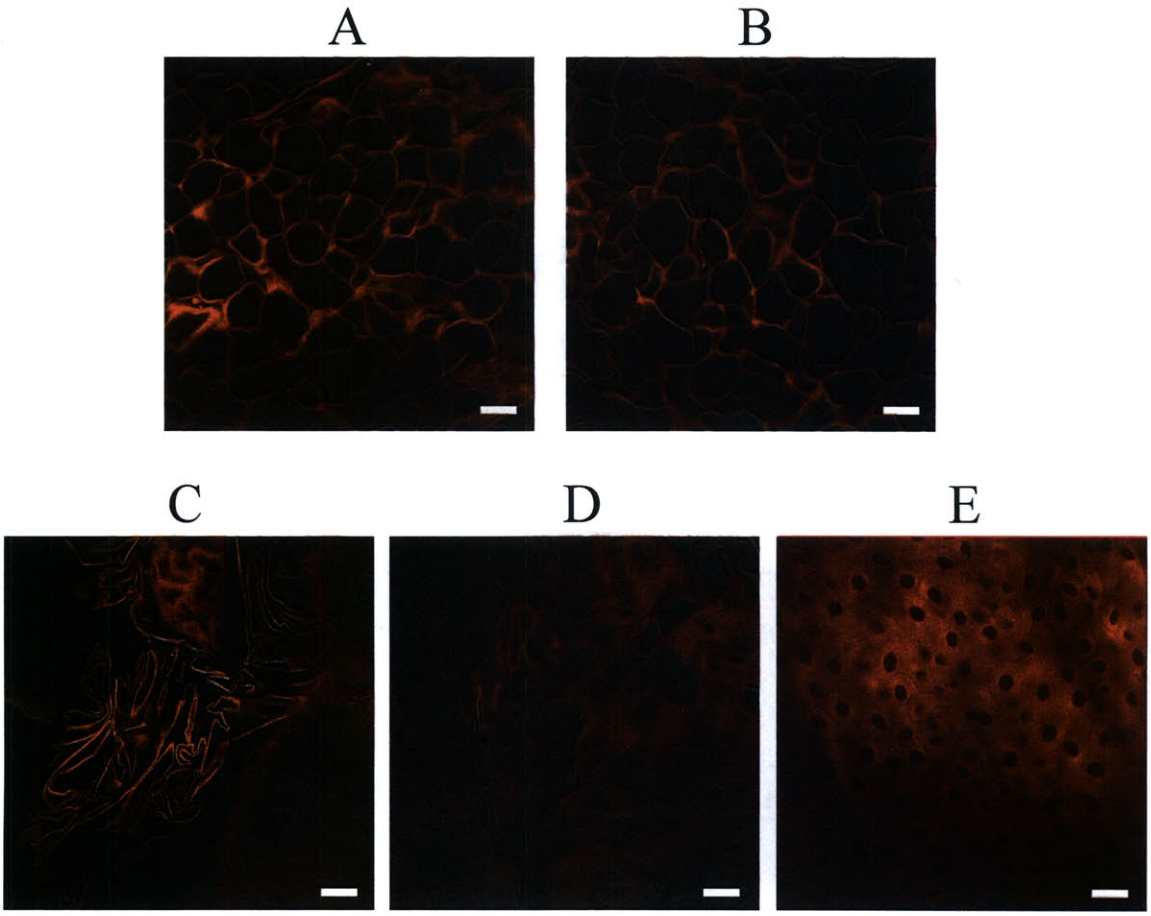

FIGURE 5-10: SRG penetration patterns within SRG-treated, SRG/glycerol-treated, and SRG/US-treated pig skin. The presence of SRG is indicated by the red color. (A) Representative image of SRG-treated skin (image depth, 2 μm below the skin surface). (B) Representative image of SRG/glycerol-treated skin (depth, 2 μm). (C, D) Selected regions of interest within the stratum corneum of SRG/US-treated skin (depth, 2 μm). (E) Selected region of interest within the epidermis of SRG/US-treated skin (depth, 34 μm). Bar = 20 μm.

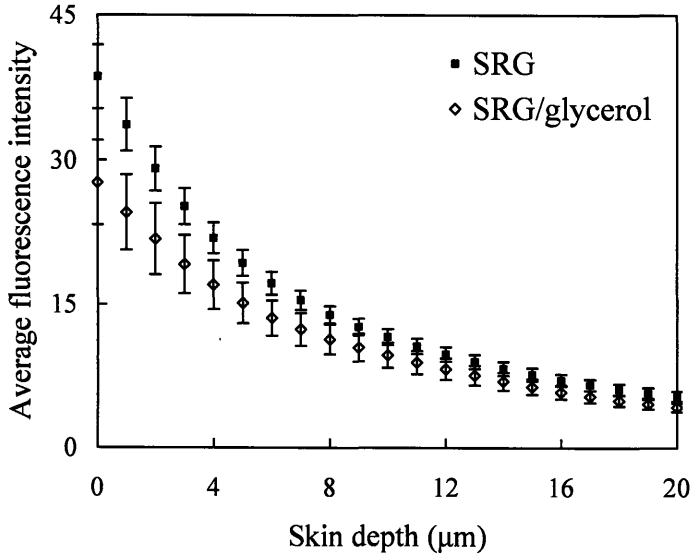

FIGURE 5-11: Average SRG fluorescence intensity as a function of skin depth, in the presence and in the absence of 10% glycerol. Fluorescence intensities are significantly different at all skin depths. Error bars indicate 95% confidence intervals. n = 18 sites for SRG; n = 12 sites for SRG/glycerol.

Next, the effect of US on SRG penetration into skin is discussed. US significantly affects the SRG penetration pattern. FIGURE 5-10C and FIGURE 5-10D show that US assists the penetration of SRG into skin via irregular, transcellular pathways. In fact, no patterns resembling intercellular routes (as seen in FIGURE 5-10A) were observed in SRG/US-treated skin, which suggests that transcellular pathways are dominant in US-treated skin. Furthermore, SRG penetration was only observed in discrete regions that were heterogeneously distributed across the treated skin area, corresponding to localized transport regions (LTRs) that have been well documented within US-treated skin [27,30] (see Chapter 1, Section 1.4.3). LTRs are regions where US-induced cavitation microjets drive SRG into the skin [133]. Finally, with the

assistance of US, SRG penetrated into the epidermis in localized regions in significant amounts (see FIGURE 5-10E), whereas without US, SRG did not significantly penetrate into the epidermis (not shown). Note that in FIGURE 5-10E, the 5-μm circular regions where SRG did not penetrate correspond to the epidermal cell nuclei.

This TPM application demonstrates that by using a FPE, one can directly visualize how changes to a topical formulation or skin treatment affect the penetration and spatial distribution of the FPE within skin. FPEs can now be utilized to aid in designing safe and effective skin treatments and topical formulations, which often contain penetration enhancers.

5.3.2.2 VISUAL COMPARISON OF THE PENETRATION PROFILES OF SRG AND SRB

SRB- and SRG-treated skin samples were imaged using TPM. In both cases, the fluorescence remained localized within the lipid bilayers surrounding the corneocytes (see FIGURE 5-4). The images were analyzed to determine the average SRB and SRG intensity profiles. FIGURE 5-12 shows that SRB did not penetrate as readily into the skin as SRG, which is consistent with the finding that SRG is a significant FPE while SRB is not (see Section 5.3.1). With higher resolution fluorescence techniques (such as single-molecule fluorescence techniques [108]), one may be able to elucidate the differences in mechanisms of skin penetration for significant and insignificant penetration enhancers, which would aid in designing potent, yet safe, penetration enhancers for drug delivery.

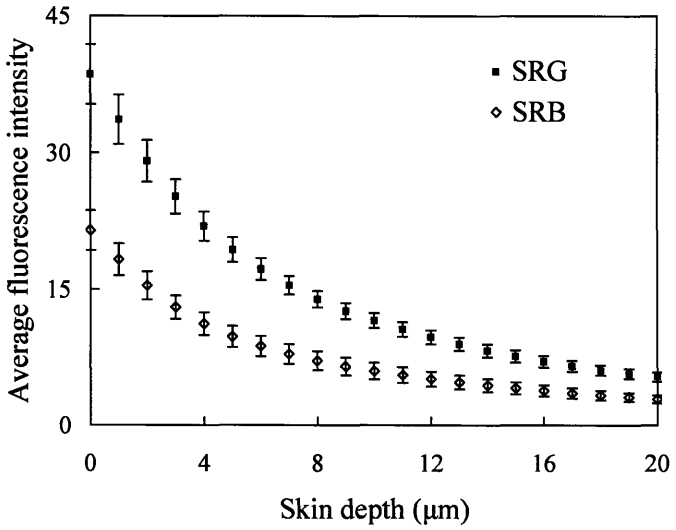

FIGURE 5-12: Average SRG and SRB fluorescence intensity as a function of skin depth. Fluorescence intensities are significantly different at all skin depths. Error bars indicate 95% confidence intervals. n = 18 sites for both SRG and SRB. SRB data were normalized as described in Section 5.2.8.3.

5.3.2.3 DUAL-CHANNEL IMAGING OF SRG AND SKIN AUTOFLUORESCENCE

Skin autofluorescence stems from intrinsic skin components, including collagen, elastin, aromatic amino acids, and cofactors [134]. These components reside in the lipid bilayers; by imaging skin autofluorescence, one can delineate the corneocyte-lipid bilayer interface. Therefore, by simultaneously imaging the probe spatial distribution and the skin autofluorescence, one can identify changes in probe partitioning between the corneocytes and the lipid bilayers and/or probe-induced structural changes in the skin structure [111,134].

This is demonstrated using dual-channel TPM to image SRG-treated skin (see FIGURE 5-13). In the green channel, the skin autofluorescence is generally limited to the intercellular regions surrounding the corneocytes, thereby delineating the skin structure. The corneocyte dimensions are approximately 20 μm, which is consistent with previous reports [7]. In the red channel, it is clear that SRG is not always present throughout the entire intercellular space; instead, there is an apparent preferential localization within a 1-μm thick region at the corneocyte-lipid interface (see arrows in FIGURE 5-13). This region may include the 15-nm cornified cell envelope, which is composed of a mixture of cross-linked protein filaments and lipid molecules [7]. This localization suggests that SRG is amphiphilic, which was evaluated in Section 5.3.1. Other higher resolution fluorescence techniques (such as single-molecule fluorescence techniques [108]) can be used to investigate this localization further, which may contribute new physical insights on the *interactions* between FPEs and the skin.

Note that in FIGURE 5-4 and FIGURE 5-10, SRG was applied to the skin at 1 mM concentration, while in FIGURE 5-13, SRG was applied at 3.6 μM concentration. In FIGURE 5-4 and FIGURE 5-10, SRG is present throughout the lipid bilayers likely because the corneocyte-lipid interfacial regions are saturated.

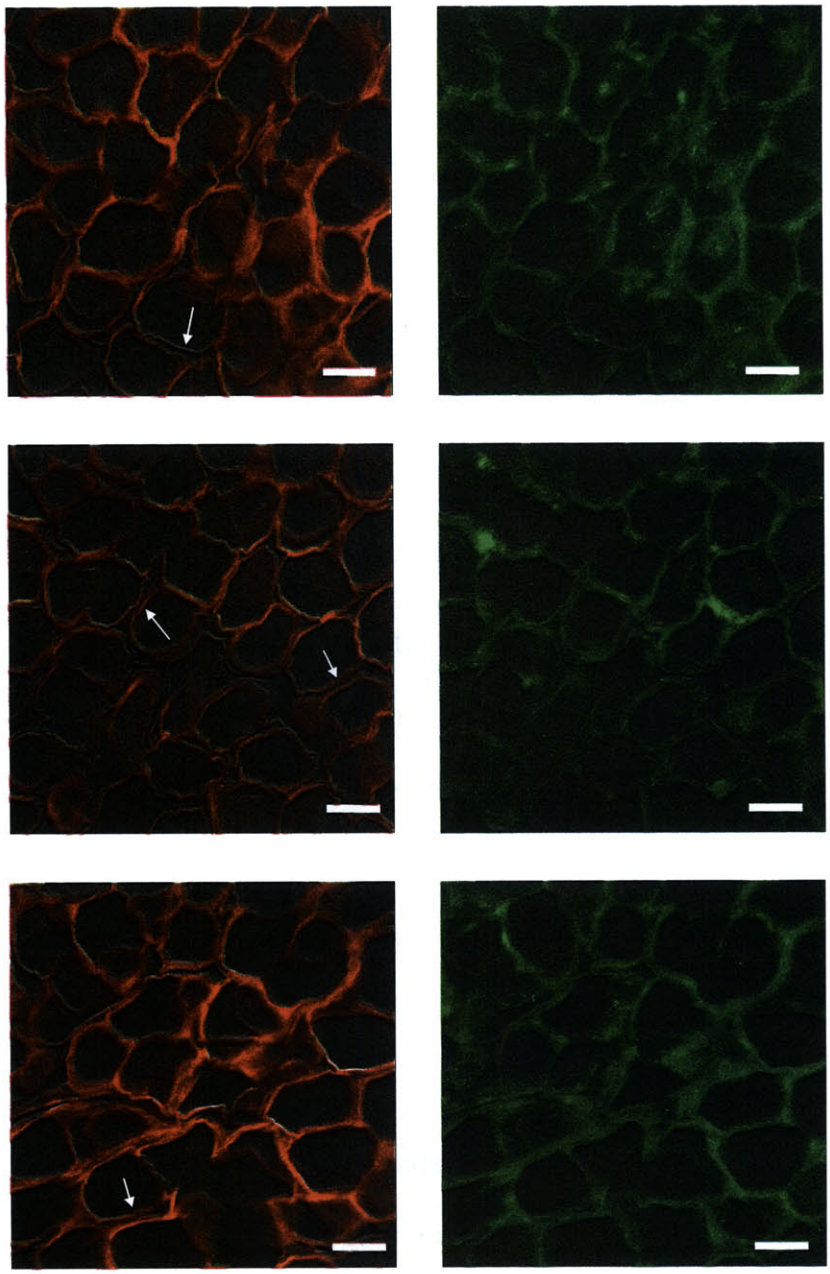

FIGURE 5-13: Representative dual-channel images of SRG and human skin autofluorescence at the skin surface. Left column, SRG channel (the presence of SRG is indicated by the red color); right column, skin autofluorescence channel (the presence of skin fluorophores is indicated by the green color). Arrows point to regions where SRG is only localized within the corneocyte-lipid interface (i.e. SRG is not present throughout the entire intercellular region). Bar = 20 μm.

5.4 CONCLUSIONS

In this chapter, eight FPEs have been identified for transdermal applications, with the best FPEs exhibiting skin current ERs similar to that of SLS, a well-known potent penetration enhancer. TPM was utilized to directly and non-invasively visualize FPEs within skin for the first time, including: (i) visualizing glycerol-mitigated and ultrasound-enhanced FPE skin penetration, (ii) visually confirming that SRB does not penetrate as readily into the skin as SRG, which is consistent with the finding that SRG is a significant FPE while SRB is not, and (iii) using dual-channel TPM to demonstrate the visualization of a FPE with respect to the skin structure. These demonstrations reinforce the novel strategy of combining FPEs with well-established fluorescence techniques to elucidate mechanisms of penetration enhancement and skin irritation. FPEs will allow a multitude of fluorescence techniques to be utilized in order to directly visualize penetration-enhanced transdermal drug delivery. With further studies, more potent transdermal FPEs may be designed. New physical insights obtained using this approach will aid in designing effective penetration enhancers for transdermal drug delivery applications. The exciting results presented in this chapter lay the foundation for the future work proposed in the next chapter.

CHAPTER 6

SUMMARY OF CONTRIBUTIONS, IMPACT, AND RECOMMENDATIONS

The unifying theme throughout this thesis has been the development of novel experimental strategies and analyses that can be utilized in *in vitro* investigations of passive and ultrasound-enhanced transdermal drug delivery. This thesis is concluded with a summary of each chapter's contributions and impact. As discussed below, the experimental strategies presented in this thesis open doors for investigations in several transdermal fields, including evaluating nanoparticle skin toxicity, designing nanoparticle drug delivery carriers, evaluating ultrasound-assisted transdermal vaccination, elucidating mechanisms of chemical penetration enhancer-induced skin irritation, designing topical formulations with penetration enhancers, and elucidating ultrasound and penetration enhancer synergism in enhancing skin permeability. Finally, detailed recommendations are offered for future studies.

6.1 THESIS CONTRIBUTIONS AND IMPACT

6.1.1 CHAPTER 3

Chapter 3 demonstrated that pig split-thickness skin (STS) is a suitable *in vitro* skin model for investigating the US/SLS-enhanced delivery of hydrophilic permeants. To attain this goal, first, a method of data analysis was developed to evaluate the rate of permeant accumulation in the receiver chamber of a Franz diffusion cell to determine if permeant diffusion

across skin occurred under steady-state, sink conditions. A second method of data analysis was developed to apply the aqueous porous pathway model (APPM) to compare log permeability – log resistivity data sets from various skin models. These methods were applied to three human skin models and two pig skin models of varying thicknesses. Skin thickness was determined to affect the response of the human skin models to US/SLS treatment, while the difference in thickness did not affect the response of the two pig skin models to US/SLS treatment. This difference in results for pig and human skin models was attributed to intrinsic differences within the skin models. Finally, to motivate the use of STS in future studies, it was demonstrated that the dermis acts as a barrier to two model, hydrophilic macromolecules (gold nanoparticles and quantum dots).

After the completion of this study, another study was designed based on the two methods of data analysis developed in Chapter 3. Specifically, I assisted in designing and conducting another study in which the APPM-based analysis was applied to compare the effect of SLS on US-induced skin structural perturbation within full-thickness skin and STS models [97]. In this study, the structural parameters of skin treated with US/SLS and US were compared in order to quantify the effect of SLS on skin structural perturbation within US-treated skin [97].

In addition, after demonstrating that pig STS is a convenient skin model for evaluating the US/SLS-enhanced delivery of macromolecules, the pig STS model was used in Chapter 4 for the US/SLS-enhanced delivery of quantum dots. STS has minimal variation in dermal thickness; therefore, the use of STS in this study reduced the variability in: (i) the amount of quantum dots quantified in the dermis by elemental analysis (see Chapter 4, Section 4.2.6.1), and (ii) the compression of the skin when it is mounted into an imaging chamber for confocal microscopy

analysis (see Chapter 4, Section 4.2.6.2), which affects the observed quantum dot penetration depth.

Finally, the STS model will be useful in future studies of the delivery of permeants such as vaccines *into*, rather than *across*, US/SLS-treated skin. Specifically, when the drug delivery targets are the Langerhans cells or the blood capillaries at the epidermis-dermis junction [135], it will be desirable to conduct *in vitro* US/SLS-enhanced transdermal diffusion experiments using STS models, in which much of the dermis is removed in order to more accurately represent the *in vivo* transdermal diffusion barrier between the skin surface and the desired skin component.

6.1.2 CHAPTER 4

In Chapter 4, the US/SLS treatment was applied to enhance the transdermal delivery of nanoparticles, which was evaluated both quantitatively and qualitatively. Using elemental analysis, quantum dot (QD) penetration into the dermis of untreated skin was demonstrated quantitatively for the first time.* In addition, the US/SLS treatment was shown to significantly enhance QD transdermal penetration by 500 – 1300%. Qualitatively, a novel application of confocal microscopy was developed to visualize the penetration of QDs into the dermis. Using confocal microscopy, QDs were observed to penetrate into skin in heterogeneous patterns, thus explaining why the literature contains conflicting reports regarding the ability of nanoparticles to penetrate skin. Finally, it was demonstrated that a more highly cationic surface charge does not necessarily result in greater nanoparticle skin penetration.

Future studies should be conducted to determine the optimum cationic surface charge for nanoparticle skin penetration. Nanoparticle surface charge can potentially be designed to target

* Note that QD penetration into the dermis of US/SLS-treated skin was quantified for the first time in Chapter 3, where QDs were used as a model macromolecule to demonstrate that the dermis acts as a barrier to macromolecules.

particular entities within the skin at specific penetration depths. Subsequently, US/SLS treatment followed by the passive application of cationic nanoparticle carriers can be a good strategy, not only for transdermal drug delivery, but also for topical drug delivery and for transcutaneous immunization. The US/SLS-enhanced delivery of a nanoparticle carrier is particularly relevant for transcutaneous immunization. First, a nanoparticle carrier can enhance the delivery of a vaccine to the dendritic cells within skin, and furthermore, the carrier can be targeted to enhance the specific uptake of the vaccine by the dendritic cells [91]. Second, the US/SLS treatment can enhance the immune response induced by simple, naked vaccine application by enhancing the penetration of the vaccine and by acting as an adjuvant [47,48,136]. Therefore, the combined application of cationic nanoparticle carriers to US/SLS-treated skin is proposed as an interesting and valuable tool for further developing transcutaneous immunization.

In addition, the combination of quantitative and qualitative methods to evaluate nanoparticle penetration into skin can be implemented in other transdermal applications besides drug delivery, e.g. to address the hypothesis that assessment of nanoparticle skin penetration depends on the skin model, as well as to address conflicting reports regarding nanoparticle skin toxicity (see Chapter 4, Section 4.4.1 for a detailed discussion).

6.1.3 CHAPTER 5

In Chapter 5, a novel concept was proposed to use fluorescent chemical penetration enhancers (FPEs) in order to take advantage of a multitude of well-established fluorescence technologies and gain new insights into the behavior of penetration enhancers within skin. Twelve FPE candidates were selected, and eight were demonstrated to be significant transdermal FPEs, where the best FPEs found compared well to sodium lauryl sulfate, a well-known potent

skin penetration enhancer. Based on the ranking of the FPEs, design principles for FPEs were presented. Two-photon fluorescence microscopy was used to directly and non-invasively visualize the penetration patterns of FPEs within skin for the first time.

In future studies, FPEs can be combined with advanced fluorescence technologies to shed light on the behavior of penetration enhancers within biological membranes and elucidate the mechanisms involved in penetration enhancement and membrane irritation. The FPE candidates identified in Chapter 5 can also be evaluated using lipid-based membranes associated with other drug delivery routes (e.g. corneal, buccal, and intestinal). Certain skin penetration enhancers have previously been shown to be effective in other types of lipid-based membranes, including the buccal mucosa [104].

Transdermal FPEs can also be utilized to aid in designing safe and effective skin treatments and topical formulations, e.g. in the cosmetics and personal care industries. Many transdermal products contain penetration enhancers. By adding a FPE to a series of formulations, one can visually compare how various formulations affect the penetration and spatial distribution of the FPE within skin, as demonstrated in Section 5.3.2.1. In addition, by using a red-emitting FPE and dual-channel imaging as demonstrated in Section 5.3.2.3, one can simultaneously visualize the effect of the FPE on the integrity of the skin structure.

Finally, the successful transdermal FPEs identified in Chapter 5 can serve as the basis for designing a homologous series of FPEs that vary in one property (e.g., head group, charge, and tail length) in order to visually investigate the effect of this property in transdermal applications. For example, acridine orange 10-nonyl bromide (AO) exhibited a significant skin current enhancement ratio (see Chapter 5, Section 5.3.1). Since the synthesis of acridine orange derivatives with various tail lengths is relatively straightforward (from acridine orange

hydrochloride hydrate and alkyl bromides [137]), AO has inspired a homologous series of FPEs for visually investigating the effect of tail length on skin penetration and irritation. I am currently assisting with evaluating this series of acridine orange derivatives (with hydrocarbon tail lengths of 8 – 16 carbons) for potency as transdermal FPEs and for combination with US as synergistic penetration enhancers, and I am utilizing two-photon fluorescence microscopy to investigate the effect of the tail length on the spatial distribution of the FPE within untreated and US-treated skin. Other specific examples of designing FPE candidates based on the ones evaluated in Chapter 5 are discussed in Section 6.2.3.

6.2 Detailed Recommendations for Future Studies

6.2.1 Evaluating Other Split-Thickness Skin Models

The results of Chapter 3 strongly suggest the use of STS to investigate the US/SLS-enhanced delivery of hydrophilic macromolecules. If one wishes to obtain US/SLS-enhanced STS permeabilities that are not significantly different than those obtained using full-thickness skin (FTS), the findings suggest the use of 700-μm thick pig STS as an alternative skin model to pig FTS. Additional experiments would be needed to investigate the effects of US/SLS on pig STS models thinner than 700 μm. Pig STS models thinner than 450 μm have already been determined to be unsuitable for US/SLS studies (see Chapter 3, Section 3.6). Therefore, additional studies should investigate intermediate thicknesses between 700 μm and 450 μm in order to determine the threshold thickness for which pig STS is suitable for US/SLS studies. Regarding human STS, since 700-μm thick human skin and human FTS respond differently to the US/SLS treatment described in Chapter 3, other US/SLS conditions (e.g. milder treatments at lower US intensities) or human STS models thicker than 700 μm may be evaluated. Then, as

described in Sections 6.1.1 and 6.1.2, validated STS models can be used to study the US/SLS-enhanced delivery of nanoparticle-encapsulated vaccines into skin.

6.2.2 Evaluating the Split-Thickness Skin Model for the US/SLS-Enhanced Transdermal Delivery of Hydrophobic Permeants

This proposed study is a natural continuation of the study presented in Chapter 3, to compare the US/SLS-enhanced delivery of *hydrophobic* permeants through FTS and STS. For hydrophilic permeants, FTS and STS were compared using analyses based on the aqueous porous pathway model for hydrophilic permeants. At this time, there is no analogous theoretical transport model that can be readily applied to compare the pathways that *hydrophobic* permeants utilize to permeate US/SLS-treated skin. While there are several structure-based models for the transport of hydrophobic permeants through the stratum corneum (e.g. [138]), the application of these models requires isolating the stratum corneum as an intact membrane for permeation experiments, which is not possible for US/SLS-treated skin because US/SLS disrupts the stratum corneum. Therefore, I suggest the use of a non-invasive, fluorescence-based quantitative analysis as an alternative method to compare the hydrophobic transport pathways through the stratum corneum of US/SLS-treated pig FTS and STS. Note that this method assumes that the stratum corneum remains a significant diffusion barrier to hydrophobic permeants after US/SLS treatment. This has been confirmed in separate experiments (see Appendix, Section 6.3).

With the above motivation in mind, confocal or two-photon fluorescence microscopy can be used to visualize the hydrophobic transport pathways through the stratum corneum of US/SLS-treated pig FTS and STS. A hydrophobic fluorescent dye is necessary to probe the hydrophobic transport pathways, and rhodamine B hexyl ester (RBHE) has previously been used

in transdermal studies for this purpose (e.g. [54,111,121,139,140]). However, considering the recent publication by Polat *et al.* which showed that sulforhodamine B (SRB) (a rhodamine dye that has often been used as a model *hydrophilic* probe) is actually *amphiphilic* [114], it would be prudent to verify that RBHE does not exhibit amphiphilic properties. In addition, in light of the results presented in Chapter 5, which showed that some rhodamine dyes can act as transdermal penetration enhancers, it would also be prudent to verify that RBHE does not act as a penetration enhancer. Note that while SRB was shown to be an insignificant passive penetration enhancer (without US), Polat *et al.* showed that SRB and US exhibit synergism as penetration enhancers [114]. If one includes a fluorescent dye in the coupling medium during US treatment, which is often done to visualize the US/SLS-enhanced transport pathways or regions within skin [27,28], then the determination that the fluorescent dye is not a passive penetration enhancer would be insufficient; one would also need to determine whether the dye exhibits synergism with US in enhancing skin penetration. These steps must be taken before using RBHE (or any other dye) as a model hydrophobic probe in future studies. Otherwise, if the probe is not "inert", then the analysis of the results of this proposed study would not be straightforward.

Upon selecting an appropriate hydrophobic probe to visualize the hydrophobic transdermal transport pathways, quantitative analyses which have previously been described [111] can be applied to the confocal or two-photon microscopy images to compare the following properties of hydrophobic probe penetration into US/SLS-treated pig FTS and STS: (i) the vehicle-to-skin partition coefficient, (ii) the concentration gradient, and (iii) the effective diffusion path length. In this manner, the hydrophobic transport pathways between FTS and STS can be non-invasively, yet quantitatively, compared to determine if STS is a suitable alternative skin model for the US/SLS-enhanced delivery of hydrophobic permeants.

6.2.3 Evaluating Additional FPE Candidates

After successfully identifying transdermal FPEs in Chapter 5, these structures can serve as the basis for selecting or synthesizing more FPE candidates. Below, several interesting molecules are listed. The chemical structures of these molecules are provided in Figure 6-1.

- DCDHF exhibited great potential as a FPE for transdermal applications, but it is limited by its poor water solubility. This structure, which has been shown to be readily derivatized [128,129], may be improved by adding a water-soluble group such as sulfonic acid (e.g. fluorophore 21 in [129]; see Figure 6-1, molecule 1).
- The BODIPY group is a desirable fluorophore because its robust fluorescence properties are highly favorable for many imaging techniques [126]. Given that BODIPY1 is a better chemical enhancer than BODIPY2, it would be interesting to evaluate a compound such as molecule 2, shown in Figure 6-1. In molecule 2, the BODIPY group is positioned between the head and tail groups, which is hypothesized to result in a more potent FPE.
- It has previously been shown that chemical penetration enhancement depends strongly upon the head group [112]. Since BODIPY1 and BODIPY2 with carboxylic acid head groups are transdermal FPEs, it would be interesting to evaluate a BODIPY molecule with a sulfate head (see Figure 6-1, molecule 3). This is hypothesized to result in a more potent FPE because the sulfate head group likely contributes to the potency of SLS as a penetration enhancer. Molecule 3 has previously been available through Invitrogen (Carlsbad, CA) as catalog number D3862, however it is currently a discontinued product. Nevertheless, it could be obtained from Invitrogen as a custom synthesis.

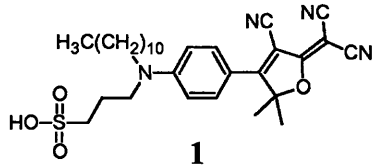

1

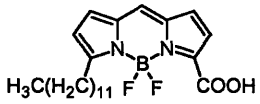

2

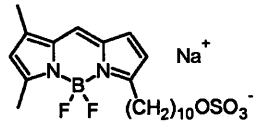

3

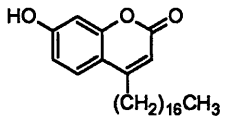

4

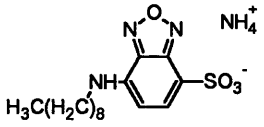

5

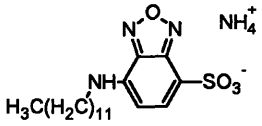

6

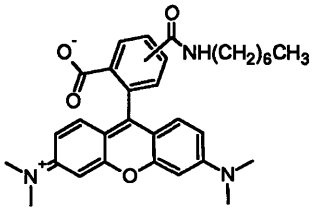

7

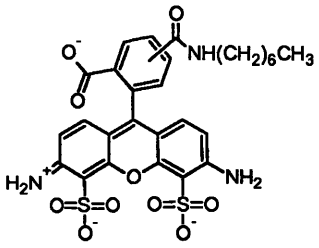

8

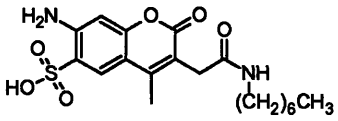

9

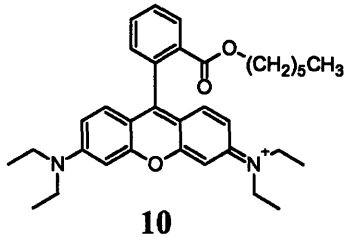

10

FIGURE 6-1: Additional molecules that may be considered for evaluation as fluorescent penetration enhancers.

- Another discontinued Invitrogen product is H22730 (see FIGURE 6-1, molecule 4), which was marketed as an amphiphilic coumarin fluorescent dye. This molecule would be interesting to evaluate as a FPE because it has a low molecular weight of 400 Daltons, a compact fluorophore, and a long hydrocarbon tail. This could be obtained from Invitrogen as a custom synthesis. It would also be interesting to synthesize a derivative with a tail length of twelve carbons, which has previously been shown to be the optimal tail length for chemical penetration enhancement [112].
- Molecules 5 and 6 were synthesized by Brett VanVeller in Professor Timothy Swager's laboratory in the MIT Department of Chemistry. These molecules have long hydrocarbon tails and compact fluorophores located adjacent to the sulfonate head groups. They were synthesized by reacting 4-chloro-7-sulfobenzofurazan ammonium salt (Sigma C1154) with nonylamine and with dodecylamine, respectively [141]. Prior to purification, molecule 5 exhibited a statistically significant skin current enhancement ratio of 5.9 ± 1.8 (mean $\pm$ 95% confidence interval; $n = 10$) in preliminary experiments conducted as described in Chapter 5, Section 5.2.6. It is hypothesized that molecule 6 would exhibit a greater enhancement ratio than molecule 5 because a 12-carbon tail length has previously been shown to be optimal for penetration enhancement [112]. It would be interesting to rigorously evaluate these molecules after purification.
- Molecule 7 was synthesized by Amanda Engler in Professor Paula Hammond's laboratory in the MIT Department of Chemical Engineering. It was synthesized by reacting 5/6-carboxy-tetramethyl-rhodamine succinimidyl ester (Thermo Scientific Pierce 46406) with heptylamine to form the amide. The motivation for synthesizing this molecule is as follows. Several rhodamine derivates were determined to be transdermal FPEs in Chapter 5, in spite

of the fact that they do not have long hydrocarbon tail groups. Therefore, it was hypothesized that the addition of a hydrocarbon tail to a rhodamine derivative would result in a potent penetration enhancer. Prior to purification, molecule 7 (which is a mixture of isomers) exhibited a statistically significant skin current enhancement ratio of 6.8 ± 3.1 (mean $\pm$ 95% confidence interval; $n = 9$) in preliminary experiments conducted as described in Chapter 5, Section 5.2.6. It would be interesting to rigorously evaluate these molecules after the separation of isomers and the subsequent purification.

- Molecule 7 was synthesized using a common synthetic route for amide formation, which can be used to add hydrocarbon tails of various lengths to other fluorophores. For example, molecules 8 and 9 can be synthesized by reacting heptylamine with Alexa Fluor 488 carboxylic acid succinimidyl ester (Invitrogen A20100) and Alexa Fluor 350 carboxylic acid succinimidyl ester (Invitrogen A10168), respectively. Molecule 8 is interesting because it contains two sulfonate groups, which would impart significant water solubility to the molecule. Molecule 9 is interesting because it has a compact fluorophore located adjacent to several water-soluble functional groups. Note that the tail length of these molecules could be varied by using amines with various hydrocarbon chain lengths in the synthesis.
- Yet another rhodamine derivative that contains a hydrocarbon chain is rhodamine B hexyl ester (RBHE), which is commercially available (see FIGURE 6-1, molecule 10). However, regarding molecules such as 7 and 10: Note that Polat *et al.* showed that sulforhodamine B (SRB) has defined polar ("head") and non-polar ("tail") regions. The division between the head and the tail can be made by laterally bisecting the 3-ring xanthene structure, with the section of SRB containing the sulfonate groups (see Chapter 5, FIGURE 5-1) comprising the head [114]. Assuming that this division is consistent for all rhodamine derivatives, then in

these molecules, the hydrocarbon chain branching off the head group may be considered to be a *second* tail group. Therefore, the analysis of the structure-activity relationship of these molecules may not be straightforward.

6.2.4 Investigating the Role of Amphiphilicity in the Structure-Activity Relationship of FPEs

Since amphiphilicity was the general basis for choosing the FPE candidates selected in Chapter 5, it would be interesting to rank the FPEs according to amphiphilicity and to determine if there is a correlation between amphiphilicity and potency. Regarding amphiphilicity, note that the oil/water interfacial tension measurements described in Chapter 5 cannot be applied to all of the FPE candidates because not all of them are soluble in either decane or water. Therefore, in order to rank the FPEs according to amphiphilicity, another oil/water system must be chosen, or another metric must be used for this study. Regarding potency, one must obtain statistically significant differences among the skin current enhancement ratios (ERs) exhibited by the FPEs in order to rigorously determine if there is a correlation between amphiphilicity and potency. In Chapter 5, the experiment for evaluating the potency of FPE candidates was designed to be applicable to 11 of the 12 selected FPE candidates (measurement of the ER exhibited after a 24-hour application of the FPE candidate to the skin at 1 mM in 40% ethanol). This design resulted in a relatively small difference in the ERs exhibited by the positive and negative controls (see Chapter 5, Figure 5-6), making it difficult to obtain a statistically significant ranking among the FPE candidates. In order to obtain a statistically significant ranking, either many replicates are required in order to increase the confidence level in the data or the experimental conditions need to be modified.

To overcome the above challenges, this study could be conducted for a subset of FPEs that are water soluble. As a result, first, surface tension measurements at an air-water interface could be used to rank the FPEs by amphiphilicity. Second, this would allow a larger concentration of solute to be used when evaluating the potency of the FPE (up to the water solubility limit of the FPEs). In turn, this would increase the difference in ERs exhibited by the positive and negative controls, thereby making it easier to obtain statistically significant differences in ERs among the FPEs. Note that by using only water-soluble FPEs, ethanol would not be needed as a co-solvent. The removal of ethanol from the system would also help in obtaining a larger difference in the ERs exhibited by the positive and negative controls because the FPEs would not need to compete with ethanol as a penetration enhancer.

At this time, only a few of the FPEs identified in Chapter 5 are significantly water soluble for this proposed study. Several molecules identified in Section 6.2.3 should be evaluated prior to this study in order to increase the number of water-soluble FPEs. Then, if there is a strong correlation between amphiphilicity and potency of water-soluble FPEs, the visualization of the FPEs within skin would assist in elucidating the mechanism of penetration enhancement by amphiphiles. In addition, amphiphilicity may be included as a new parameter in structure-activity relationships for penetration enhancers and in designing potent penetration enhancers. Furthermore, amphiphilic fluorescent molecules, or fluorosurfactants, would be useful in many other fields, e.g. cosmetic and pharmaceutical topical formulation design, surfactant-induced skin irritation, and surfactant-enhanced transdermal drug delivery. Specifically, fluorosurfactants that can penetrate into skin can be utilized to visualize how mixing surfactants can be used to decrease skin penetration and irritation. One can visualize how the distribution, composition, and concentration of the fluorescent surfactant in the skin are changed by: (i) mixing with traditional

surfactants, (ii) adding a humectant, and (iii) adding a polymer. The Blankschtein Lab has previously shown that these strategies can be used to modulate the skin penetration of traditional surfactants [110,120,132,142,143]. Generalizing these studies using a fluorosurfactant would be very exciting, and would be of great interest to the cosmetics and personal care products industries.

6.3 Appendix: Evaluation of the Stratum Corneum's Diffusion Barrier to Hydrophobic Permeants after US/SLS Treatment

6.3.1 Materials and Methods

6.3.1.1 Skin Preparation

700-μm thick pig split-thickness skin samples were prepared as described in Chapter 3, Section 3.2.2. Next, US/SLS treatment was applied to the skin samples as described in Chapter 4, Section 4.2.4. Samples prepared using this method are referred to hereafter as "intact" skin. Subsequently, "tape-stripped" skin was prepared from intact skin by repeated tape stripping, using up to 35 strips of Scotch® book tape (3M, St. Paul, Minnesota) until the stratum corneum was removed. This endpoint was achieved when the epidermal surface glistened and the tape strips no longer removed any skin fragments. Note that tape-stripping is a commonly reported method for removing the stratum corneum.

6.3.1.2 Naphthol Permeation through Skin

Naphthol was selected as a model hydrophobic permeant because it has previously been used for transdermal diffusion experiments [138,144,145]. 1-^{14}C-labeled naphthol-α in ethanol

(55 mCi/mmol) was obtained from American Radiolabeled Chemicals (St. Louis, Missouri). All other general chemicals were obtained and prepared as described in Chapter 3, Section 3.2.1. The naphthol stock solution was prepared by drying the naphthol using compressed air in order to remove the ethanol. Then, PBS was added to obtain a concentration of 1 μCi/mL, and the solution was 0.02-μm filtered.

Intact and tape-stripped skin samples were mounted into clean, dry Franz diffusion cells. 12 mL of PBS was added to the receiver chambers, and 0.5 mL of naphthol donor solution was added to the donor chambers. Diffusion experiments were conducted for 2 hours at room temperature (25°C) and under occluded conditions by sealing the donor chambers with parafilm. The donor solutions were replaced every 30 minutes in order to maintain a constant donor concentration. The receiver solutions were magnetically stirred at 500 RPM.

1-mL samples were withdrawn from the receiver chambers at 10-minute intervals from 60 to 110 minutes after the start of the experiment. Each receiver solution sample was immediately replaced with an equal volume of PBS. After mixing each sample with 15 mL of Hionic-Fluor scintillation cocktail, the radioactivity of the samples was measured using a Tri-Carb 2810TR liquid scintillation analyzer (PerkinElmer, Waltham, Massachusetts). These data were utilized to calculate the concentration of naphthol in the receiver chamber from 60 to 110 minutes, taking into account the replacement of the receiver samples and the background radioactivity [28]. The data were analyzed using the methods described in Chapter 3, Section 3.2.9.

6.3.2 RESULTS AND DISCUSSION

The stratum corneum is widely regarded as the primary barrier to transdermal diffusion. However, after treating the skin with US/SLS, it was not clear whether the stratum corneum or the hydrophilic epidermis is the primary diffusion barrier to hydrophobic permeants. Therefore, the permeation of naphthol through US/SLS-treated intact and tape-stripped skin was compared. As shown in FIGURE 6-2, naphthol diffused through tape-stripped skin at a significantly faster rate than through intact skin. There is a statistically significant difference between the naphthol concentrations at each time point between 60 and 110 minutes. Furthermore, there is a statistically significant difference between the slopes of the linear regressions fitted to the data shown in FIGURE 6-2. These results indicate that the stratum corneum remains a significant diffusion barrier to hydrophobic permeants after US/SLS treatment.

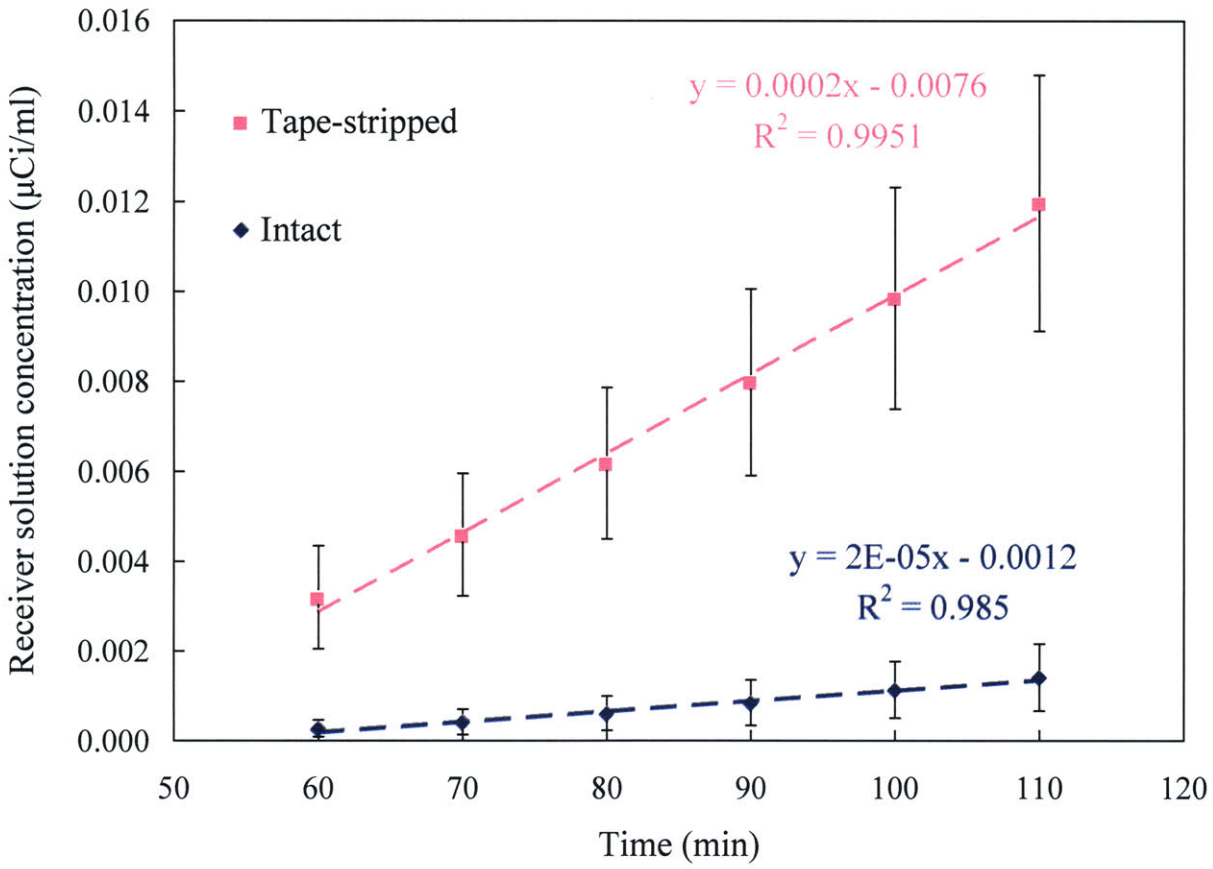

FIGURE 6-2: Comparison of naphthol permeation through US/SLS-treated intact skin and tape-stripped skin. The data points are the mean of n replicates: $n = 3$ for intact skin and $n = 7$ for tape-stripped skin. Error bars indicate 95% confidence intervals. The dashed lines represent the linear regressions fitted to each data set. The corresponding linear regression parameters are shown in the figure.

BIBLIOGRAPHY

[1] VV Ranade. Drug delivery systems 5A. Oral drug delivery. Journal of Clinical Pharmacology 31, 2-16 (1991).

[2] VV Ranade. Drug delivery systems 5B. Oral drug delivery. Journal of Clinical Pharmacology 31, 98-115 (1991).

[3] RD Gordon and TA Peterson. 4 myths about transdermal drug delivery. Drug Delivery Technology 3, 44-50 (2003).

[4] Food and Drug Administration. Electronic Orange Book. www.fda.gov/cder/ob (2006).

[5] Drug Digest. Estradiol and norethindrone transdermal patch. http://www.drugdigest.org/DD/DVH/Uses/0,3915,550530%7CEstradiol+and+Norethindrone+Transdermal+Patch,00.html (2005).

[6] DS Wishart, C Knox, AC Guo, S Shrivastava, M Hassanali, P Stothard, Z Chang, and J Woolsey. DrugBank: a comprehensive resource for in silico drug discovery and exploration. Nucleic Acids Research 34, D668-D672 (2006).

[7] KA Walters and MS Roberts. The structure and function of skin. In KA Walters, editor. Dermatological and Transdermal Formulations. New York: Marcel Dekker, Inc., 1-39 (2002).

[8] S Gochnour. Transdermal Products: Key Formulation, Development, Materials, and Process Considerations. PowerPoint Presentation.

[9] J Kushner. Theoretical and experimental investigations of passive and ultrasound-enhanced transdermal drug delivery. PhD Thesis, Massachusetts Institute of Technology (2006).

[10] A Jadoul, J Bouwstra, and V Preat. Effects of iontophoresis and electroporation on the stratum corneum. Review of the biophysical studies. Advanced Drug Delivery Reviews 35, 89-105 (1999).

[11] B Shroot and D Aust. Current trends in dermatologicals and delivery systems. In JJ Wille, editor. Skin Delivery Systems: Transdermals, Dermatologicals, and Cosmetic Actives. Blackwell Publishing, 129-135 (2006).

[12] RA Thakur, Y Song, and BB Michniak. Chemical enhancers. In JJ Wille, editor. Skin Delivery Systems: Transdermals, Dermatologicals, and Cosmetic Actives. Blackwell Publishing, 277-295 (2006).

[13] S Mitragotri. Effect of bilayer disruption on transdermal transport of low-molecular weight hydrophobic solutes. Pharmaceutical Research 18, 1018-1023 (2001).

[14] AC Williams and BW Barry. Penetration enhancers. Advanced Drug Delivery Reviews 56, 603-618 (2004).

[15] S Mitragotri. Synergistic effect of enhancers for transdermal drug delivery. Pharmaceutical Research 17, 1354-1359 (2000).

[16] K Moser, K Kriwet, C Froehlich, A Naik, YN Kalia, and RH Guy. Permeation enhancement of a highly lipophilic drug using supersaturated systems. Journal of Pharmaceutical Sciences 90, 607-616 (2001).

[17] JA Mikszta, MI Haider, and RJ Pettis. Microneedles for drug and vaccine delivery: when will the dream become a reality? In JJ Wille, editor. Skin Delivery Systems: Transdermals, Dermatologicals, and Cosmetic Actives. Blackwell Publishing, 309-325 (2006).

[18] VP Zharov and AS Latyshev. Laser ultrasonic transport of drugs in living tissues. Annals of the New York Academy of Sciences 858, 66-73 (1998).

[19] S Mitragotri, D Ray, J Farrell, H Tang, B Yu, J Kost, D Blankschtein, and R Langer. Synergistic effect of low-frequency ultrasound and sodium lauryl sulfate on transdermal transport. Journal of Pharmaceutical Sciences 89, 892-900 (2000).

[20] L Le, J Kost, and S Mitragotri. Combined effect of low-frequency ultrasound and iontophoresis: applications for transdermal heparin delivery. Pharmaceutical Research 17, 1151-1154 (2000).

[21] A Tezel, A Sens, J Tuchscherer, and S Mitragotri. Synergistic effect of low-frequency ultrasound and surfactants on skin permeability. Journal of Pharmaceutical Sciences 91, 91-100 (2002).

[22] J Kost, U Pliquett, S Mitragotri, A Yamamoto, R Langer, and J Weaver. Synergistic effect of electric field and ultrasound on transdermal transport. Pharmaceutical Research 13, 633-638 (1996).

[23] ME Johnson, S Mitragotri, A Patel, D Blankschtein, and R Langer. Synergistic effects of chemical enhancers and therapeutic ultrasound on transdermal drug delivery. Journal of Pharmaceutical Sciences 85, 670-679 (1996).

[24] S Mitragotri, D Blankschtein, and R Langer. Ultrasound-mediated transdermal protein delivery. Science 269, 850-853 (1995).

[25] S Mitragotri, D Blankschtein, and R Langer. Transdermal drug delivery using low-frequency sonophoresis. Pharmaceutical Research 13, 411-420 (1996).

[26] H Tang, CCJ Wang, D Blankschtein, and R Langer. An investigation of the role of cavitation in low-frequency ultrasound-mediated transdermal drug transport. Pharmaceutical Research 19, 1160-1169 (2002).

[27] BE Polat, D Hart, R Langer, and D Blankschtein. Ultrasound-mediated transdermal drug delivery: Mechanisms, scope, and emerging trends. Journal of Controlled Release (2011, in press).

[28] J Kushner, D Blankschtein, and R Langer. Heterogeneity in skin treated with low-frequency ultrasound. Journal of Pharmaceutical Sciences 97, 4119-4128 (2008).

[29] BE Polat, PL Figueroa, D Blankschtein, and R Langer. Transport pathways and enhancement mechanisms within localized and non-localized transport regions in skin treated with low-frequency sonophoresis and sodium lauryl sulfate. Journal of Pharmaceutical Sciences 100, 512-529 (2011).

[30] BE Polat, D Blankschtein, and R Langer. Low-frequency sonophoresis: application to the transdermal delivery of macromolecules and hydrophilic drugs. Expert Opinion on Drug Delivery 7, 1415-1432 (2010).

[31] S Mitragotri, J Farrell, H Tang, T Terahara, J Kost, and R Langer. Determination of threshold energy dose for ultrasound-induced transdermal drug transport. Journal of Controlled Release 63, 41-52 (2000).

[32] T Terahara, S Mitragotri, J Kost, and R Langer. Dependence of low-frequency sonophoresis on ultrasound parameters; distance of the horn and intensity. International Journal of Pharmaceutics 235, 35-42 (2002).

[33] A Tezel, A Sens, and S Mitragotri. A theoretical analysis of low-frequency sonophoresis: dependence of transdermal transport pathways on frequency and energy density. Pharmaceutical Research 19, 1841-1846 (2002).

[34] H Chuang, E Taylor, and TW Davison. Clinical evaluation of a continuous minimally invasive glucose flux sensor placed over ultrasonically permeated skin. Diabetes Technology & Therapeutics 6, 21-30 (2004).
[35] BM Becker, S Helfrich, E Baker, K Lovgren, PA Minugh, and JT Machan. Ultrasound with topical anesthetic rapidly decreases pain of intravenous cannulation. Academic Emergency Medicine 12, 289-295 (2005).
[36] NP Katz, DE Shapiro, TE Herrmann, J Kost, and LM Custer. Rapid onset of cutaneous anesthesia with EMLA cream after pretreatment with a new ultrasound-emitting device. Anesthesia and Analgesia 98, 371-376 (2004).
[37] J Gupta and MR Prausnitz. Recovery of skin barrier properties after sonication in human subjects. Ultrasound in Medicine & Biology 35, 1405-1408 (2009).
[38] BE Polat, WM Deen, R Langer, and D Blankschtein. A physical mechanism to explain the synergism in transdermal enhancement between low-frequency ultrasound and chemical penetration enhancers. Journal of Controlled Release (submitted).
[39] S Skarbek-Borowska, BM Becker, K Lovgren, A Bates, and PA Minugh. Brief focal ultrasound with topical anesthetic decreases the pain of intravenous placement in children. Pediatric Emergency Care 22, 339-345 (2006).
[40] WT Zempsky, B Robbins, and K McKay. Reduction of topical anesthetic onset time using ultrasound: a randomized controlled trial prior to venipuncture in young children. Pain Medicine 9, 795-802 (2008).
[41] CP Stowell, M-Q Trieu, H Chuang, N Katz, and C Quarrington. Ultrasound-enabled topical anesthesia for pain reduction of phlebotomy for whole blood donation. Transfusion 49, 146-153 (2009).
[42] Perkin Elmer website, http://las.perkinelmer.com/Catalog/ProductInfoPage.htm?ProductID=B281000. (12/08/2010).
[43] Boyle group website, http://boyle.mit.edu/~ed/Instrumentation. (12/08/2010).
[44] MR Prausnitz and R Langer. Transdermal drug delivery. Nature Biotechnology 26, 1261-1268 (2008).
[45] HA Benson and S Namjoshi. Proteins and peptides: strategies for delivery to and across the skin. Journal of Pharmaceutical Sciences 97, 3591-3610 (2008).
[46] M Ogura, S Paliwal, and S Mitragotri. Low-frequency sonophoresis: current status and future prospects. Advanced Drug Delivery Reviews 60, 1218-1223 (2008).
[47] A Dahlan, HO Alpar, P Stickings, D Sesardic, and S Murdan. Transcutaneous immunisation assisted by low-frequency ultrasound. International Journal of Pharmaceutics 368, 123-128 (2009).
[48] A Tezel, S Paliwal, Z Shen, and S Mitragotri. Low-frequency ultrasound as a transcutaneous immunization adjuvant. Vaccine 23, 3800-3807 (2005).
[49] RL Bronaugh. Methods for in vitro percutaneous absorption. In H Zhai, K-P Wilhelm, HI Maibach, editors. Marzulli and Maibach's Dermatotoxicology. Florida: CRC Press, 307-310 (2007).
[50] B Baroli. Penetration of nanoparticles and nanomaterials in the skin: fiction or reality? Journal of Pharmaceutical Sciences 99, 21-50 (2010).
[51] J Kushner, D Blankschtein, and R Langer. Experimental demonstration of the existence of highly permeable localized transport regions in low-frequency sonophoresis. Journal of Pharmaceutical Sciences 93, 2733-2745 (2004).

[52] J Kushner, D Blankschtein, and R Langer. Evaluation of the porosity, the tortuosity, and the hindrance factor for the transdermal delivery of hydrophilic permeants in the context of the aqueous pore pathway hypothesis using dual-radiolabeled permeability experiments. Journal of Pharmaceutical Sciences 96, 3263-3282 (2007).

[53] J Kushner, D Blankschtein, and R Langer. Evaluation of hydrophilic permeant transport parameters in the localized and non-localized transport regions of skin treated simultaneously with low-frequency ultrasound and sodium lauryl sulfate. Journal of Pharmaceutical Sciences 97, 906-918 (2008).

[54] J Kushner, D Kim, PT So, D Blankschtein, and RS Langer. Dual-channel two-photon microscopy study of transdermal transport in skin treated with low-frequency ultrasound and a chemical enhancer. Journal of Investigative Dermatology 127, 2832-2846 (2007).

[55] S Mitragotri and J Kost. Transdermal delivery of heparin and low-molecular weight heparin using low-frequency ultrasound. Pharmaceutical Research 18, 1151-1156 (2001).

[56] A Tezel, S Dokka, S Kelly, GE Hardee, and S Mitragotri. Topical delivery of anti-sense oligonucleotides using low-frequency sonophoresis. Pharmaceutical Research 21, 2219-2225 (2004).

[57] S Paliwal, GK Menon, and S Mitragotri. Low-frequency sonophoresis: ultrastructural basis for stratum corneum permeability assessed using quantum dots. Journal of Investigative Dermatology 126, 1095-1101 (2006).

[58] H Tang, D Blankschtein, and R Langer. Effects of low-frequency ultrasound on the transdermal permeation of mannitol: comparative studies with in vivo and in vitro skin. Journal of Pharmaceutical Sciences 91, 1776-1794 (2002).

[59] S Mitragotri and J Kost. Low-frequency sonophoresis: a review. Advanced Drug Delivery Reviews 56, 589-601 (2004).

[60] A Farinha, S Kellogg, K Dickinson, and T Davison. Skin impedance reduction for electrophysiology measurements using ultrasonic skin permeation: initial report and comparison to current methods. Biomedical Instrumentation & Technology 40, 72-77 (2006).

[61] A Verma, O Uzun, Y Hu, HS Han, N Watson, S Chen, DJ Irvine, and F Stellacci. Surface-structure-regulated cell-membrane penetration by monolayer-protected nanoparticles. Nature Materials 7, 588-595 (2008).

[62] AC Allenby, J Fletcher, C Schock, and TFS Tees. The effect of heat, pH, and organic solvents on the electrical impedance and permeability of excised human skin. British Journal of Dermatology 81, 31-39 (1969).

[63] P Karande, A Jain, and S Mitragotri. Relationships between skin's electrical impedance and permeability in the presence of chemical enhancers. Journal of Controlled Release 110, 307-313 (2006).

[64] GB Kasting and LA Bowman. DC electrical properties of frozen, excised human skin. Pharmaceutical Research 7, 134-143 (1990).

[65] J Rosell, J Colominas, P Riu, R Pallas-Areny, and JG Webster. Skin impedance from 1 Hz to 1 MHz. IEEE Transactions on Biomedical Engineering 35, 649-651 (1988).

[66] H Tang, S Mitragotri, D Blankschtein, and R Langer. Theoretical description of transdermal transport of hydrophilic permeants: application to low-frequency sonophoresis. Journal of Pharmaceutical Sciences 90, 545-568 (2001).

[67] A Tezel, A Sens, and S Mitragotri. Incorporation of lipophilic pathways into the porous pathway model for describing skin permeabilization during low-frequency sonophoresis. Journal of Controlled Release 83, 183-188 (2002).
[68] A Tezel, A Sens, and S Mitragotri. Description of transdermal transport of hydrophilic solutes during low-frequency sonophoresis based on a modified porous pathway model. Journal of Pharmaceutical Sciences 92, 381-393 (2003).
[69] H Tang, D Blankschtein, and R Langer. Prediction of steady-state skin permeabilities of polar and nonpolar permeants across excised pig skin based on measurements of transient diffusion: characterization of hydration effects on the skin porous pathway. Journal of Pharmaceutical Sciences 91, 1891-1907 (2002).
[70] P Dechadilok and WM Deen. Hindrance factors for diffusion and convection in pores. Industrial & Engineering Chemistry Research 45, 6953-6959 (2006).
[71] SE dal Belo, LR Gaspar, PMBG Maia Campos, and J-P Marty. Skin penetration of epigallocatechin-3-gallate and quercetin from green tea and ginkgo biloba extracts vehiculated in cosmetic formulations. Skin Pharmacology and Physiology 22, 299-304 (2009).
[72] SG John, JG Park, Z Zhan, and EA Boyle. The isotopic composition of some common forms of anthropogenic zinc. Chemical Geology 245, 61-69 (2007).
[73] JH Zar. Biostatistical Analysis. New Jersey: Prentice Hall. p 372-377 (2009).
[74] SK Li, AH Ghanem, KD Peck, and WI Higuchi. Characterization of the transport pathways induced during low to moderate voltage iontophoresis in human epidermal membrane. Journal of Pharmaceutical Sciences 87, 40-48 (1998).
[75] NJ Vardaxis, TA Brans, ME Boon, RW Kreis, and LM Marres. Confocal laser scanning microscopy of porcine skin: implications for human wound healing studies. Journal of Anatomy 190, 601-611 (1997).
[76] P Karande and S Mitragotri. Dependence of skin permeability on contact area. Pharmaceutical Research 20, 257-263 (2003).
[77] SW Fong, E Klaseboer, CK Turangan, BC Khoo, and KC Hung. Numerical analysis of a gas bubble near bio-materials in an ultrasound field. Ultrasound in Medicine & Biology 32, 925-942 (2006).
[78] A Tezel, A Sens, J Tuchscherer, and S Mitragotri. Frequency dependence of sonophoresis. Pharmaceutical Research 18, 1694-1700 (2001).
[79] RU Pendlington. In vitro percutaneous absorption measurements. In RP Chilcott, S Price, editors. Principles and Practice of Skin Toxicology. England: John Wiley & Sons Ltd., 129-148 (2008).
[80] AM Barbero and HF Frasch. Pig and guinea pig skin as surrogates for human in vitro penetration studies: a quantitative review. Toxicology In Vitro 23, 1-13 (2009).
[81] R Alvarez-Román, G Merino, YN Kalia, A Naik, and RH Guy. Skin permeability enhancement by low-frequency sonophoresis: Lipid extraction and transport pathways. Journal of Pharmaceutical Sciences 92, 1138-1146 (2003).
[82] JS Milton. Statistical Methods in the Biological and Health Sciences. New York: McGraw-Hill. p 373 (1992).
[83] G Cevc and U Vierl. Nanotechnology and the transdermal route: a state of the art review and critical appraisal. Journal of Controlled Release 141, 277-299 (2010).
[84] RR Patlolla, PR Desai, K Belay, and MS Singh. Translocation of cell penetrating peptide engrafted nanoparticles across skin layers. Biomaterials 31, 5598-5607 (2010).

[85] PW Lee, SH Hsu, JS Tsai, FR Chen, PJ Huang, CJ Ke, ZX Liao, CW Hsiao, HJ Lin, and HW Sung. Multifunctional core-shell polymeric nanoparticles for transdermal DNA delivery and epidermal Langerhans cells tracking. Biomaterials 31, 2425-2434 (2010).

[86] TR Kuo, CL Wu, CT Hsu, W Lo, SJ Chiang, SJ Lin, CY Dong, and CC Chen. Chemical enhancer induced changes in the mechanisms of transdermal delivery of zinc oxide nanoparticles. Biomaterials 30, 3002-3008 (2009).

[87] JP Ryman-Rasmussen, JE Riviere, and NA Monteiro-Riviere. Surface coatings determine cytotoxicity and irritation potential of quantum dot nanoparticles in epidermal keratinocytes. Journal of Investigative Dermatology 127, 143-153 (2007).

[88] JP Ryman-Rasmussen, JE Riviere, and NA Monteiro-Riviere. Penetration of intact skin by quantum dots with diverse physicochemical properties. Toxicological Sciences 91, 159-165 (2006).

[89] LW Zhang, WW Yu, VL Colvin, and NA Monteiro-Riviere. Biological interactions of quantum dot nanoparticles in skin and in human epidermal keratinocytes. Toxicology and Applied Pharmacology 228, 200-211 (2008).

[90] X Wu, K Landfester, A Musyanovych, and RH Guy. Disposition of charged nanoparticles after their topical application to the skin. Skin Pharmacology and Physiology 23, 117-123 (2010).

[91] K Park. Nano is better than micro for targeted vaccine delivery. Journal of Controlled Release 144, 117 (2010).

[92] X Wu, GJ Price, and RH Guy. Disposition of nanoparticles and an associated lipophilic permeant following topical application to the skin. Molecular Pharmaceutics 6, 1441-1448 (2009).

[93] B Baroli, MG Ennas, F Loffredo, M Isola, R Pinna, and MA Lopez-Quintela. Penetration of metallic nanoparticles in human full-thickness skin. Journal of Investigative Dermatology 127, 1701-1712 (2007).

[94] JL Matousek and KL Campbell. A comparative review of cutaneous pH. Veterinary Dermatology 13, 293-300 (2002).

[95] MD Abràmoff, PJ Magalhães, and SJ Ram. Image processing with ImageJ. Biophotonics International 11, 36-42 (2004).

[96] R Alvarez-Román, A Naik, YN Kalia, RH Guy, and H Fessi. Skin penetration and distribution of polymeric nanoparticles. Journal of Controlled Release 99, 53-62 (2004).

[97] BE Polat, JE Seto, D Blankschtein, and R Langer. Application of the aqueous porous pathway model to quantify the effect of sodium lauryl sulfate on ultrasound-induced skin structural perturbation. Journal of Pharmaceutical Sciences 100, 1387-1397 (2011).

[98] NA Monteiro-Riviere and B Baroli. Nanomaterial penetration. In NA Monteiro-Riviere, editor. Toxicology of the Skin. New York: Informa Healthcare, 333-346 (2010).

[99] MS Roberts and M Walker. Water: the most natural penetration enhancer. In KA Walters, J Hadgraft, editors. Pharmaceutical Skin Penetration Enhancement. New York: Marcel Dekker, Inc., 1-30 (1993).

[100] JE Seto, BE Polat, RFV Lopez, D Blankschtein, and R Langer. Effects of ultrasound and sodium lauryl sulfate on the transdermal delivery of hydrophilic permeants: comparative in vitro studies with full-thickness and split-thickness pig and human skin. Journal of Controlled Release 145, 26-32 (2010).

[101] P Dechadilok and WM Deen. Electrostatic and electrokinetic effects on hindered convection in pores. Journal of Colloid and Interface Science 338, 135-144 (2009).

[102] E Drakaki, E Borisova, M Makropoulou, L Avramov, AA Serafetinides, and I Angelov. Laser induced autofluorescence studies of animal skin used in modeling of human cutaneous tissue spectroscopic measurements. Skin Research and Technology 13, 350-359 (2007).
[103] AV Zvyagin, X Zhao, A Gierden, W Sanchez, JA Ross, and MS Roberts. Imaging of zinc oxide nanoparticle penetration in human skin in vitro and in vivo. Journal of Biomedical Optics 13, 064031 (2008).
[104] JA Nicolazzo, BL Reed, and BC Finnin. Buccal penetration enhancers--how do they really work? Journal of Controlled Release 105, 1-15 (2005).
[105] Y Sultana, M Aqil, A Ali, and A Samad. Advances in the topical ocular drug delivery. Expert Review of Ophthalmology 2, 309-323 (2007).
[106] P Karande, A Jain, K Ergun, V Kispersky, and S Mitragotri. Design principles of chemical penetration enhancers for transdermal drug delivery. Proceedings of the National Academy of Sciences, USA 102, 4688-4693 (2005).
[107] P Karande, A Jain, and S Mitragotri. Discovery of transdermal penetration enhancers by high-throughput screening. Nature Biotechnology 22, 192-197 (2004).
[108] AP Demchenko. Introduction to Fluorescence Sensing. Dordrecht, Netherlands: Springer (2009).
[109] JW Fluhr, R Darlenski, and C Surber. Glycerol and the skin: holistic approach to its origin and functions. British Journal of Dermatology 159, 23-34 (2008).
[110] S Ghosh, D Kim, P So, and D Blankschtein. Visualization and quantification of skin barrier perturbation induced by surfactant-humectant systems using two-photon fluorescence microscopy. Journal of Cosmetic Science 59, 263-289 (2008).
[111] B Yu, KH Kim, PTC So, D Blankschtein, and R Langer. Visualization of oleic acid-induced transdermal diffusion pathways using two-photon fluorescence microscopy. Journal of Investigative Dermatology 120, 448-455 (2003).
[112] JL Zatz and B Lee. Skin penetration enhancement by surfactants. In MM Rieger, LD Rhein, editors. Surfactants in Cosmetics. New York, NY: Marcel Dekker, 501-517 (1997).
[113] JD Bos and MMHM Meinardi. The 500 Dalton rule for the skin penetration of chemical compounds and drugs. Experimental Dermatology 9, 165-169 (2000).
[114] BE Polat, S Lin, JD Mendenhall, B VanVeller, R Langer, and D Blankschtein. Experimental and molecular dynamics investigation into the amphiphilic nature of sulforhodamine B. Journal of Physical Chemistry B 115, 1394-1402 (2011).
[115] VK Rachakonda, KM Yerramsetty, SV Madihally, RL Robinson, Jr., and KA Gasem. Screening of chemical penetration enhancers for transdermal drug delivery using electrical resistance of skin. Pharmaceutical Research 25, 2697-2704 (2008).
[116] IH Pitman, SJ Rostas, and LM Downes. Effects of breed, season, temperature, and solvents on the permeability of frozen and reconstituted cattle skin to levamisole. Journal of Pharmaceutical Sciences 72, 218-221 (1983).
[117] W Magerl, RA Westerman, B Mohner, and HO Handwerker. Properties of transdermal histamine iontophoresis: differential effects of season, gender, and body region. Journal of Investigative Dermatology 94, 347-352 (1990).
[118] J Schroder. Cutaneous absorption of chemicals. Journal of the South African Veterinary Association 57, 169-176 (1986).

[119] M Mulqueen and D Blankschtein. Theoretical and experimental investigation of the equilibrium oil-water interfacial tensions of solutions containing surfactant mixtures. Langmuir 18, 365-376 (2002).
[120] S Ghosh and D Blankschtein. The role of sodium dodecyl sulfate (SDS) micelles in inducing skin barrier perturbation in the presence of glycerol. Journal of Cosmetic Science 58, 109-133 (2007).
[121] B Yu, C-Y Dong, PTC So, D Blankschtein, and R Langer. In vitro visualization and quantification of oleic acid induced changes in transdermal transport using two-photon fluorescence microscopy. Journal of Investigative Dermatology 117, 16-25 (2001).
[122] RH Na, IM Stender, LX Ma, and HC Wulf. Autofluorescence spectrum of skin: component bands and body site variations. Skin Research and Technology 6, 112-117 (2000).
[123] KS Warner, SK Li, N He, TM Suhonen, D Chantasart, D Bolikal, and WI Higuchi. Structure-activity relationship for chemical skin permeation enhancers: Probing the chemical microenvironment of the site of action. Journal of Pharmaceutical Sciences 92, 1305-1322 (2003).
[124] GM Golden, JE McKie, and RO Potts. Role of stratum corneum lipid fluidity in transdermal drug flux. Journal of Pharmaceutical Sciences 76, 25-28 (1987).
[125] E Bodner, M Afri, and AA Frimer. Determining radical penetration into membranes using ESR splitting constants. Free Radical Biology and Medicine 49, 427-436 (2010).
[126] AC Benniston and G Copley. Lighting the way ahead with boron dipyrromethene (Bodipy) dyes. Physical Chemistry Chemical Physics 11, 4124-4131 (2009).
[127] DM Bagley, JR Gardner, G Holland, RW Lewis, JF Regnier, DA Stringer, and AP Walker. Skin irritation: Reference chemicals data bank. Toxicology In Vitro 10, 1-6 (1996).
[128] SJ Lord, NR Conley, H-LD Lee, SY Nishimura, AK Pomerantz, KA Willets, Z Lu, H Wang, N Liu, R Samuel, R Weber, A Semyonov, M He, RJ Twieg, and WE Moerner. DCDHF fluorophores for single-molecule imaging in cells. ChemPhysChem 10, 55-65 (2009).
[129] H Wang, Z Lu, SJ Lord, WE Moerner, and RJ Twieg. Modifications of DCDHF single molecule fluorophores to impart water solubility. Tetrahedron Letters 48, 3471-3474 (2007).
[130] N Kanikkannan, RJ Babu, and M Singh. Structure-activity relationship of chemical penetration enhancers. In EW Smith, HI Maibach, editors. Percutaneous Penetration Enhancers. Boca Raton, FL: CRC Press, 17-33 (2006).
[131] N Kanikkannan, K Kandimalla, SS Lamba, and M Singh. Structure-activity relationship of chemical penetration enhancers in transdermal drug delivery. Current Medicinal Chemistry 7, 593-608 (2000).
[132] S Ghosh, S Hornby, G Grove, C Zerwick, Y Appa, and D Blankschtein. Ranking of aqueous surfactant-humectant systems based on an analysis of in vitro and in vivo skin barrier perturbation measurements. Journal of Cosmetic Science 58, 599-620 (2007).
[133] BE Polat, WM Deen, R Langer, and D Blankschtein. A physical mechanism to explain the synergism in transdermal enhancement between low-frequency ultrasound and chemical penetration enhancers. Journal of Controlled Release (2011).

[134] R Alvarez-Roman, A Naik, YN Kalia, H Fessi, and RH Guy. Visualization of skin penetration using confocal laser scanning microscopy. European Journal of Pharmaceutics and Biopharmaceutics 58, 301-316 (2004).
[135] P Karande and S Mitragotri. Transcutaneous immunization: An overview of advantages, disease targets, vaccines, and delivery technologies. Annual Review of Chemical and Biomolecular Engineering 1, 175-201 (2010).
[136] S Paliwal and S Mitragotri. Therapeutic opportunities in biological responses of ultrasound. Ultrasonics 48, 271-278 (2008).
[137] A Yamagishi, T Masui, and F Watanabe. Selective activation of reactant molecules by reversed micelles. Journal of Physical Chemistry 85, 281-285 (1981).
[138] J Kushner, W Deen, D Blankschtein, and R Langer. First-principles, structure-based transdermal transport model to evaluate lipid partition and diffusion coefficients of hydrophobic permeants solely from stratum corneum permeation experiments. Journal of Pharmaceutical Sciences 96, 3236-3251 (2007).
[139] B Yu, KH Kim, PTC So, D Blankschtein, and R Langer. Evaluation of fluorescent probe surface intensities as an indicator of transdermal permeant distributions using wide-area two-photon fluorescence microscopy. Journal of Pharmaceutical Sciences 92, 2354-2365 (2003).
[140] B Yu, KH Kim, PTC So, D Blankschtein, and R Langer. Topographic heterogeneity in transdermal transport revealed by high-speed two-photon microscopy: determination of representative skin sample sizes. Journal of Investigative Dermatology 118, 1085-1088 (2002).
[141] S Uchiyama, T Santa, T Fukushima, H Homma, and K Imai. Effects of the substituent groups at the 4- and 7-positions on the fluorescence characteristics of benzofurazan compounds. Journal of the Chemical Society, Perkin Transactions 2: Physical Organic Chemistry 10, 2165-2173 (1998).
[142] PN Moore, A Shiloach, S Puvvada, and D Blankschtein. Penetration of mixed micelles into the epidermis: effect of mixing sodium dodecyl sulfate with dodecyl hexa(ethylene oxide). Journal of Cosmetic Science 54, 143-159 (2003).
[143] PN Moore, S Puvvada, and D Blankschtein. Challenging the surfactant monomer skin penetration model: penetration of sodium dodecyl sulfate micelles into the epidermis. Journal of Cosmetic Science 54, 29-46 (2003).
[144] ME Johnson, D Blankschtein, and R Langer. Evaluation of solute permeation through the stratum corneum: lateral bilayer diffusion as the primary transport mechanism. Journal of Pharmaceutical Sciences 86, 1162-1172 (1997).
[145] S Mitragotri. In situ determination of partition and diffusion coefficients in the lipid bilayers of stratum corneum. Pharmaceutical Research 17, 1026-1029 (2000).